INVESTIGATION OF THE PLASMA ACCELERATION MECHANISM WITHIN A COAXIAL HALL THRUSTER

BY

William Anthony Hargus, Jr.

March 2001

Report N0. TSD-130

Work Sponsored by
US Air Force Research Laboratory
US Air Force Office of Scientific Research

High Temperature Gasdynamics Laboratory
Thermosciences Division
Stanford University
Stanford California 94305-3032

Abstract

The Hall thruster is an electro-static propulsive device in which electric body forces accelerate ionized xenon propellant to velocities in excess of 18 km/s (>250 eV). These devices are to be used for on-orbit satellite propulsion where their high specific impulse allows for longer lifetimes and/or reduced satellite launch mass due to a reduction of approximately 50% of the propellant that would otherwise be required for conventional chemical thrusters now in use.

This work describes the development and construction of a laboratory Hall thruster as well as the measurement of propellant acceleration within the device. Thrust, electric fields, and propellant velocities in the plume and interior portions of the acceleration channel were characterized. Axial ion and neutral velocity profiles for several discharge voltage conditions were measured as were radial ion velocity profiles in the near field plume. Ion velocity measurements were performed using laser induced fluorescence with nonresonant signal detection of the xenon ion $5d[4]_{7/2} - 6p[3]_{5/2}$ excitation transition while monitoring the signal from the $6s[2]_{3/2} - 6p[3]_{5/2}$ transition. Neutral axial velocity measurements were similarly performed in the interior of the Hall thruster using the $6s[3/2]_2^0 - 6p[3/2]_2$ transition with resonance fluorescence collection. Optical access to the interior of the Hall thruster was provided by a 1 mm wide axial slot in the outer insulator wall. While the majority of the ion velocity measurements used partially saturated fluorescence to improve the signal to noise ratio, a radial trace of the ion transition was taken in the linear fluorescence region and yielded an ion translational temperature between 400 and 800 K at a location 13 mm into the plume. Emissive probe based plasma potential measurements extended from 50 mm outside the thruster exit plane to the near anode region. For each condition, the axial electric field was calculated from the plasma potential, and the local electron temperature was determined from the difference between the floating and plasma potentials. These two sets of complementary measurements delineate the structure of the plasma and indicate that the ionization and acceleration regions are separated to some degree. Also, these measurements indicate a region of low electric field near the thruster exit, especially at the higher discharge voltages. It is believed that this region of near con-

stant potential (low electric field) is a result of oscillations which enhance the local plasma conductivity.

This work is the first effort to non-intrusively investigate the propellant acceleration within a Hall thruster using laser induced fluorescence. Coupled with more conventional probe measurements of the potential and electric fields, the entire propellant acceleration process starting with the propellant ionization and extending into the plume has been characterized. This body of information has increased the understanding of the physics Hall thruster operation. With greater understanding of the mechanisms governing Hall thruster operation, it will be possible to increase the efficiency and lifetime of these devices.

Table of Contents

List of Tables

List of Figures

Variable Dictionary

Roman Characters

A	nuclear magnetic dipole hyperfine spin splitting constant
A	exposed probe area
A	cross-sectional area of acceleration channel
A_{21}	Einstein coefficient for spontaneous emission between levels 2 and 1
A_l	acceleration channel wall area
a	numerical constant dependent on the mean square deviation of the plasma density fluctuation generally taken to have a value of approximately 1/16
$\vec{B}$	vector magnetic field
B	nuclear electric quadrapole moment hyperfine spin splitting constant
B	radial magnetic field strength
B^*	optimal radial magnetic field strength
B_{12}	Einstein coefficient for induced absorption between levels 1 and 2
B_{21}	Einstein coefficient for induced emission between levels 2 and 1
B_{anode}	radial magnetic field strength at anode
B_{max}	maximum radial magnetic field strength in acceleration channel
C	intermediate constant for nuclear spin split hyperfine structure

c	speed of light
$\bar{c}_e$	electron mean thermal speed
$\bar{c}_i$	ion mean thermal speed
D	ionization region depth
D	radial position reference
D	classical cross-field diffusion coefficient
D_B	Bohm diffusion coefficient
D_{probe}	probe diameter
$\vec{E}$	vector electric field
E_I	electron energy at which the secondary electron yield first exceeds unity
E_{II}	electron energy at which the secondary electron yield returns below unity
E_{kin}	average kinetic energy acquired by each fully accelerated propellant ion
E_{max}	electron energy at which secondary electron yield is maximum
E_z	axial electric field strength
e	elementary charge
ΔE_F	combined nuclear spin split energy level shift combining the effect of the nuclear magnetic dipole moment and the electric quadrapole moment
ΔE_M	energy level shift associated with the magnetic dipole of the nucleus

ΔE_Q	energy level shift associated with the electric quadrapole of the nucleus
$\boldsymbol{F}$	total angular momentum
F	restoring force
$\vec{F}$	Lorentz force exerted on a charged particle
f_{12}	transition oscillator strength between levels 1 and 2
g	relative speed of colliders
g	Earth's gravitational constant
$g_c(\nu)$	purely collisionally broadened transition line shape function
$g_d(\nu)$	purely Doppler broadened Gaussian line shape function
g_{ef}	constant associated with thermionic emission from a filament
g_G	mean Gaunt factor
g_i	degeneracy of the i^{th} energy level
$g_v(\nu)$	line shape function for Voigt profile
H	pendulum length
h	Plank's constant
$h\nu_{12}$	energy difference between levels 1 and 2
$\boldsymbol{I}$	nuclear spin
I	probe current
I	discharge current
I_e	electron current
I_ν	incident laser irradiance per unit frequency interval

I_e^*	electron saturation current
I_{ef}	filament emission current
I_{ef}^o	saturated filament emission current
I_{sat}^{ν}	saturation spectral irradiance
I_{sp}	specific impulse
$\boldsymbol{J}$	electron total angular momentum
J	anode current density
J_e	electron current density
J_H	Hall electron current density
I_i^*	ion saturation current
J_z	axial electron current density
$\hat{j}$	applied current density
K	effective spring constant
k	Boltzmann’s constant
L	length of acceleration channel
M	ion mass
m	particle mass
$\dot{m}$	total propellant flow rate
m_e	electron mass
$\dot{m}_i$	ionized propellant flow rate
$\dot{m}_N$	neutral propellant flow rate

m_{Xe}	atomic mass of xenon
mg	gravitational force acting on pendulum mass
N	total population
N_1	population of lower level, level 1
N_2	population of upper level, level 2
N_1^0	unperturbed population of lower level, level 1
N_j	population of the j^{th} level
n_e	electron number density
n_N	neutral number density
n_s	sheath edge plasma density
P	thruster power
$Q_{Ne}(g)$	neutral-electron collisional ionization cross-section for a particular value of g
Q_{21}	quenching rate coefficient between levels 1 and 2
q	particle charge
R_{ion}	neutral-electron collisional ionization rate
r_L	Larmor radius
S	transition strength
$S^{1 \rightarrow 2}$	electron collisional excitation coefficient
S_f	measured fluorescence signal power
T	thrust

T	temperature
T_{Ent}	thrust generated in ground test facilities due to entrainment of background neutrals
T_e	electron temperature
T_f	temperature of thermionically emitted electrons
T_i	ion temperature
T_{kin}	kinetic temperature
t	time
u_B	Bohm drift speed
$\overrightarrow{u_d}$	Hall drift velocity
u_s	ion sheath edge drift speed
V	sample volume
$V(a, x)$	Voigt profile variable
ΔV_{anode}	anode fall
v	absorber velocity component along laser beam propagation vector
$\bar{v}$	mean propellant exit velocity
$\bar{v}_i$	mean ion exit velocity
$\bar{v}_N$	mean neutral exit velocity
W	acceleration channel width
$\vec{w}$	particle velocity
w_x, w_y	components of $\vec{w}$ in the plane normal to $\vec{B}$

$\vec{w}_{\|}$	particle velocity component parallel to magnetic field $\vec{B}$
$\vec{w}$	particle velocity component normal to magnetic field
X	pendulum displacement
Z	axial position reference

Greek Characters

α	ionization fraction
α	phase angle
β	Hall parameter
Γ_e	electron flux
Γ_i	ion flux
γ	loss coefficient due to neutral propellant exiting thruster
δ	secondary electron yield
δ	loss coefficient due to profile losses
δ_{max}	peak secondary electron yield
ε_{12}	energy difference between levels 1 and 2
ε_l	wall energy loss in a collisionless plasma
ς	geometrical scaling factor
η	thrust efficiency
η_d	detection system efficiency
κ	constant associated with transition strength S
λ_D	Debye length

μ_B	Bohm mobility
ν_o	transition center frequency
$\delta\nu_{12}$	Doppler frequency shift
ν_c	collision frequency
$\Delta\nu_c$	full width at half maximum of the purely collisionally broadened line shape
$\Delta\nu_{csat}$	full width at half maximum of a saturated purely collisionally broadened line shape
$\Delta\nu_d$	full width at half maximum of the purely Doppler broadened line shape
ρ_N	neutral propellant density near anode
σ	classical conductivity of a collisionless plasma across a magnetic field
σ_B	conductivity of a collisionless plasma across a magnetic field due to Bohm diffusion
σ_w	effective wall axial conductivity
φ	arbitrary probe potential
φ_A	anode potential
φ_f	final plasma potential of average propellant ion
φ_f	floating potential
φ_i	plasma potential at creation of average propellant ion
φ_{ion}	ionization potential
φ_{loss}	plasma potential loss

φ_p	plasma potential
Ω	solid angle subtended by the collection optics
ω	Larmour frequency, or cyclotron frequency

Chapter 1. Introduction

1.1 Motivation and Objectives

The objective of this work is to measure plasma properties of a Hall thruster discharge to better understand the physics intrinsic to Hall thruster operation and validate Hall thruster models. Due to the limited nature of current modeling efforts, the understanding of the physical processes governing the operation of these plasma devices relies heavily on experimental diagnostics. Present Hall thruster technology has demonstrated good performance characteristics; however, further understanding of the plasma discharge physics is required before improvements in Hall thruster technology can advance. Once comprehensive measurements and validated numerical models are available, further refinement in the efficiency of Hall thrusters will be possible.

In order to provide better understanding of Hall thruster physics, measurements of three plasma parameters are performed. Velocity is the most important plasma parameter in an electric thruster. The thrust produced is directly proportional to the exhaust velocity. As such, knowledge of the propellant velocity is crucial to validate any attempt to numerically simulate a Hall thruster discharge. If the velocity field can be measured with high spatial resolution, important parameters such as the profile velocity spread and the relative energy imparted to the propellant provide important clues to losses inherent to the acceleration process. Since Hall thrusters are electro-static plasma accelerators, the velocity and acceleration of the ionized propellant depend on the electric fields produced by the device. In order to fully understand the plasma acceleration within a Hall thruster, these plasma parameters must also be measured. Relative plasma potential data may be extracted from velocity data as can the effective electric field profile. These data may be compared to direct measurements of the absolute plasma potential which will yield the electric field. The final critical parameter essential for understanding Hall thruster physics is electron temperature. Electron temperature data provide information on the ionization rate of the propellant. In addition, electron temperature data provide an indication of the electron mobility within the magnetic field which retards electron flow to the anode in a Hall thruster. These three parameters are vital for Hall thruster characterization. By understanding the plasma processes occurring

within a Hall thruster, valuable resources for validation of numerical simulations are created.

1.2 Organization

First, the physics within a Hall thruster will be discussed. The discussion will begin with a description of the interaction of charged particles with electric and magnetic fields. The various processes, including ionization, acceleration, and neutralization, will be discussed as they pertain to Hall thruster operation. The scaling relations required for Hall thruster design will then be explained accounting for the relevant physical mechanisms. Next, the diagnostic techniques used to probe the Hall thruster plasma will be presented as will the theory behind each. The diagnostics discussed will include: thrust measurements, laser velocimetry using the relatively complex spectrum of xenon, and the use of emissive plasma potential probes. The experimental apparatus will then be discussed. This will be followed with a discussion of the Hall thruster design. The behavior and characteristics of the prototype device will be outlined including the lessons that led to the construction of a second device on which most of the measurements in this work were performed. The vacuum and support facilities will also be presented as will the apparatus used to perform the diagnostics. These experimental facilities include: the thrust stand used to measure thrust generated by the Hall thruster, the lasers and optics used to measure the propellant velocity, and the emissive plasma potential probes used to measure the plasma potential field. The results of the diagnostic measurements will then be presented and discussed. These results will first show that the thruster constructed for this work resembles devices being studied by other researchers. The location of the ionization and acceleration zones as well as the magnitude of the peak electron temperature will be identified. Finally, the conclusions of this work will be presented. These will include a number of suggestions for future work on Hall thruster development and related projects.

1.3 Background

1.3.1 Electric Propulsion Fundamentals

The essential principles of electric propulsion have been recognized since the inception of modern rocketry (Goddard). Yet only now, 40 years after the first orbital flights of Sputnik and Explorer, is electric propulsion a viable alternative to chemical spacecraft propulsion. The first low power hydrazine arcjets have been launched aboard commercial communication satellites, a high power ammonia arcjet has recently undergone space flight tests (Salasovich et al.), and an ion engine has powered a NASA deep space flight mission to a rendezvous with an asteroid (Brophy). Other electric propulsion devices are also being readied for flight, including magnetoplasmadynamic thrusters, pulsed plasma thrusters, and an array of electric thrusters from around the world (Toki and Saasoh, Spanjers et al., Spores et al. 1997).

Electric propulsion in its most general sense can be defined as; “The acceleration of gases for propulsion by electrical heating and/or by electric and magnetic body forces.” (Jahn). While this definition appears relatively straight forward, the are many methods by which electricity and propellants may be combined to create propulsive devices. As illustrated in Figure 1.1, there are three main categories of electric propulsion; electrothermal, electrostatic, and electromagnetic. In electrothermal devices, the propellant gases are electrically heated and then expanded to produce thrust. A common example of this classification is the arcjet in which the propellant is heated by an arc between two electrodes and subsequently expanded through a nozzle. In electrostatic devices, the propellant is first ionized and the resulting ions are then accelerated by direct application of electric body forces. The classic example of an electrostatic thruster is the ion, or Kaufman, engine. Here a number of positive ions are created within the thruster. The ions are then accelerated by an electric field supported by a series of grids and neutralized by an external electron source. In electromagnetic devices, ions are accelerated by the combination of electric and magnetic fields producing Lorentz forces which exert an electromagnetic force on the propellant. An example of an electromagnetic thruster is a magneto-hydro-dynamic channel in which an applied cur-

rent $\vec{j}$ and an orthogonal magnetic field $\vec{B}$ produce a $\vec{j} \times \vec{B}$ propellant accelerating force (Jahn).

The principle advantage of electric propulsion over traditional chemical propulsion is that electric propulsion is not limited in its propellant energy release. Chemical systems rely on the energy released from chemical bonds to produce thermal energy that is then converted into propulsive thrust by expansion through a nozzle. It can be shown that the energy available to chemical reactions in a conventional rocket is on the order of 70 MJ/kg (Hill and Peterson). This energy is an intrinsic property of the propellants. Electric thrusters have no limitation on the amount of energy that may conceivably be deposited into the propellant. Since electric thrusters require electrical energy, the engineering trade off is that thrust levels are limited by the availability of electrical power. Table 1.1 shows the specific impulse ranges for the several general types of chemical and electric thrusters (Jahn).

Electric thrusters produce specific impulses between 1.5 to 25 times that of chemical thrusters. By virtue of their much higher specific impulses, electric thrusters are capable of using significantly less propellant mass to produce the same impulse as chemical thrusters, thereby enhancing spacecraft capabilities and reducing life cycle costs. The high specific impulse of electric propulsion is not without penalties. Since the available power from the spacecraft is fixed and the specific impulse of the thruster is high, electric propulsion is generally limited to a low thrust level. The inherent power limitations of spacecraft relegate electric propulsion to the low thrust niche of space propulsion. Low thrust, high specific impulse applications include satellite station-keeping, repositioning, and attitude control. These include missions such as orbit raising, plane changes, and orbital repositioning which require large changes in orbital velocity and are very propellant intensive. With the high specific impulse of electric propulsion, these missions become possible.

Table 1.1: Specific Impulse Ranges of Various Thrusters

Thruster Type	Specific Impulse, I_{sp} (s)
Liquid Monopropellants	170 - 290
Solid Propellants	210 - 320
Liquid Bipropellants	290 - 450

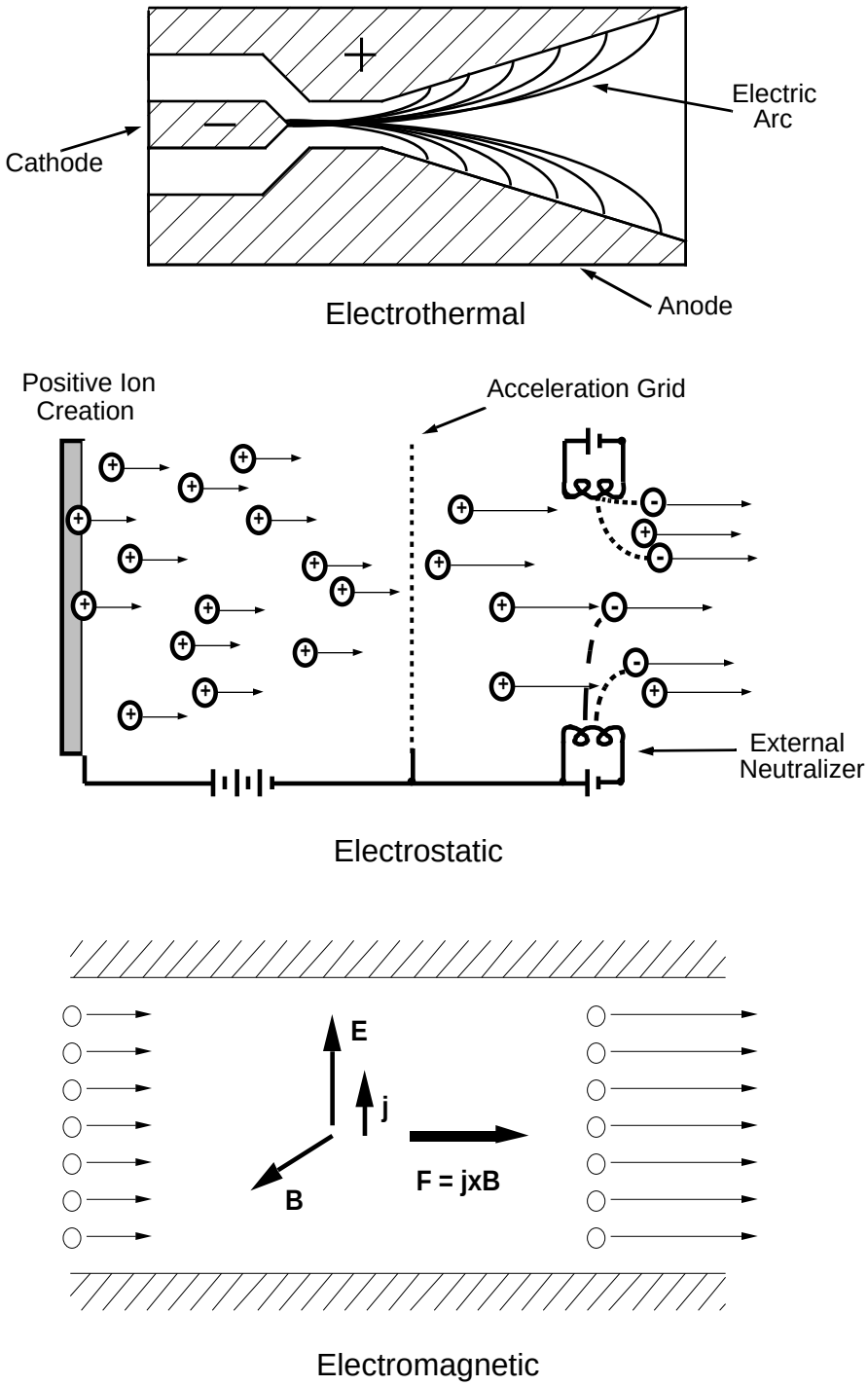

Figure 1.1. Basic operation of electrothermal (arcjet), electrostatic (ion engine), and electromagnetic (MHD channel) thruster concepts.

Table 1.1: Specific Impulse Ranges of Various Thrusters

Thruster Type	Specific Impulse, I_{sp} (s)
Exotic Bipropellants and Tripropellants	400 - 600
Arcjets	500 - 1000
Hall Thrusters	1000 - 1800
Ion Thrusters	1200 - 5000

For some on-orbit propulsion missions, low thrust levels are an advantage. Low thrust levels may be used to provide more precise positioning and attitude control than higher thrust chemical devices (Janson). For some orbit repositioning missions, constant low thrusting allows for more fuel economy and faster repositioning (Spores et al. 1995). Other missions for electric propulsion include reusable electric orbit transfer vehicles and planetary missions (Brophy), as well as novel high maintenance orbits such as low altitude, high drag orbits and formation flying (Janson).

1.3.2 Hall Thruster Orbital Missions

Table 1.2 shows the launch costs and payload capability of available launch vehicles (Larson and Wertz). With launch costs averaging $10,000/lb to geosynchronous orbit, reduced launch mass directly translates into lower cost or increased capability. Hall thrusters are now being considered for use on commercial, research, and military spacecraft. This technology provides economic advantages that can be translated into lower launch mass, longer lifetimes, or larger useful payloads. Hall thrusters are a nearly mature technology for satellite propulsion. Thrusters, such as the Russian built SPT-100, deliver thrusts of approximately 100 mN at a specific impulse approaching 1800 s with an efficiency above 50%.

Hall thrusters are ideal for a variety of missions. Orbital repositioning and orbit raising both benefit from high efficiencies that maximize the thrust produced relative to electrical energy consumed. This minimizes the mass associated with solar panels, or other power sources. High specific impulse also minimizes the propellant mass required so that satellites can either carry less propellant mass, trading it for more payload, or retain the propellant mass and increase the useful lifetime of the system. Additionally, the relatively high

thrust levels, for an electric thruster, allow Hall thrusters to complete their missions in reasonable times.

Table 1.2: Launch costs associated with U.S. launch vehicles

Vehicle	Weight (kg)	Payload (kg)	Cost ($x10^6)	Specific Cost ($/kg)
Pegasus	25,000	460	12	26,100
Delta II	230,000	5,100	50	9,800
Atlas II	240,000	8,600	100	11,600
Titan IV	860,000	21,600	200	9,300
Shuttle	2,040,000	24,400	250	10,200

Hall thrusters are not always the best electric propulsion option. For example, arcjets with their high thrust levels are much better suited for missions where the Van Allen belts must be traversed quickly. The trip time through the radiation belts must be minimized to preserve the solar panels which are susceptible to damage in the radiation belts. Another mission regime where Hall thrusters are supplanted is interplanetary missions. In these, the goal is to reach extraterrestrial objects that would otherwise be too expensive to reach without high specific impulse propulsion. For these missions, the specific impulse must be maximized and the best thruster choice is the ion engine. In this case, the propellant mass is the primary cost driver of the mission.

This argument can be visualized more clearly by examining the equation which defines the efficiency η of a Hall thruster such that the relationship between thrust and specific impulse is apparent.

$$T = \frac{P\eta}{2gI_{sp}} \tag{1.1}$$

Where T is thrust, P is the power provided to the electric thruster, and g is the gravitational constant of Earth. Equation 1.1 shows that thrust is proportional to power and efficiency. So for a fixed I_{sp}, increasing power and/or efficiency will provide more thrust. With increased

thrust, it is likely that the spacecraft will have a shorter trip time to its objective. However for a fixed power spacecraft, increasing the specific impulse of the thruster will decrease the thrust produced and most likely produce a longer trip time. However, the spacecraft with the higher specific impulse thruster will need to carry less propellant mass to produce the same impulse. It is this series of engineering trade offs that make tailoring electric thrusters for various missions nonintuitive.

Chapter 2. Hall Thruster Theory of Operation

2.1 Charged Particle Dynamics in Electric and Magnetic Fields

In order to understand the behavior of the plasma within a Hall thruster, it is first necessary to understand the behavior of individual charged particles under the influence of electric and magnetic fields. This discussion will be based on the Lorentz equation.

$$\vec{F} = q[\vec{E} + \vec{w} \times \vec{B}] \tag{2.1}$$

Where $\vec{F}$ is the force exerted on the particle of charge q and velocity $\vec{w}$ by the electric field $\vec{E}$ and a magnetic field $\vec{B}$. Ignoring relativistic effects, this equation describes an isolated charged particle acted on by electric and magnetic fields in an inertial frame (Mitchner and Kruger). This discussion will now continue with an examination of a charged particle in uniform fields.

2.1.1. Particle Motion in Uniform Fields: B = 0

The simplest case to consider is the case of a particle of mass m in a uniform and constant electric field. In this case, the equation of motion is given by the following.

$$m\frac{d}{dt}\vec{w} = q\vec{E} \tag{2.2}$$

If the particle does not experience any collisions, it will accelerate indefinitely along the electric field lines with the direction dependent on the polarity of the charge q.

2.1.2 Particle Motion in Uniform Fields: E = 0

In the case of a constant magnetic field and no electric field, the equation of motion of a charged particle can also be derived from Equation 2.1.

$$m\frac{d}{dt}\vec{w} = q\vec{w} \times \vec{B} \tag{2.3}$$

The magnetic field does no work on the particle and the particle's kinetic energy is constant since the right hand side of Equation 2.3 is orthogonal to the magnetic field $\vec{B}$. This can also be illustrated by separating Equation 2.3 into two vector components for convenience.

$$\frac{d\vec{w}_{\parallel}}{dt} = 0 \tag{2.4}$$

$$\frac{d\vec{w}}{dt} = \frac{q}{m}(\vec{w} \times \vec{B}) \tag{2.5}$$

The first component represents the motion parallel to the magnetic field vector and the second component that normal to the magnetic field. Since the kinetic energy is a constant, the magnitude of $\vec{w}$ is also a constant.

If a Cartesian coordinate system is introduced where the magnetic field is positioned along the Z axis, the components of Equation 2.5 are constrained to the X-Y plane. After carrying out the cross product, the components w_x and w_y are shown below.

$$\frac{dw_x}{dt} = \frac{qB}{m} w_y \tag{2.6}$$

$$\frac{dw_y}{dt} = \frac{-qB}{m} w_x \tag{2.7}$$

The solutions to this set of linear ordinary differential equations defines a circular motion.

$$w_x = w \cos(\omega t + \alpha) \tag{2.8}$$

$$w_y = \mp w \sin(\omega t + \alpha) \tag{2.9}$$

Where α is a phase angle dependent on initial conditions. The upper sign in Equation 2.9 corresponds to the case when the particle's charge is positive ($q > 0$) and the lower sign corresponds to the case when the particle's charge is negative ($q < 0$). The frequency of motion ω also known as the Larmor, or cyclotron, frequency is defined by Equation 2.10.

$$\omega = \frac{|q|B}{m} \tag{2.10}$$

The radius of the oscillatory motion r_L, also known as the Larmor radius, is determined by the ratio of the oscillation speed w and the frequency of oscillation ω.

$$r_L = \frac{w}{\omega} = \frac{mw}{|q|B} \tag{2.11}$$

The sense of rotation is clockwise about the magnetic field lines for a positively charged particle and counterclockwise for a negatively charged particle. It must also be remembered that all the calculations until now have neglected the velocity in the Z direction, $w_z = w_{||}$. The actual motion of the charged particle is a helix axially traveling at $w_{||}$ with the rotation dependent on the charge of the particle as previously explained.

In real plasmas where collisions occur, a measure of the true particle motion known as the Hall parameter is important. Collisions disturb the helical motion described above. The Hall parameter β is the ratio of the Larmor frequency ω to the collision frequency ν_c.

$$\beta = \frac{\omega}{\nu_c} \tag{2.12}$$

The Hall parameter is a measure of how many oscillations around the magnetic field lines occur during the characteristic time for collisions. The Hall parameter, just like the Larmour frequency and radius, varies between particles due to mass, charge, and temperature.

2.1.3 Particle Motion in Uniform Fields: E ≠ 0, B ≠ 0

Now that the two limiting cases have been discussed, the general case of a single charged particle subject to both electric and magnetic fields will be examined. The equations of motion can be reduced from the general case of Equation 2.1 into a form resembling Equations 2.4 and 2.5.

$$\frac{d\vec{w}_{\parallel}}{dt} = \frac{q}{m}\vec{E}_{\parallel} \tag{2.13}$$

$$\frac{d\vec{w}}{dt} = \frac{q}{m}(\vec{E} + \vec{w} \times \vec{B}) \tag{2.14}$$

Where the acceleration experienced by the particle is again separated into the vector components normal and parallel to the magnetic field $\vec{B}$. As before, a Cartesian coordinate system is fixed such that $\vec{B}$ is aligned with the Z axes constraining the motion described by Equation 2.14 to the X-Y plane. Equation 2.14 may be reduced to the component equations of motion for the X and Y axes.

$$\frac{dw_x}{dt} = \frac{q}{m}(E_x + w_y B) \tag{2.15}$$

$$\frac{dw_y}{dt} = \frac{q}{m}(E_y - w_x B) \tag{2.16}$$

The system of inhomogeneous linear ordinary differential equations in Equations 2.15 and 2.16 may then be solved for the velocity components along the X and Y axes.

$$w_x = w \cos(\omega t + \alpha) + \frac{E_y}{B} \tag{2.17}$$

$$w_y = \mp w \sin(\omega t + \alpha) - \frac{E_x}{B} \tag{2.18}$$

Where the negative sign in Equation 2.18 designates negatively charged particles and the positive sign holds for positively charged particles.

These equations of motion are similar to those in Equations 2.8 and 2.9 with the exception of the final term on the right hand side of each. This term corresponds to the drift associated with the motion of a charged particle in a region of space containing crossed electric and magnetic fields. A vector relation for this drift can be extracted from Equation 2.1.

$$[\vec{E} + \vec{w} \times \vec{B}] = 0 \tag{2.19}$$

This relation holds since energy in the X-Y plane is conserved. If the cross product of the above relation is taken with respect to the magnetic field, it is possible to determine the electric field drift of the center of rotation.

$$[\vec{E} + \vec{w} \times \vec{B}] \times \vec{B} = \vec{E} \times \vec{B} - B^2 \vec{w} + (\vec{w} \cdot \vec{B})\vec{B} = 0 \tag{2.20}$$

Where the designation for the transverse component has been removed to relieve the notation. Now, the transverse portion of the above equation provides an expression for the drift velocity $\vec{u_d}$.

$$\vec{u_d} = \frac{\vec{E} \times \vec{B}}{B^2} = \vec{w}_{\|} \tag{2.21}$$

A special case where the electric and magnetic fields are orthogonal is shown in Figure 2.1. It shows the general behavior of positive and negatively charged particles. It is important to note that $\vec{u_d}$ is independent of q, m, and $\vec{w}$. In the first half cycle of a positively charged particle's orbit, the particle gains energy from the electric field and increases

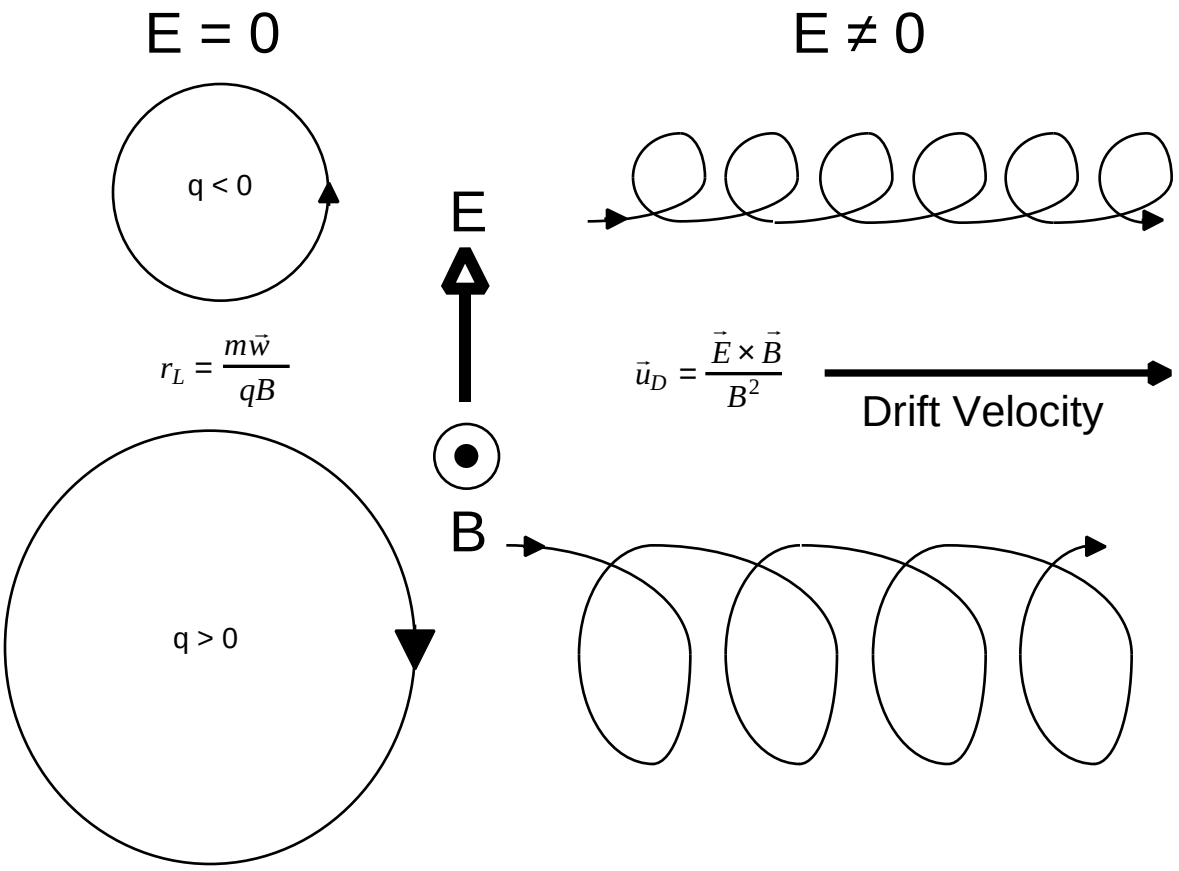

Figure 2.1. The Larmor radius and drift velocity defined for particles of negative and positive charge. The smaller Larmor radius assumes smaller mass, or lower energy.

in $\vec{w}$ and therefore in r_L. In the second half cycle, the positive ion loses energy to the electric field so $\vec{w}$ and r_L decrease. The difference in r_L on the top and bottom sides of the orbit causes the drift $\overrightarrow{u_d}$. A negatively charged particle orbits in the opposite direction, but also gains energy in this direction. The result is that charged particles drift in the same direction regardless of polarity. For particles of equal charge, the lighter one will have a smaller r_L and therefore drift less per cycle. However, the Larmor frequency ω will be higher and two effects will exactly cancel (Chen).

2.2 Hall Thruster Physics

2.2.1 General Operating Features

Figure 2.2 shows a schematic of a typical Hall type thruster. Hall thrusters function by use of perpendicular electric and magnetic fields. The radial magnetic field acts to impede the flow of electrons from cathode to anode. The electrons are trapped near the exit of a coaxial acceleration channel. The crossed fields produce a net Hall electron current in the $\vec{B} \times \vec{E}$ direction. The trapped electrons act as a volumetric zone of ionization for neutral propellant atoms. Electrons collide with the slow moving neutrals producing ions and more electrons to both support the discharge and ionize additional neutrals. The positive ions are not significantly affected by the magnetic field due to their larger Larmor radii, which are on the order of meters. The ions are accelerated through the electric field produced by the impedance of the magnetic field on the plasma. The resulting high speed ion beam is subsequently neutralized with an external electron source.

The Hall thruster is an electrostatic accelerator where thrust is produced by momentum imparted to the positive ions by electric body forces. The thruster is relieved of space charge limitations by the neutralizing effect of the trapped electrons, and Hall type thrusters are therefore capable of providing higher thrust densities than grided ion engines. Due to the crossed electric and magnetic fields within a Hall thruster, a sizable azimuthal Hall current is produced. To avoid the use additional electrodes, a coaxial geometry is used to short the Hall current, and the electrons are confined in an endless azimuthal drift (Jahn). The typical geometry and sizing of Hall thrusters have not changed significantly since the earliest work reported on Hall type plasma accelerators (Lary et al., Seikel et al., Brown and

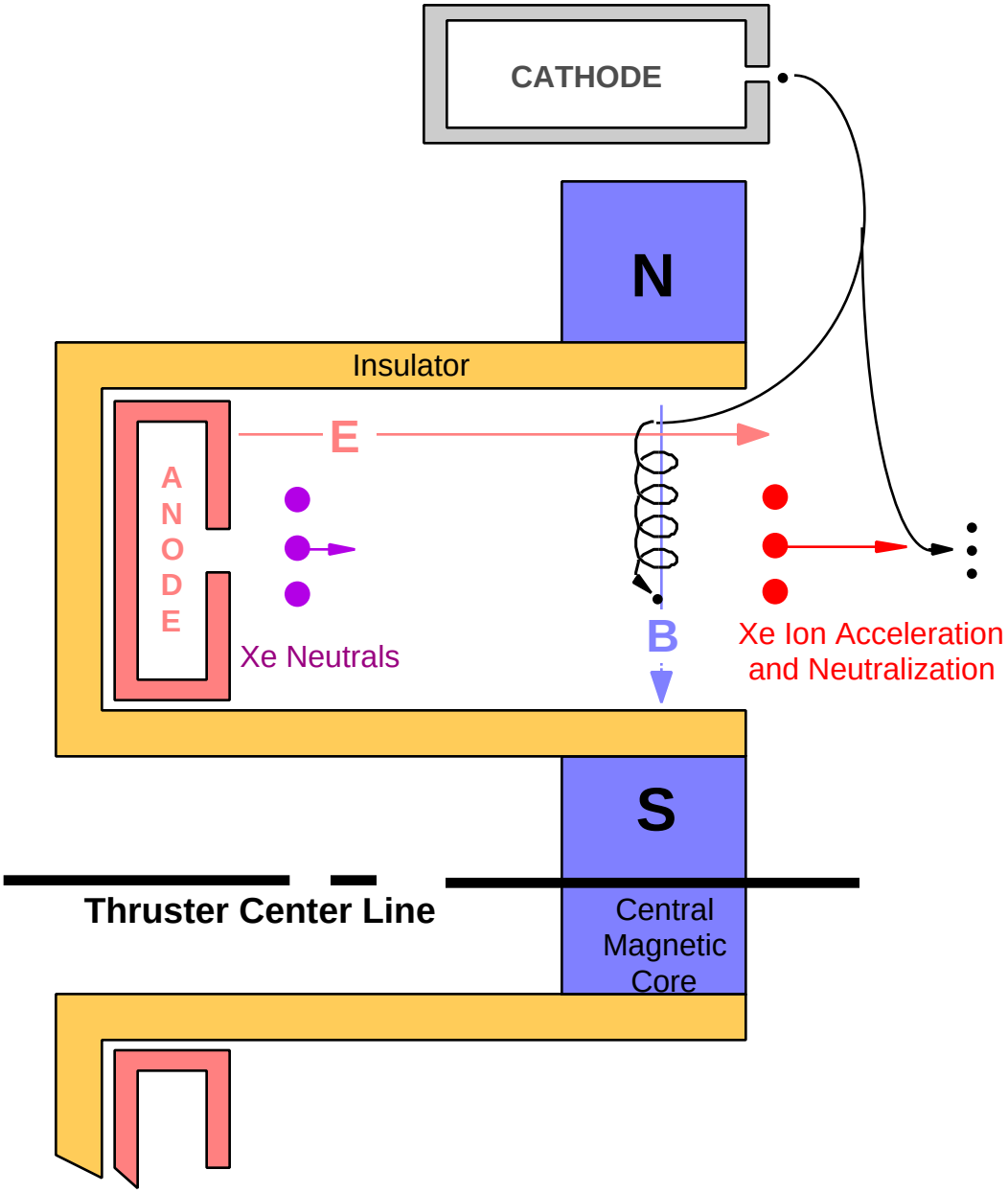

Figure 2.2. Cutaway schematic of a model Hall thruster. Typical magnetic and electric field lines as well as particle trajectories are shown.

Pinsly). More recent thruster designs utilize a coaxial geometry with acceleration channel outer diameters varying from 50 to 280 mm. Channel widths are typically 10-15% of the outer diameter (Bober et al.).

The material used for the magnetic circuit is a ferromagnetic material with a sufficiently high permeability to produce a strong radial field across the exit of the coaxial acceleration channel. A further requirement is that this material have a high saturation flux density. Typically, pure iron, or alloys of iron, provide a good mix of these properties (Lidde). Electrical windings produce the required magnetic field. One large inner coil and several outer coils are generally used. The magnetic circuit subsequently directs the magnetic field lines to produce the requisite field profile.

The plasma discharge within a Hall thruster requires an anode and a cathode. The anode serves two purposes. First, it is the positive electrode supporting the plasma discharge. Second, it distributes the propellant gas through the coaxial acceleration channel. The cathode provides an electron source to both support the electric discharge and neutralize the ion beam. Although this function can be provided by several different devices, hollow cathodes are commonly used. They are used due to their long lifetimes and reliability despite requiring propellant, typically 10-15% of the total propellant flow. Thermionic emission of electrons from a hot filament, although simpler to implement, is generally considered less efficient and more prone to failure.

In the Hall thruster class commonly referred to as *stationary plasma thrusters* (SPT), an electrical insulator isolates the anode from the magnetic circuit. It also directs the propellant into the volume where the neutral propellant is ionized, accelerated, and expelled from the thruster. Insulators are typically manufactured from dielectric materials such as boron nitride, borosil, or alumina. Another class of Hall thrusters known as *anode layer thrusters* (ALT) do not have dielectric insulators. These thrusters have the magnetic circuit in direct contact with the plasma. Electron conduction is minimized by placing the magnetic circuit at negative potential to repel the electrons in the ionization region from the channel walls (King).

2.2.2 Impact of the Magnetic Field

The magnetic field is the single most important parameter in the design of a Hall thruster. The electric field which accelerates the ionized propellant is created by the impedance of the magnetic field to axial electron conduction. The containment of electrons in a Hall thruster depends on the Larmor radius defined in Equation 2.11. For electrons with little, or no, directed velocity, a value for w can be approximated from the electron mean thermal speed $\bar{c}_e$ (Vincenti and Kruger).

$$w \approx \sqrt{\frac{8kT_e}{\pi m_e}} = \bar{c}_e \tag{2.22}$$

Where k is Boltzmann's constant, T_e is the electron temperature, and m_e is the electron mass. In order to constrain the electrons and allow the ions to be accelerated by the electric field within a Hall thruster, the requirements on the thruster radial magnetic field are that the electron Larmor radius be smaller than the width of the acceleration channel. Conversely, the ion Larmor radius must be significantly larger, such that the magnetic field does not affect the trajectory of the ions as they accelerate through the axial potential fall.

$$(r_L)_{ion} \gg W \tag{2.23}$$

$$(r_L)_{electron} \ll W \tag{2.24}$$

Where W is the width of the acceleration channel.

The relationship between the parameters that determine the electron Larmor radius reduces to a function of electron temperature T_e and radial magnetic field strength B.

$$(r_L)_{electron} \propto \frac{\sqrt{T_e}}{B} \tag{2.25}$$

The electron Larmor radius depends only on the magnetic field strength and the electron temperature indicating that the requirement in Equation 2.23 may be achieved comfortably over a wide range of electron temperatures with little magnetic field variation.

With the exception of electron impact ionization of neutrals, the flow within the acceleration channel is essentially collisionless. Electron-neutral collisional ionization places a lower bound on the required electron temperature, approximately equivalent to the ionization potential of the propellant. Typically, the ions have a temperature near 1 eV, and the magnetic field is on the order of 150 G, and the Larmour radii are approximately 50 cm and 1 mm for the ions and electrons, respectively (Cedolin, Sankovic et al. 1993). In regard to the ion Larmour radius, the large mass of xenon (131 amu) compared to other inert propellant gases such as argon (40 amu) and krypton (84 amu) is important in ensuring that the inequality in Equation 2.23 is satisfied (Brown and Pinsly, Lidde).

Equations 2.23 and 2.24 also determine the radial magnetic field profile. The depth of the ionization region D must satisfy these inequalities to ensure electrons are contained in the ionization region, and the following must hold.

$$D \quad W \tag{2.26}$$

Any propellant which is not ionized does not significantly contribute to thrust production. Therefore, care must taken to ensure that most neutrals are ionized. The neutrals can be assumed to reach the ionization region with a velocity v_N. The constraint is that the neutral-electron collisional ionization rate R_{ion} must be sufficiently high so that the majority of the neutrals are ionized in the ionization zone characteristic depth.

$$D » \frac{v_n}{R_{ion}} \tag{2.27}$$

An important limitation of Hall thruster efficiency is the magnitude of the axial electron current. To limit this loss mechanism, the anode is placed far from locations of high electron density where the magnetic field has confined electrons. Typical magnetic circuits produce radial magnetic field profiles resembling Gaussian functions (Morozov et al.). If the

region where Equations 2.23 and 2.24 hold extends over the characteristic width D of this field profile, the total length of the acceleration channel L must be larger than D. Therefore, the following conditions for the magnetic field profile and length of the acceleration channel hold.

$$B_{anode} \ll B_{max} \tag{2.28}$$

$$L > D \tag{2.29}$$

The effects of magnetic field shape has been explored experimentally by Morozov et al. who showed that the profile of the radial magnetic field has a strong effect on the performance of a Hall thruster. At a constant discharge voltage, an ion to electron current ratio of approximately 90% was measured when the magnetic field had a positive gradient through the acceleration channel. Relatively constant, or zero gradient, radial magnetic fields had ion to current ratios near 60% where negative gradient magnetic fields were found to have ion to discharge current ratios less than 50%. For these reasons, it is important that the magnetic field gradient be positive throughout the acceleration channel to maximize thruster performance. In order for this be accomplished, the maximum magnetic field strength B_{max} must be close to the exit plane of the thruster.

2.2.3 Ionization Processes

The Hall thruster is an electrostatic accelerator, and for the propellant to be accelerated, it must first be ionized. The neutral-electron collisional ionization rate R_{ion} is given by the following.

$$R_{ion}(g) = n_N n_e g Q_{Ne}(g) dg \tag{2.30}$$

Where g is the relative speed of collision, n_N is the neutral number density, n_e is the electron number density, and $Q_{Ne}(g)$ is the neutral-electron collisional ionization cross-section for a particular value of g. The complete ionization rate is an integration over all possible

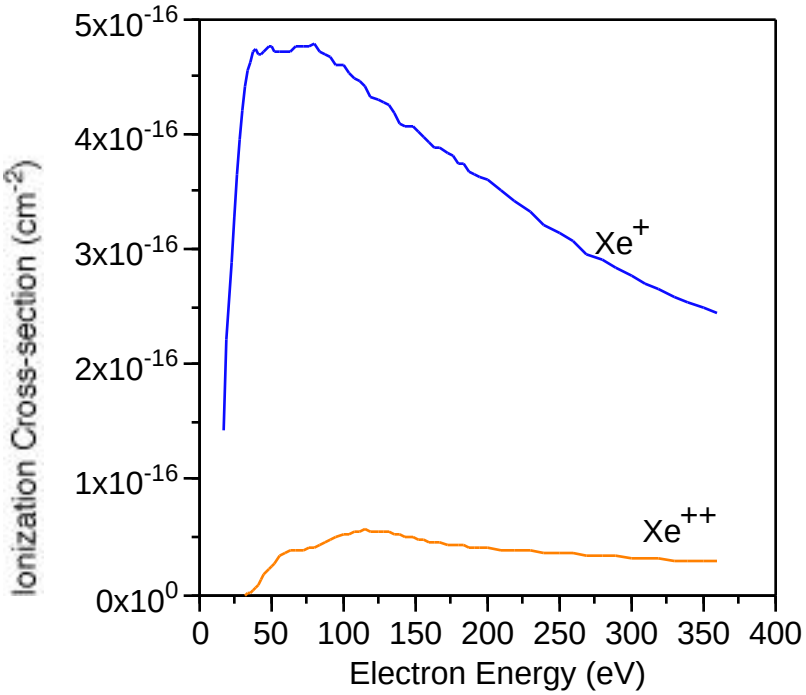

Figure 2.3. Ionization cross-section of Xe to Xe^{+} and Xe^{++} by electron impact (Syage).

relative speeds of collision g (Mitchner and Kruger). The neutral-electron collisional ionization cross-section measured by Syage is presented in Figure 2.3. The ionization cross-section for singly ionized xenon rises from near zero at the ionization potential φ_{ion} at 12.127 eV and peaks at approximately 50 eV with a value of 4.75×10^{-16} cm^{-2}. To find the ionization rate functional dependence on the electron temperature, the neutrals are approximated to be stationary relative to the fast moving electrons. The relative collider speed g in Equation 2.30 is then approximated by the mean electron thermal speed given in Equation 2.22. The functional dependence of the ionization rate relative to electron temperature T_e is shown in Equation 2.31.

$$R_{ion} \quad n_N n_e T_e^{1.5} \tag{2.31}$$

This relation uses a linear approximation of experimental electron impact ionization cross-section. It is only valid for xenon above the ionization potential to the peak of the ionization

cross-section which occurs at an electron energy of approximately 50 eV. Equation 2.31 shows that as the neutral number density is lowered, increases in the electron temperature can compensate, or increase, the ionization rates within a Hall thruster.

The thruster will not operate efficiently if a sizable fraction of the propellant is not ionized. Any propellant not ionized, will not contribute to thrust production. This is best illustrated by examining the conservation of mass and momentum within a Hall thruster. The thrust produced by the propellant is given by the exiting momentum which can be divided into the fractions produced by the ions and neutrals.

$$T = \dot{m}\bar{v} = \dot{m}_i\bar{v}_i + \dot{m}_N\bar{v}_N \tag{2.32}$$

Where T is the total thrust, $\dot{m}$ is the total mass flow rate, $\dot{m}_i$ is the ionized mass flow rate, $\dot{m}_N$ is the neutral mass flow rate, $\bar{v}$ is the mean propellant exit velocity, $\bar{v}_i$ is the mean ion exit velocity, and $\bar{v}_N$ is the mean neutral exit velocity. From conservation of mass, mass flow into and out of the thruster is conserved.

$$\dot{m} = \dot{m}_i + \dot{m}_N \tag{2.33}$$

The ionization fraction α is defined as the ratio of ionized to total densities, or equivalently the ratio of ionized to total flow rates.

$$\alpha = \frac{\dot{m}_i}{\dot{m}} = 1 - \frac{\dot{m}_N}{\dot{m}} \tag{2.34}$$

Now by combining Equations 2.32, 2.33, and 2.34, a relation for the thruster average ionization fraction is extracted.

$$\alpha = \frac{\bar{v} - \bar{v}_N}{\bar{v}_i - \bar{v}_N} \tag{2.35}$$

Equation 2.35 calculates of the ionization fraction from thrust and velocity measurements. These quantities are much easier to measure than directly determining ion and neutral number densities. For example, the thrust of an SPT-100 running at 300V and 5 mg/s of xenon is approximately 75 mN (Sankovic et al.). The ion velocities of this thruster have been measured to be approximately 15.6 km/s (Manzella 1994). Other measurements have shown that the neutral velocities are decoupled from the ion velocities and are on the order of 500 m/s (Cedolin). For this case, it is calculated that over 95% of the propellant has been ionized in the propellant acceleration process. This ionization fraction is supported by emission measurements which confirm the plasma is over 95% ionized in the plume of a Russian SPT-100 Hall thruster (Manzella 1993).

2.2.4 Electric Field

Early Hall thruster studies established that the electron current across the radial magnetic field of a Hall thruster is significantly higher than predicted by classical electrodynamic theory (Lary et al., Seikel et al.). This greater than predicted electron diffusion across magnetic field lines was originally labeled *anomalous diffusion,* although it now often referred to as *Bohm diffusion.* Classical electron diffusion is based on the Boltzmann equation with collision terms providing the transport mechanism across magnetic field lines. The classical conductivity of a plasma across a magnetic field σ is inversely proportional to the square of the magnetic field (Mitchner and Kruger, Lieberman and Lichtenberg).

$$\sigma = \left(\frac{n_e e^2}{kT_e}\right) D = \left(\frac{n_e e^2}{kT_e}\right)\left(\frac{1}{3\nu_c r_L^{\,2}}\right)\frac{n_e}{T_e B^2} \tag{2.36}$$

Where D is the classical cross-field diffusion coefficient related to the conductivity via the Einstein relation, e is the elementary charge, and n_e is the electron number density.

If plasma turbulence is present, plasma conductivity will be enhanced by plasma density fluctuations with simultaneous electric field fluctuations. The resulting skewed $\vec{E} \times \vec{B}$ drift enhances electron diffusion across the magnetic field lines. The axial plasma

conductivity due to Bohm diffusion σ_B is therefore inversely proportional to the radial magnetic field (Yoshikawa and Rose).

$$\sigma_B = \left(\frac{n_e e^2}{kT_e}\right) D_B = \left(\frac{n_e e^2}{kT_e}\right)\left(\frac{1}{3}\right) a c r_L \frac{n_e}{T_e^{0.5} B} \tag{2.37}$$

Where D_B is the Bohm diffusion coefficient, and a is a numerical constant dependent on the mean square deviation of the plasma density fluctuation generally taken to have a maximum value of approximately 1/16.

When the turbulence enhanced plasma conductivity of Equation 2.37 is combined with Ohm's law, Equation 2.38, the dependence of the axial electric field E_z is shown to be proportional to the radial magnetic field B and square root of the electron temperature as well as inversely proportional to the plasma density (Mitchner and Kruger).

$$\vec{J} = \sigma \vec{E} \tag{2.38}$$

$$E_z \quad \frac{J_z B T_e^{0.5}}{n_e} \tag{2.39}$$

Where J_z is the axial electron current density. Equation 2.39 illustrates the importance of the radial magnetic field in the evolution of the axial electric field within a Hall thruster. The electric field is directly proportional to the strength of the radial magnetic field. Supporting experimental evidence exists in the literature (Morozov et al. 1972). However, it must be noted that the electric field is also a function of the electron density and the electron temperature. These properties in turn are also complex functions of the radial magnetic field.

With orthogonal magnetic and electric fields, the electrons in the ionization region move in the $\vec{E} \times \vec{B}$ direction with a drift speed u_d given by Equation 2.21.

$$u_d = \frac{E_z}{B} \quad \frac{J_z T_e^{0.5}}{n_e} \tag{2.40}$$

Where the cross product has been simplified by the orthogonal geometry of a Hall thruster assuming purely radial magnetic and axial electric fields. Recognizing that the electric and magnetic fields are orthogonal, the drift velocity can be used to determine the Hall electron current density J_H.

$$J_H = -en_e \frac{E_z}{B} \quad -eJ_z T_e^{0.5} \tag{2.41}$$

The relative magnitude of the Hall current density J_H and the axial current density J_z may be compared.

$$J_H = 16 J_z \tag{2.41}$$

Where the derived upper limit of the Bohm diffusion coefficient used to derive equation 2.41 is presented in Equation 2.42 (Lieberman and Lichtenberg).

$$D_b\big|_{max} = \frac{kT_e}{16B} \tag{2.42}$$

The result in Equation 2.41 is often overlooked in the design and study of Hall thrusters, but is critical to understanding the physics that govern the operation of these devices. In a typical 1 kW class Hall thruster, such as the Russian SPT-100, axial current density is approximately 100-200 mA/cm^2 (Sankovic et al.), which implies that the Hall current density is on the order of 4 A/cm^2.

2.2.5 Insulator Wall Effects

The flow within the acceleration channel of a Hall thruster may be classified as a transitional flow with a Knudsen number on the order of unity. The atoms and ions have a

larger probability of striking the dielectric walls than of a collision with another atom, or ion. Neutrals striking the walls will reflect diffusely at the ground state energy. Ions that strike the wall will recombine on the wall surface and leave the surface diffusely at the atomic ground energy state (Redhead et al.). The energy transferred to these ions by the thruster will therefore by lost to the bulk material of the insulator and subsequently radiated away. In order to minimize this loss mechanism, the ionization region must lie close to the exit plane and be as short as possible.

Electrons colliding with any surface may produce secondary electrons. Metals have secondary emission ratios near unity. For insulating materials, the primary electrons are able to penetrate more deeply, and secondary electrons are able to escape from greater depths. Therefore, the secondary electron emission yields of insulators are generally much higher (Alig and Bloom).

Secondary electron emission yield curves have a characteristic shape consisting of a steep rise at low incident electron energies to a maximum yield followed by a slow fall off at higher incident electron energies as shown in Figure 2.4 (Lidde).

Available data for materials typically used in Hall thruster construction are shown in Table 2.1. The first four are metals used in Hall thruster construction. The magnetic circuit is often made of iron, sometimes alloyed with cobalt or nickel, and the electrical connections and magnetic windings are generally copper. The final six materials are insulators which have slightly different secondary emission curves due to larger peak secondary electron emission values, δ_{max}. The second crossover point E_{II} in these cases is beyond the incident electron energies studied (Lide, Alig and Bloom).

Of the dielectric materials in Table 2.1, boron nitride (BN), silica ($Si0_2$), and alumina (Al_2O_3) have been used as insulators within Hall thrusters (Ashkenazy et al., Raitses et al. 1997). The available data for boron nitride and alumina show that the secondary electron yield reaches unity at electron energies of 50 eV and 25 eV, respectively. Both materials have maximum yields in the region of 650 eV with maximum secondary electron emission ratios of 2.9 for boron nitride and 6.4 for alumina. Data for silica is not as complete, but appears to be similar. It should also be noted that secondary electron emission is extremely sensitive to the surface state. Surface layers and contamination significantly alter secondary

electron emission yields. Conducting layers, in particular, are known to drastically reduce secondary electron yields.

Table 2.1. Secondary electron emission yield data for Hall thruster materials.

Material	δ_{max}	E_{max} (eV)	E_I	E_{II}	Ref.
Co	1.2	600	200		Lide
Cu	1.3	400	200	1500	Lide
Fe	1.3	400	120	1400	Lide
Ni	1.3	550	150		Lide
Al_2O_3	6.4 - 19	650 - 1300	25		Dawson
BeO	3.4	2000			Lide
BN	2.9	600	50		Dawson
CaO	2.2	500			Lide
MgO	3 - 15	400 - 1500			Lide
SiO_2	2.1 - 4	400			Lide

The effect of secondary electron emission on thruster operation is not well understood. With relatively high secondary electron emission coefficients, the Hall thruster insulator surfaces are charged in and around the high electron density ionization region. The electrons freed from the insulator will be of a lower energy and will not contribute to the ionization of neutrals, nor do they appear to contribute to cross field diffusion. Due to their low energy, they will be more firmly confined by the magnetic field. However, it has been suggested that a large fraction of the electron diffusion across the radial magnetic field lines is due to secondary emission from the insulator walls which produces a cascade of low energy electrons that eventually reach the anode (Fife et al. 1997).

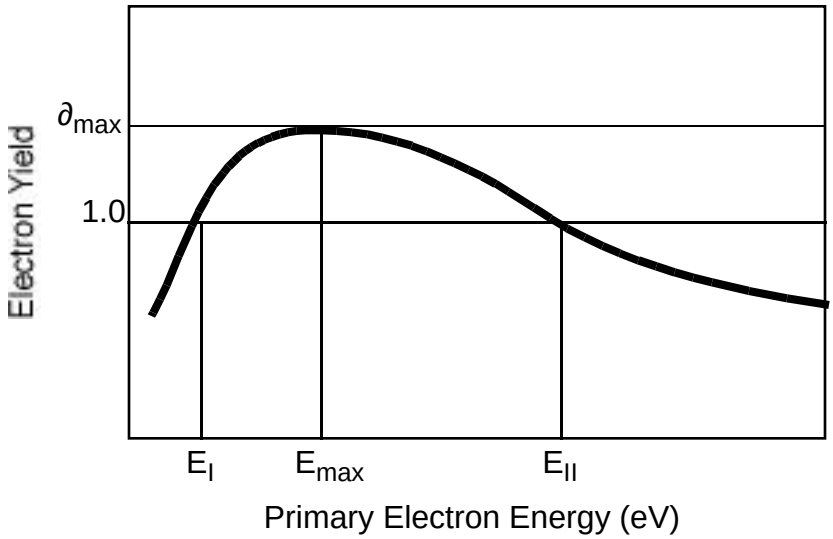

Figure 2.4. Typical shape of a secondary electron emission yield curve. Note that this figure is not to scale. The maximum secondary electron yield is δ_{max}, E_I is the energy at which the secondary electron yield first exceeds unity, the electron energy at which the yield returns below unity is labeled as E_{II}, and the electron energy at which the maximum yield occurs is E_{max}.

The presence of the insulator has a profound effect on the plasma within a Hall type thruster. Secondary emission from the insulator produces a population of low energy electrons in an SPT. Due to these secondary electrons, the potential drop across the sheath adjacent to the insulator wall is small and a large number of high energy primary electrons are able to reach the wall. As confined electrons diffuse toward the anode, they gain energy from the electric field. After an impact with the dielectric insulator walls, these high energy electrons are absorbed and release less energetic secondary electrons. The result is that the dielectric wall limits the temperature of the electrons confined in the ionization region. By limiting the electron temperature, a smooth continuous variation of the plasma potential results.

One class of Hall thruster, the ALT, does not utilize dielectric insulating walls in the acceleration channel. The magnetic pole pieces are exposed to the plasma, but are held at cathode potential to repel stray electrons. As electrons diffuse toward the anode, the bulk electron temperature is not moderated by secondary electrons. Thermal diffusion toward the cathode eventually equals the applied electric diffusion toward the anode. At the point where

this occurs, an abrupt, nearly discontinuous, potential jump occurs in the plasma with the thruster acceleration channel and is referred in the literature as the anode layer (King).

2.2.6 Cathode and Anode Losses

Since the Hall thruster is an electrostatic accelerator, potential drops represent losses detrimental to efficient operation. Previous measurements indicate that a significant potential fall exists within the Hall thruster near the anode especially at high discharge voltages (Morozov et al. 1972). This feature is not completely understood. Since the anode is far from the peak magnetic field, the discharge near the anode may be treated as a glow discharge. The Von Engle theory for a glow discharge predicts that the anode fall will be approximately equal to the ionization potential of the discharge gas and is also known to have weak dependencies on the current and number densities.

$$\Delta V_{anode} \quad \frac{J}{n_N^{\,2}} \tag{2.43}$$

Where ΔV_{anode} is the anode fall, J is the anode current density, and the electron temperature is assumed to be invariant (Brown).

The losses associated with the cathode are not just limited to a potential fall. Since thermionic emission from a hot filament is constrained by surface area and lifetime, hollow cathodes have been the neutralizers of choice. Hollow cathodes have longer lifetimes and support higher current densities than emissive filaments. Unfortunately, approximately 10-15% of the propellant flow is required to operate the hollow cathode. This propellant is not accelerated by the thruster and hence does not contribute to the thrust. In addition, hollow cathodes do not produce electrons at ground potential. Due to the work function of the emitter and the keeper discharge, the electrons are emitted at a potential different than the local ground. The actual cathode potential can also differ between hollow cathodes and due to age. This generally disallows the use of multiple cathodes for very large thrusters, or clusters of thrusters, since the various cathodes will steal electron current from one another (Rusakov et al.).

2.2.7 Thrust Generation and Energy Distribution

The Hall thruster is an electrostatic accelerator in that the ionized propellant is accelerated by electric body forces. The average kinetic energy acquired by each propellant ion E_{kin} is a function of the potential at creation φ_i and final potential φ_f .

$$E_{kin} = \frac{1}{2} m_{Xe} \bar{v}^2 = e(\varphi_i - \varphi_f) \tag{2.44}$$

Where m_{Xe} is the atomic mass of the xenon propellant, and $\bar{v}$ is the average final velocity of the ion stream. Assuming that the velocity is primarily directed in the axial direction, Equation 2.32 may be combined with Equation 2.44 to produce a relation for $\bar{v}$.

$$\bar{v} = \sqrt{2e\frac{(\varphi_i - \varphi_f)}{m_{Xe}}} \tag{2.45}$$

Where it is assumed that the ionization fraction α is unity and multiply charged ions are neglected. The potential difference $(\varphi_i - \varphi_f)$ may be better stated as the difference between the anode potential φ_A and potential φ_{loss} lost in the propellant acceleration.

$$\bar{v} = \sqrt{2e\frac{(\varphi_A - \varphi_{loss})}{m_{Xe}}} \tag{2.46}$$

Taking into account profile losses and losses due to incomplete ionization, an expression for the thrust produced by a Hall thruster may be constructed from Equations 2.32 and 2.46.

$$T = \gamma\delta\dot{m}\sqrt{2e\frac{(\varphi_A - \varphi_{loss})}{m_{Xe}}} + (T_{Ent}) \tag{2.47}$$

Where γ represents losses due to neutral propellant exiting the thruster, δ is representative of the profile losses, and T_{Ent} is the value of additional thrust generated in ground test facilities due to entrainment of background neutrals.

Although some measurements have been made, quantitative values for the various loss mechanisms are unknown. Using the analyses available in the literature, it is possible to determine an energy balance for the 1.35 kW SPT-100 Hall thruster. Emission measurements indicate that the plume of an SPT-100 is approximately 95% ionized with 10-20% of the ions doubly ionized (Manzella 1993). Thermal modeling of the radiative heat transfer of an ALT of similar to the SPT-100 shows that 9% of the input energy is lost as heat to the surroundings (Gakusha et al.). Losses due to the spread in the ion energy distribution are estimated to be approximately 10%. Plume divergence of SPT type thrusters is also considered to be in the neighborhood of 10%. The cost of ionization is thought to be relatively low at 6 to 8 times the ionization potential φ_{ion} (Gavryshin et al.). Figure 2.5 shows a chart of the relative energy output of an SPT-100. The efficiency of the thruster η is taken to be 50%. The thruster is assumed to be operating at 300 volts and a total power of 1.35 kW with 4 mg/s of xenon. The cost of ionizing each ion is taken to be $7\varphi_{ion}$. The thruster exhaust is taken to be 95% ionized with 20% of the ions doubly charged with a φ_{ion} of 21.2 eV.

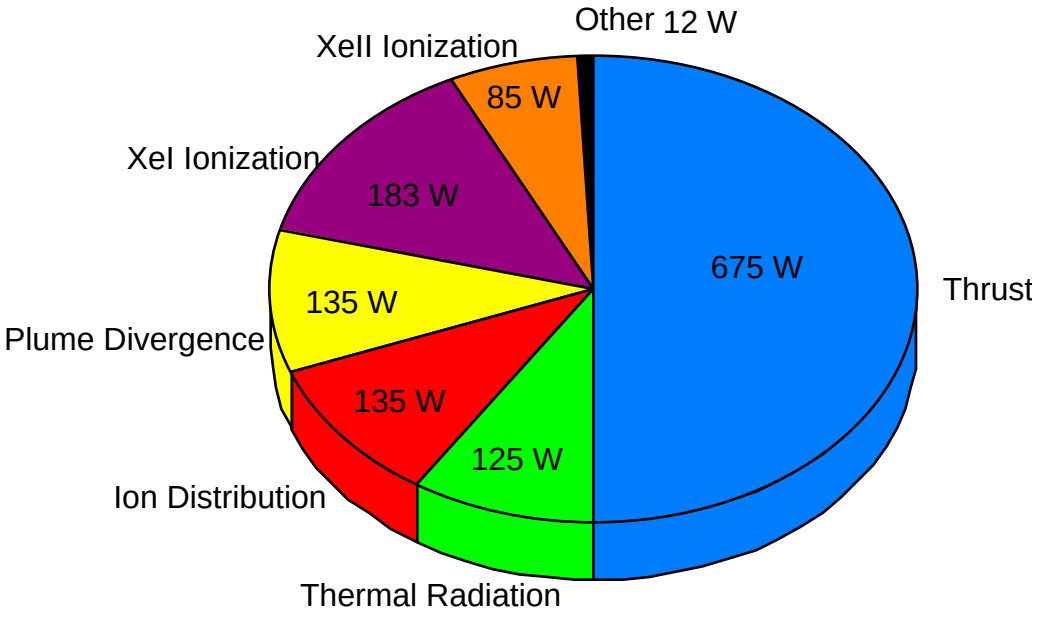

Figure 2.5. Energy output for an SPT-100. Note that 12 W are not accounted for in this analysis.

2.3 Thruster Scaling

Based on the physics presented in the previous section, the scaling of a Hall type thruster may be determined. The first assumption is that the average electron energy, or electron temperature, must be conserved. This quantity is critical to the ionization process and is therefore characteristic of the propellant. Second, the desired voltage will be treated as a design parameter specified at 300V. This is in a comparable range to that of current thrusters that operate at reasonably high efficiencies which produce useful specific impulses.

The assumption of invariant electron temperature is justified if it can be argued that the ratio of the power dissipated to electrons in the discharge is decreased in proportion to the electron energy loss at the wall, which is probably the dominant energy loss mechanism. The wall energy loss rate in a collisionless plasma ε_l (note that drift to the walls is unimpeded by the magnetic field) is simply.

$$\varepsilon_l = \left(\frac{n_e c_e}{4}\right) A_l \left(\frac{3}{2} kT_e\right) \quad n_e T_e^{1.5} A_l \tag{2.48}$$

It is clear that the selection of the appropriate scaling on the loss area A_l and power P as well as the consequence that this has on the electron density is critical to the issue of the invariance in the electron temperature.

If it is desirable to geometrically scale the power of present Hall thrusters by some arbitrary factor ς, then intuition would suggest a corresponding scaling in the mass flow rate.

$$\dot{m} = \rho_N v_N A \tag{2.49}$$

Where A is the area of the acceleration channel, ρ_N is the neutral density near the anode, and v_N is the velocity of the neutral propellant near the anode. A gasdynamic limitation on the flow velocity is established (choked flow), rendering it invariant provided that the temperature of the anode and thruster assembly do not rise appreciably. A decision as to the scaling of the discharge cross sectional area A and its consequences on the density ρ_N is

required. Choosing to scale all geometric lengths by the factor ς, the area therefore scales by the factor ς^2 and the density by the factor ς. Therefore, if the operating power is reduced by a factor of 10, the cross-sectional area is reduced by a factor of 100, and as a consequence, the particle densities throughout the discharge are expected to be higher by a factor of 10. In order to satisfy conditions on the charged particle Larmor radii, Equations 2.23 and 2.24, the shortening of all of the lengths by the factor ς implies that the magnetic field must increase by the factor ς^{-1}. Also, a shorter length will guarantee proper scaling on the ion losses at the wall, and in addition, provide the necessary scaling on the electron energy wall loss. The increased magnetic field necessary for this scaling is not difficult to achieve as it is applied across a magnetic pole spacing that has also been reduced by the scaling factor ς.

Thruster power scaled by the factor ς at a fixed discharge voltage implies a correspondingly scaled total discharge current I. To maintain the same ion current to electron current ratio seen in higher power thrusters implies a proportional scaling of the electron current. The electron current $I_e = J_e A$, where J_e is the axial electron current density, must scale as ς^{-1} due to the chosen scaling of A.

Before determining the appropriateness of this scaling, the mechanisms likely to affect electron transport need to be examined. If crossed-field transport is largely controlled by the effective Bohm mobility, $\mu_B = 1/(16B)$, then $J_e \le (n_e E)/(16B)$ scales with ς^{-1} as a result of the expected scaling in the plasma density n_e. This is consistent with the requirements on the scaling of the electron current density. If the cross field transport is largely controlled by wall collisions, then the effective wall axial conductivity can be approximated.

$$\sigma_w = \frac{n_e e^2 W}{m_e c_e} \tag{2.50}$$

Where Equation 2.50 is scale invariant. However, the axial electron current density is $J_e = \sigma_w \varphi_A / L$ which has the required ς^{-1} scaling, where L is the channel length. So both transport mechanisms support the scaling requirements on the electron current imposed by

the election to scale the area A by ς^2. The electron $\vec{E} \times \vec{B}$ drift velocity is also invariant with this scaling.

In addition, this scaling conserves the ratio of the Hall current to axial electron current, a parameter intuitively expected to be reproduced from one Hall thruster to another. The two properties should be expected to be coupled, especially if Bohm type transport is the controlling cross field transport mechanism. This scaling is also consistent with the axial evolution in the electron and ion current densities, expected due to the production of electrons and ions in the ionization region, as seen by examining the electron conservation equation.

$$\frac{\partial J_e}{\partial z} \approx \frac{J_e}{L} = \int_g R_{ion}(g) \tag{2.51}$$

This scaling, although introducing a reduced residence time associated with the propellant in the channel due to a reduced channel length, introduces a reduced characteristic ionization time, as a consequence of the increased particle densities.

Revisiting Equation 2.48 and the statement of the electron temperature invariance and recognizing the selection to scale all lengths as well as discharge power by the factor ς, we see that the electron energy loss at the wall is also scaled by the factor ς, which would ensure the necessary scaling on the electron temperature.

In summary, the above scaling analysis suggests a number of scaling laws. Nominal design parameters are indicated by the asterisk and a scaling factor denoted by ς. All of the characteristic dimensions of the thruster are also scaled by the factor ς.

$$P = \varsigma P^* \tag{2.52}$$

$$\dot{m} = \varsigma \dot{m}^* \tag{2.53}$$

$$B = \varsigma^{-1} B^* \tag{2.54}$$

$$\varphi_A = \varphi_A^* \tag{2.55}$$

2.4 Hall Thruster Instabilities

Within a Hall thruster, there is an applied radial magnetic field and a resultant electric field. In the vicinity of the peak magnetic field strength, the electrons are constrained to move along the azimuthal coordinate in the direction of the closed $\vec{E} \times \vec{B}$ drift. Hence, Hall thrusters have often been referred to as *closed electron drift accelerators.* However, early researchers recognized that the electron current comprised a larger fraction of the total discharge current than could be accounted for by classical collisional diffusion alone and that an anomalous cross field diffusion of electrons is necessary to account for the enhanced plasma conductivity. An experimental study by Janes and Lowder drew attention to the presence of weakly turbulent density and field fluctuations which give rise to cross field electron transport. These experiments were subsequently followed in the former Soviet Union (Morozov et al., Esipchuk et al. 1974, Esipchuk et al. 1976), where the nature and structure of the plasma turbulence was further resolved and in which the first theoretical analysis of the wave dispersion relations were presented.

The nature of the instabilities that give rise to the unsteady behavior in Hall thrusters is strongly dependent on the sign of the axial gradient in the applied magnetic field (Morozov et al.). There appear to be at least three principle oscillatory modes present in Hall thrusters. At relatively low frequencies (20-60 kHz), traveling azimuthal drift waves, often mislabled as *ionization waves*, exist in the regions of the thruster where the axial gradient in the applied magnetic field $dB/dz < 0$. These waves are predominant when operating along the ionization portion of the current voltage characteristic and are damped in the current saturation operating regime, except for regions very near the anode, where the wave is excited even in cases where $dB/dz > 0$ (Morozov et al.). At moderate frequencies (70-500 kHz), largely turbulent axial waves occur in the regions where $dB/dz > 0$ with frequencies centered at approximately the inverse ion transit times. Therefore, these waves are often referred to as transit time oscillations in the literature (Esipchuk et al. 1974). At high frequencies (MHz), azimuthal waves are evident very near the optimum magnetic field which

is defined as where the discharge current is a minimum for a fixed voltage and propellant flow (Esipchuk et al. 1976).

The precise role played by the oscillatory and turbulent behavior characteristic of these Hall discharges is only qualitatively understood (Choueiri). This behavior is believed to be responsible for not only the cross field diffusion of electrons, but also for the spreading of the ion velocity distribution. However, no evidence has been found that the oscillatory behavior of Hall thrusters produce increased radial electric fields that cause radial divergence of the plume (Esipchuk et al. 1974). Commonly, some of the thruster oscillations have been mitigated by isolation of the thrusters from the power sources. It is shown that the addition of an inductive-capacitive, or resistive-capacitive, circuits will decrease the amplitude of the discharge oscillations and increase thruster efficiency (Randolph et al. 1994). Knowledge of these unsteady plasma mechanisms provide physical insight into a range of performance limiting factors in modern Hall thrusters (Baranov et al.).

Chapter 3. Diagnostic Techniques

3.1 Thrust Measurement

Since a Hall thruster is first and foremost a propulsive device, thrust is the most important measure of performance. Without thrust measurements, the fundamental performance of the device is unknown. Thrust measurements do not provide detailed information on the physics of the thruster, but rather, a temporally and spatially averaged parameter. From a thrust measurement, mean propellant exit velocity, specific impulse, and thrust efficiency may be computed (Hill and Peterson).

$$\bar{v} = \frac{T}{\dot{m}} \tag{3.1}$$

$$I_{sp} = \frac{T}{\dot{m}g} \tag{3.2}$$

$$\eta = \frac{2P}{T\bar{v}} \tag{3.3}$$

Where I_{sp} is the specific impulse, g is Earth's gravitational constant, η is the thrust efficiency, and P is the electrical power dissipated by the thruster. In order to provide a system η, P is the total system power including power dissipated in supporting the hollow cathode discharge and magnetic field. Although, thrust measurements only directly provide information on the efficiency of the thruster as a whole, values of I_{sp}, or $\bar{v}$, are valuable as comparisons with spatially resolved measurements.

Due to the low levels of thrust, generally less than 200 mN, a displacement type measurement of the thrust is preferred. Load cells are not used since they lack sufficient resolution. The most commonly used thrust stand design for electric thrusters is an inverted pendulum design as shown in Figure 3.1 (Crofton).

The inverted pendulum thrust stand consists of two main parts. These are the lower portion which is fixed to the test facility and the upper pendulum portion upon which

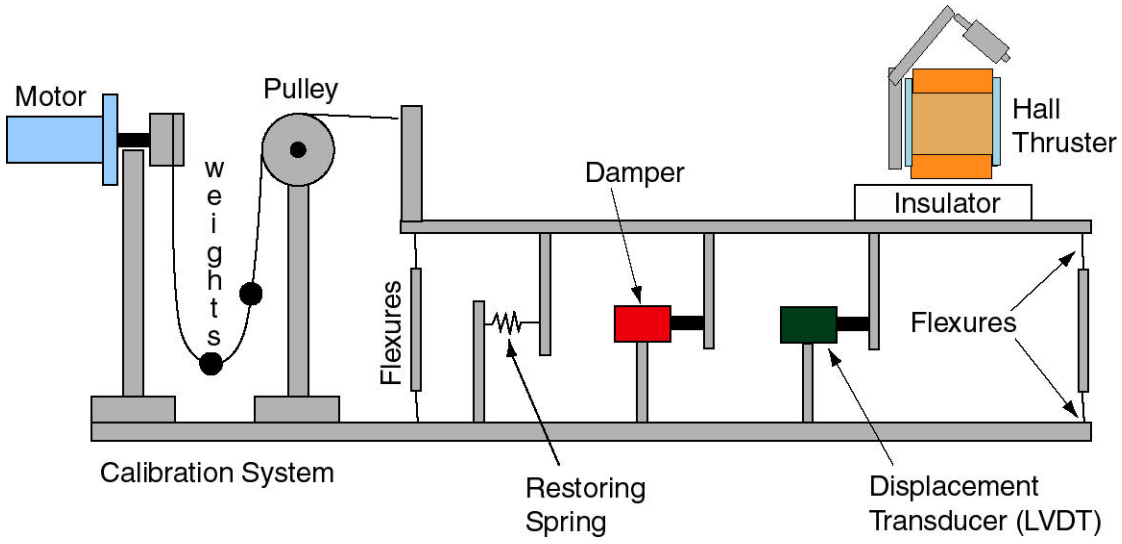

Figure 3.1. Schematic of an inverted pendulum thrust stand.

the thruster is mounted. These two parts are connected by several flexures, a restoring spring, and the propellant feed lines (not shown). The flexures in concert with the restoring spring and the propellant feed lines form a composite spring with an effective spring constant of K. The thruster displaces the inverted pendulum a distance X, and the thrust stand produces a restoring force $F = KX$. Similar to a simple pendulum, gravitational force has a component along the displacement axis given by mgX/H. Where H is the pendulum length and mg is the gravitational force acting on the pendulum. In this case, mg is not a restoring force, but rather a destabilizing force as shown in Equation 3.4.

$$X = \frac{T}{\left(K - \frac{mg}{H}\right)} \tag{3.4}$$

The effective spring constant is adjusted such that the unstable condition of $K = mg/H$ is avoided, but still provides sufficient displacement for high measurement sensitivity. If the denominator of Equation 3.4 is too small, slight variations in the force mg due to minor disturbances such as thrust stand tilt, or hanging cable perturbations, will have a significant influence on the measurements (Crofton).

With the displacement of the inverted pendulum proportional to the thrust, it must be measured accurately, usually with a linear variable differential transformer (LVDT) which measures the change of impedance associated with the relative positions of a stationary coil and an iron core. In this way, X is measured without contact between the inverted pendulum and stationary base. A similar electromagnetic damper restrains oscillations that couple into the thrust stand from the test environment. Stiction, a combination of friction and sticking of thrust stand spring components and flexures, often masks small thrust variations and is overcome by using the damper circuit to induce oscillations between thrust measurements.

Calibration of the thrust stand is performed using an electric motor and pulley system. Weights are suspended from the pulley attached to the inverted pendulum. The electric motor then lowers, or raises, several weights of known mass. The deflection of the thrust stand for a known calibration weight yields a linear displacement X versus calibration force curve.

3.2 Laser Velocimetry

3.2.1 Laser Induced Fluorescence

The interaction of a laser beam with a plasma may involve the optical excitation of a number of atoms to a higher energy state. The excitation is more likely to occur if the laser is tuned to the energy difference $h\nu_{12}$ between two energy states. This interaction can be investigated by either monitoring the resulting reduction in laser power following propagation through the plasma (absorption), or by monitoring the subsequent spontaneous emission as the resulting excited state relaxes to a lower state (laser induced fluorescence, LIF). Monitoring the fluorescence as the laser is tuned over the transition provides a measure of the fluorescence excitation line shape and is preferred due to the higher spatial resolution that it affords in the determination of plasma parameters.

The measured fluorescence signal power S_f for a simple two level model shown in Figure 3.2 is given below for a volume V (Eckbreth).

$$S_f = \eta_d h\nu_{12} N_2 V A_{21} \frac{\Omega}{4\pi} = \eta_d h\nu_{12} \left(\frac{\Omega}{4\pi}\right) N_1^0 V \left(\frac{B_{12}}{B_{21}+B_{12}}\right)\left(\frac{A_{21}}{1+\frac{I_{sat}^{\nu}}{I_{\nu}}}\right) \quad (3.5)$$

Where η_d is the efficiency of the detection system, Ω is the solid angle subtended by the collection optics, I_ν is the incident laser irradiance per unit frequency interval, N_2 is the population of the upper state, N_1^0 is the unperturbed population of lower state, A_{21} is the Einstein coefficient for spontaneous emission, B_{12} is the Einstein coefficient for induced absorption, and B_{21} is the Einstein coefficient for induced emission. The saturation intensity I_{sat}^{ν}, defined as that intensity which produces a fluorescence signal half of what it would be if the fluorescence was linear with irradiance, depends inversely on the line strength of the particular line and is defined in Equation 3.6.

$$I_{sat}^{\nu} = \frac{(A_{21}+Q_{21})c}{B_{12}+B_{21}} \quad (3.6)$$

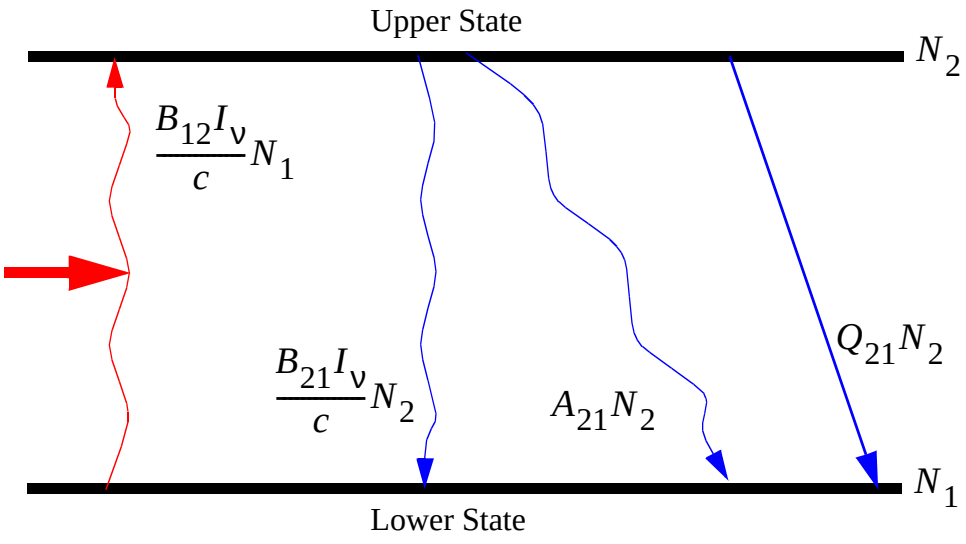

Figure 3.2. Simple two energy level diagram for laser induced fluorescence.

Where Q_{21} is the quenching rate coefficient which is a function of the specific collisional partners and their energies. It is, therefore, dependent on the sample composition and temperature.

At low excitation irradiances where $I_\nu \ll I_{sat}^\nu$, Equation 3.5 simplifies and the fluorescence signal is linearly proportional to the probe beam irradiance.

$$S_f = \eta_d \frac{h\nu_{12}}{c}\left(\frac{\Omega}{4\pi}\right) N_1^0 \; V B_{12} I_\nu \left(\frac{A_{21}}{A_{21} + Q_{21}}\right) \tag{3.7}$$

Where Equation 3.7 holds is often referred to as the linear regime. Conversely, at high excitation irradiances where $I_\nu \gg I_{sat}^\nu$, the fluorescence signal no longer depends on either the quenching rate coefficient or the excitation irradiance.

$$S_f = \eta_d h\nu_{12}\left(\frac{\Omega}{4\pi}\right) N_1^0 \; V \frac{B_{12}}{B_{12} + B_{21}} A_{21} \tag{3.8}$$

In this saturated regime, the rates of laser absorption and stimulated emission become so large that they dominate the state to state energy transfer from pumped levels. Saturation maximizes the fluorescence signal yield. However, complete saturation is difficult to achieve since saturation does not occur in the outer wings of the focussed excitation laser beam and the phenomena is severely complicated by spatial inhomogeneities.

3.2.2 Line Shape

Several factors can affect the line shape and give rise to broadening. In high temperature plasmas, the most significant of these is due to the Doppler effect and gives rise to Doppler broadening which reflects the fact that the absorbing species is distributed in velocity according to the kinetic temperature T_{kin}. When the absorbing species is characterized by a Maxwellian velocity distribution, Doppler broadening results in a Gaussian line shape with a line shape function $g_d(\nu)$ (Eckbreth).

$$g_d(\nu) = \frac{c}{\nu_o}\sqrt{\frac{m_{Xe}}{2\pi kT_{kin}}}\exp\left[-4\ln 2\frac{(\nu-\nu_o)^2}{\Delta\nu_d^2}\right] \tag{3.9}$$

Where v_o is the unshifted transition center frequency. The full width at half maximum (FWHM) Δv_d of the purely Doppler line broadened shape is given in Equation 3.10.

$$\Delta\nu_d = \frac{\nu}{c}\sqrt{\frac{8\ln 2kT_{kin}}{m_{Xe}}} \tag{3.10}$$

Doppler broadening of spectral lines is an example of inhomogeneous broadening. The atoms can be divided into a number of velocity subgroups based on their thermal distribution. The probability of absorption, or emission, of monochromatic radiation at frequency v is not equal for all atoms, but depends on their velocity class (Demtroder).

Collisional interactions between the absorbers and other species in the plasma give rise to spectral line shapes which are Lorentzian in shape. These include interactions with charged particles (Stark broadening) and uncharged particles (van der Waals broadening). The general form of the line shape function $g_c(\nu)$ for a purely collisionally broadened transition with a FWHM of $\Delta\nu_c$ is shown below (Eckbreth).

$$g_c(\nu) = \left(\frac{\Delta\nu_c}{2\pi}\right)\frac{1}{(\nu-\nu_o)^2+\left(\frac{\Delta\nu_c}{2}\right)^2} \tag{3.11}$$

Collisional broadening is an inhomogeneous broadening mechanism. The probability of absorption or emission of radiation of frequency v is equal for all atoms and is not dependent on the thermal velocity as is the case for Doppler broadening (Demtroder).

At conditions where neither Doppler nor collisional broadening dominates, the two line shape functions must be convolved to yield a Voigt profile. The line shape function and associated definitions for a Voigt profile are shown below (Eckbreth).

$$g_v(\nu) = 2\sqrt{\frac{\ln 2}{\pi}}\frac{V(a,x)}{\Delta\nu_d} \tag{3.12}$$

Where.

$$V(a,x) = \left(\frac{a}{\pi}\right)\int_{-\infty}^{\infty}\frac{\exp(-y^2)}{a^2+(x+y)^2}dy \tag{3.13}$$

$$a = \sqrt{\ln 2}\frac{\Delta\nu_c}{\Delta\nu_d} \tag{3.14}$$

$$x = 2\sqrt{\ln 2}\frac{(\nu-\nu_o)}{\Delta\nu_d} \tag{3.15}$$

The measured fluorescence excitation line shape is not necessarily equivalent to the spectral line shape. The line shape is an intrinsic property of the absorbers, whereas the fluorescence line shape is the variation in the detected fluorescence signal with frequency as the laser is tuned across the absorption line feature. If the laser excitation significantly perturbs the populations in the coupled levels, it is said to be saturating the transition and the fluorescence signal is then a nonlinear function of laser intensity. In cases where the laser intensity is significantly below the saturation level and the laser linewidth is small compared to the transition linewidth, the fluorescence excitation line shape reflects the spectral absorption line shape as given by Equation 3.7. When the laser intensity is sufficiently high to saturate the transition, the fluorescence excitation line shape is broader than the spectral line shape and the fluorescence intensity is less than it would be if it were linear with the laser intensity. Stronger transitions have a smaller saturation intensity and thus a larger saturation effect for a given laser intensity. For a purely homogeneously broadened transition, the resulting line shape retains its Lorentzian profile but with an increased half width $\Delta\nu_{csat}$.

$$\Delta\nu_{csat} = \Delta\nu_c \sqrt{1 + \frac{I_\nu}{I^\nu_{sat}}} \tag{3.16}$$

Where the saturation parameter, I^ν_{sat} / I_ν represents the ratio of the pumping rate to the average relaxation rate for the two level model in Figure 3.2. The FWHM of a saturation broadened homogeneous line shape increases with the saturation parameter of the line center (Demtroder).

For inhomogeneously broadened transitions, the behavior of saturated line shapes is significantly more complex. When a monochromatic beam of light passes through a sample of atoms at with a thermal distribution at T_{kin}, only the atoms in one particular velocity subclass will be able to interact with the incident radiation. If the intensity of the radiation is large enough to saturate the transition, it will deplete the lower level velocity subclass. If the radiation is scanned across the transition, the result will be a Voigt profile similar to Equation 3.12 with a modified saturation broadened line width (Demtroder).

Local electric and magnetic fields can also affect the spectroscopy of a transition and its line shape. Zeemann splitting occurs when a magnetic field splits each fine, or hyperfine, feature into a number of lines by separating formerly degenerate energy states. In a similar manner, an electric field may also cause splitting of spectral lines known as Stark splitting. Furthermore, perturbations of an atom's energy levels by nearby charged particles lead to a type of pressure broadening and a shift of a spectral line position (Griem 1974).

3.2.3 Doppler Shift

If an absorber has a velocity component v along the axis of the laser beam, it will absorb the light at a frequency shifted from that of stationary absorbers due to the Doppler effect. The magnitude of the frequency shift $\delta\nu_{12}$ depends on the absorber's velocity v along the laser beam propagation vector.

$$\delta\nu_{12} = \nu_{12}\frac{v}{c} \tag{3.17}$$

The shift of a species' fluorescence profile away from the line center ν_{12} of the stationary absorbers is in proportion to the species velocity. This effect is similar to the Doppler broadening discussed in section 3.2.2, but where the velocity distribution is shifted by a bulk velocity v. The value of $\delta\nu_{12}$ can be used to determine the bulk velocity of the flow regardless of spectral line shape broadening.

3.3 Xenon Spectroscopy

3.3.1 Hyperfine Splitting

When individual atomic transitions are examined with spectral apparatus of the highest possible resolution, many are split into a number of components lying close together with a total width not exceeding 2 cm^{-1}. This spectral structure is called hyperfine splitting and is caused by the properties of the atomic nucleus. Most elements possess several naturally occurring isotopes. Each isotope has the same number and arrangement of optical electrons, and the same basic spectra. However, each isotope has a different mass. Quantum mechanical calculations indicate that for elements lighter than neon the isotope shifts can be explained of the basis of mass alone. A calculation of this sort will provide a solution correct to within an order of magnitude. Considering the change of mass alone for heavy atoms, the isotope shifts should decrease as the nuclear mass increased, since the motion of the nucleus would become less important. Yet, elements with high atomic masses still exhibit larger than expected isotope shifts. For heavier atoms, the isotope shifts are due to the change in charge nuclear density (Herzberg).

In many cases, isotope shifts are not sufficient to fully explain the observed hyperfine structure. The number of hyperfine spectral features is often considerably greater than the number isotopes (Herzberg). Many nuclei which have an odd number of protons and/or an odd number of neutrons possess an intrinsic nuclear spin $\boldsymbol{I}\hbar$. Where $\boldsymbol{I}$ is integral, or half-integral, dependent on whether the atomic mass is even or odd, respectively (Cowan). For nuclei with nuclear spin, there exists an interaction of the nucleus with the electron shell. The interaction leads to the splitting of levels with angular momentum $\boldsymbol{J}$ into a number of components, each corresponding a specific value of the total angular momentum $\boldsymbol{F}$ (Sobelman).

$$\boldsymbol{F} = \boldsymbol{I} + \boldsymbol{J} \tag{3.18}$$

As a result of this interaction, $\boldsymbol{F}$ is a conserved quantity while $\boldsymbol{I}$ and $\boldsymbol{J}$ are not. The interaction is very small allowing the hyperfine splitting of each level to be taken independently. The number of nuclear spin split hyperfine components is $2I + 1$ if $J \geq I$ and $2J + 1$ if $J < I$ with F values shown below (Sobelman, White).

$$F = J + I, J + I - 1, \quad , |J - I| \tag{3.19}$$

In turn, the selection rules for F are given below.

$$\Delta F = 0, \pm 1 \tag{3.20a}$$

$$\Delta F \neq 0 \text{, if } F = 0 \tag{3.20b}$$

Two constants are associated with hyperfine nuclear spin splitting. These are the A hyperfine structure constant which represents the nuclear magnetic dipole effect on the atom, and the B hyperfine structure constant which is associated with the nuclear electric quadrapole moment of the atom which will only be present if $I \geq 1$. The relative energy of the spin split states depends on the sign of A. In atoms with $A > 0$, the state with the highest value of F has the highest energy. While for atoms with $A < 0$, the state with the lowest value of F has the highest energy (White). The energy level shift ΔE_M associated with the magnetic dipole of the nucleus is given by Cowan.

$$\Delta E_M(F) = \frac{1}{2}A[F(F+1) - J(J+1) - I(I+1)] = \frac{A}{2}C \tag{3.21}$$

Additionally, the energy spacing between successive levels $F - 1$ and F may be shown to be proportional to F.

$$\Delta E_M(F) - \Delta E_M(F-1) = AF \tag{3.22}$$

If $I \geq 1$, the nucleus will have an electric quadrapole moment and a related hyperfine splitting constant B which produces an additional hyperfine splitting with energy linear in $C(C+1)$ where C is defined in Equation 3.21.

$$\Delta E_F = \Delta E_M + \Delta E_Q = \frac{AC}{2} + B\left[C(C+1) - \frac{4}{3}J(J+1)I(I+1)\right] \tag{3.23}$$

Where ΔE_F is the combined nuclear spin split energy level shift combining the effect from the nuclear magnetic dipole moment ΔE_M and the effect of the electric quadrapole moment ΔE_Q (Cowan). It should be noted that the center of gravity of the hyperfine levels lies at a position of the unsplit level J (Sobelman).

$$\sum_F (2F+1)\Delta E_F \tag{3.24}$$

Due to close energy spacing of nuclear spin split levels, near ideal coupling between $\boldsymbol{I}$ and $\boldsymbol{J}$ occurs in most hyperfine structure. Therefore, the intensity rules derived in the literature for Russel-Saunders coupling are appropriate for hyperfine splitting (White).

For where $J-1 \rightarrow J$,

$$F-1 \rightarrow F:\ S = \kappa\frac{(J+F+I+1)(J+F+I)(J+F-I)(J+F-I-1)}{F} \tag{3.25a}$$

$$F \rightarrow F:\ S = -\kappa\frac{(J+F+I+1)(J+F-I)(J-F+I)(J-F-I-1)(2F+1)}{F(F+1)} \tag{3.25b}$$

$$F+1 \rightarrow F:\ S = \kappa\frac{(J-F+I)(J-F+I-1)(J-F-I-1)(J-F-I-2)}{(F+1)} \tag{3.25c}$$

For where $J \rightarrow J$,

$$F-1 \rightarrow F: S = -\kappa \frac{(J+F+I+1)(J+F-I)(J-F+I+1)(J-F-I)}{F} \quad (3.26a)$$

$$F \rightarrow F: S = \kappa \frac{[J(J+1)+F(F+1)+I(I+1)]^2(2F+1)}{F(F+1)} \quad (3.26b)$$

$$F+1 \rightarrow F: S = -\kappa \frac{(J+F+I-2)(J+F-I+1)(J-F+I)(J-F-I-1)}{(F+1)} \quad (3.26c)$$

Where S is the transition strength and κ is an arbitrary constant (White).

Table 3.1. Hyperfine spin splitting constants for Xe I and Xe II.

Species	State	A_{129} (MHz)	A_{131} (MHz)	B_{131} (MHz)	Source
Xe I	$6s[3/2]_2^0$	-2384 ± 2	707 ± 1	525 ± 2	Giessen et al.
Xe I	$6p[3/2]_2$	887 ± 1	265 ± 3	30 ± 3	Fischer et al.
Xe II	$5d[3]_{7/2}$	-502 ± 4	150 ± 2	70 ± 13	Brostrom et al.
Xe II	$6p[2]_{5/2}$	-1633 ± 11	487 ± 4	-129 ± 16	Brostrom et al.
Xe II	$6p[3]_{7/2}$	-1387 ± 9	409 ± 2	-117 ± 10	Brostrom et al.
Xe II	$6p[3]_{5/2}$	-1164 ± 5	346 ± 2	-230 ± 11	Brostrom et al.

The relative intensities of the isotope shifted transitions are proportional to each isotopes relative abundance. However, the relative intensities of the nuclear spin split hyperfine splitting are governed by two summation rules (Sobelman). First, the sum of the intensities of all the lines of the hyperfine structure of a transition $J \rightarrow J'$ originating from a component F of the level J is proportional to the statistical weight of this component,

$(2F + 1)$. Second, the sum of the intensities of all the lines of the hyperfine structure the transition $J \rightarrow J'$ ending on the component F' of the level J' is proportional to the statistical weight of this component, $(2F' + 1)$. With these two sum rules, a system of linear equations are solved for the relative intensities of the nuclear spin split components of each isotope.

3.3.2 Xenon Transitions

The ground state of the xenon atom is not easily accessible to LIF with currently available laser wavelengths, it is therefore advantageous to probe more easily accessed excited states. One neutral and one ionic transition were chosen primarily due to their accessibility by available lasers.

The spectroscopy of the neutral xenon $6s[3/2]_2^0 - 6p[3/2]_2$ transition at 823.2 nm examined in this study is discussed extensively by Cedolin. The conventional Racah notation for the inert gases is used to denote the energy levels. With their natural abundances, nuclear spin, and isotopic shifts given in Table 2.1, the nine stable xenon isotopes each have a slight difference in their transition energies corresponding to their different masses and nuclear charge density. The odd mass isotopes are further spin split due to nuclear magnetic dipole and nuclear electric quadrapole moments. The isotopic and nuclear-spin effects contributing to the hyperfine structure cause the $6s[3/2]_2^0 - 6p[3/2]_2$ transition to consist of 21 lines.

The only ionic xenon transitions for which the hyperfine spin splitting constants are known are those arising from the metastable $5d[3]_{7/2}$ state presented in Table 3.2. In the case of the $5d[3]_{7/2} - 6p[2]_{5/2}$ transition at 605.1 nm, the combined isotopic and nuclear-spin effects cause this transition to have 19 isotopic and hyperfine components contributing to its line shape. Nonresonant fluorescence of the $6s[2]_{5/2} - 6p[2]_{5/2}$ transition at 529.2 nm, which has the same upper state as the 605.1 nm transition, is collected to eliminate noise associated with reflections of the probe beam (Brostrom et al., Hansen and Persson).

For LIF measurements focused on determining the velocity of the plasma flow, it is convenient to probe more accessible transitions for which there is incomplete knowledge of the isotopic and nuclear spin splitting constants. Manzella has shown that the ionic xenon

Table 3.2. Xenon natural isotope abundances, nuclear spins, and representative isotope shifts for Xe I and Xe II transitions relative to ^{132}Xe in MHz.

Isotope	% Natural Abundance	Nuclear Spin, *I*	Xe I 823.2 Isotope Shift	Xe II 605.1nm Isotope Shift
^{124}Xe	0.10	0	270 ± 12	336.6 ± 3.9
^{126}Xe	0.09	0	189 ± 12	252.4 ± 3.9
^{128}Xe	1.91	0	117 ± 12	172.0 ± 6.8
^{129}Xe	26.4	1/2	123 ± 18	113.7 ± 5.0
^{130}Xe	4.1	0	54 ± 12	83.6 ± 4.5
^{131}Xe	21.2	3/2	81 ± 18	16.7 ± 5.0
^{132}Xe	26.9	0	0	0
^{134}Xe	10.4	0	-30 ± 12	-75.8 ± 4.0
^{136}Xe	8.9	0	-147 ± 12	-140.9 ± 7.3
Source	Lidde	Cowan	Jackson and Coulombe 1973	Boughs et al. Bingham et al.

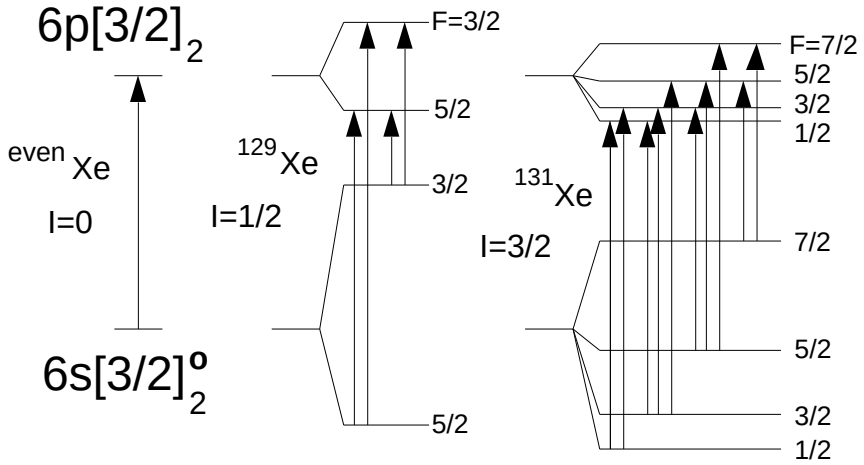

Figure 3.3. Nuclear spin splitting of the $6s[3/2]^0_2 - 6p[3/2]_2$ transition of neutral xenon at 823.2 nm.

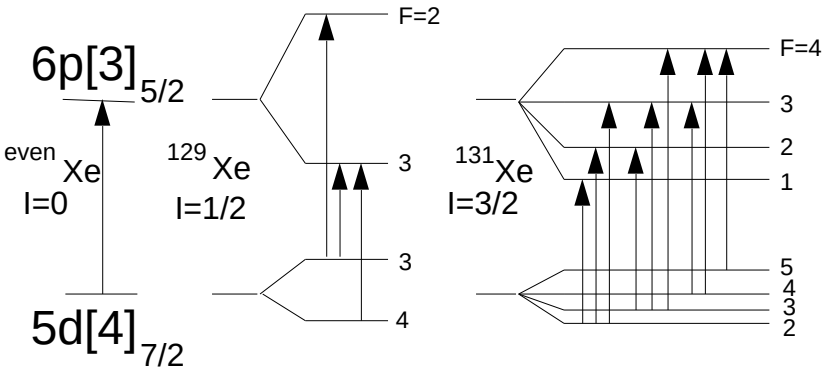

Figure 3.4. Nuclear spin splitting of the $5d[4]_{7/2} - 6p[3]_{5/2}$ transition of singly ionized xenon at 834.7 nm. This diagram is also valid for the $5d[3]_{7/2} - 6p[2]_{5/2}$ transition at 605.1 nm.

transition $5d[4]_{7/2} - 6p[3]_{5/2}$ at 834.7 nm can be used to make velocity measurements in the plume of a Hall thruster. For this transition, the combined isotopic and nuclear-spin effects produce 19 isotopic and hyperfine components. While the upper $6p[3]_{5/2}$ state is well characterized, the $5d[4]_{7/2}$ lower state isotopic and hyperfine structure remain unknown. An additional convenient feature of this transition is a strong line emanating from the same upper state, the $6s[2]_{3/2} - 6p[3]_{5/2}$ transition at 541.9 nm which allows for non-resonant fluorescence collection.

It should be noted that the $5d[4]_{7/2} - 6p[3]_{5/2}$ ionic transition has an interesting history. In the original analysis of the Xe II spectrum by Humpreys in 1939, it was incorrectly identified. The value of J for the lower $5d[4]_{7/2}$ level was incorrectly identified as $5/2$ by Humphreys. This was discovered in 1976 (Garpman and Spector) and corrected in 1987 (Hansen and Persson). Although the value of J is listed correctly as $7/2$ in the most current literature, the initial misidentificaiton of the lower level has propagated into various references. For example, the incorrect spectral data was incorporated into the standard tables available for atomic energy levels (Moore).

3.3 Emissive Plasma Potential Probe

3.3.1 Characteristic of a Swept Probe

A conducting surface immersed in a plasma and biased with potential φ to draw a current I is one of the earliest plasma diagnostics developed for low pressure plasma discharges. This sort of probe is referred to as a Langmuir probe (Lieberman and Lichtenberg). Although it is relatively simple to obtain a model current-potential trace from a Langmuir probe as shown in Figure 3.5, the use of Langmuir probes is limited to a strict set of plasma conditions prevailing in low pressure discharges. These assumptions include that the plasma be stationary, the probe is nonemitting, and that no local fields affect the charged particle trajectories. The probe dimensions must also be much smaller than the mean free paths of the charged particles in plasma. Alternatively, the Debye length λ_D of the plasma can be used as a characteristic length.

$$D_{probe} < \lambda_D = \left(\frac{\varepsilon_o k T_e}{n_e e^2} \right)^{1/2} \tag{3.27}$$

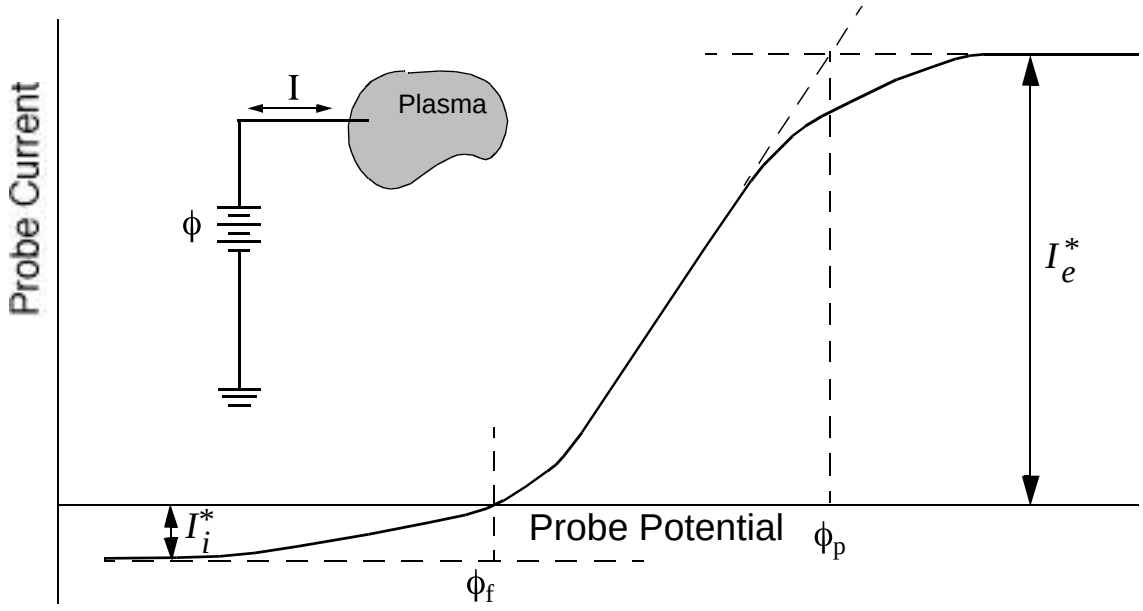

Figure 3.5. Current-voltage characteristic of a swept Langmuir probe including a diagram of a basic swept probe circuit.

Where D_{probe} is the probe diameter. In this case, the probe collects the plasma ions and electrons under essentially collision free conditions. Also, the sheath thickness is treated to be much less than the probe diameter so that the sheath can be treated as a plane (Mitchner and Kruger).

The appearance of the current-potential characteristic of a typical Langmuir probe is also shown in Figure 3.5. The probe current is defined as positive for flow from the electrode into the plasma and is equivalent to electron current from the plasma. The potential φ is the probe potential relative to an arbitrary ground, usually the metallic chamber surrounding the plasma. The floating potential φ_f is defined as the point in the characteristic where the net current is zero. At this point in the characteristic, the currents due to ion and electron flux to the surface of the probe exactly cancel. If the probe is biased negative with respect to φ_f, more ions than electrons will reach the probe surface resulting in a negative net electron current. If the probe is biased sufficiently negative, all the electrons will be repelled and the probe current will approach a nearly constant ion saturation current I_i^*. When the probe is biased positive relative to φ_f, more electrons than ions will be collected, resulting is a positive probe current I. The electron current will continue to rise until the probe potential reaches the plasma potential φ_p. At this point in the probe characteristic, electrons reach the probe surface unimpeded. This higher current is due to the greater mobility of the electrons relative to the heavier and cooler ions. At probe potentials above φ_p, the ions are repelled and I approaches the electron saturation current I_e^*. It should be noted that the probe currents in the saturated portions of the characteristic are not constant, but rather continue to increase slowly in magnitude. This is attributed to an increasing sheath thickness, resulting in a larger effective collection area for the probe (Mitchner and Kruger).

The probe characteristic may be divided into two portions. For the $\varphi \leq \varphi_p$ region where electrons are repelled, the relation for the probe current I is given by the difference between the freely diffusing random ion flow and the retarded electron flow.

$$I = I_e^* \exp\left[\frac{-e(\varphi_p - \varphi)}{kT_e}\right] - I_i^* \tag{3.28}$$

While in the ion retarding region where $\varphi \geq \varphi_p$, I is instead given by the difference between the freely diffusing random electron flow and the retarded ion flux.

$$I = I_e^* - I_i^* \exp\left[\frac{-e(\varphi - \varphi_p)}{kT_i}\right] \tag{3.29}$$

Consistent with the assumptions leading to Equations 3.28 and 3.29, the electron saturation current I_e^* and the ion saturation current I_i^* are given by their respective random one way particle flux.

$$I_e^* = Ae\frac{n_e \bar{c}_e}{4} \tag{3.30}$$

$$I_i^* = Ae\frac{n_i \bar{c}_i}{4} \tag{3.31}$$

Where A is the plasma exposed probe area, $\bar{c}_e$ is the electron mean thermal speed, and $\bar{c}_i$ is the ion mean thermal speed. It should also be noted that the plasma is assumed to be quasi-neutral which is represented as $n_i = n_e$. It should be noted that Equation 3.31 is only valid if the ions are in collisional equilibrium. In diffuse plasmas, this is generally not the case and the ion flux ($n_i \bar{c}_i / 4$ for a collisional plasma) is approximated by the product of the ion density and the ion velocity at the sheath.

These results may be applied to obtain information of various plasma parameters. For example, the electron temperature T_e may be determined by the slope of the line of $\ln(I + I_i^*)$ versus φ in the electron repulsion regime near the floating potential φ_f. Once the electron temperature is known, the electron number density can be determined from Equation 3.30, or from Equation 3.31 if the plasma is isothermal (Mitchner and Kruger).

3.3.2 Characteristic of an Emissive Probe

An electron emitting, or emissive, probe may also be used to measure plasma parameters. These probes require thermionic emission of electrons from the probe surface;

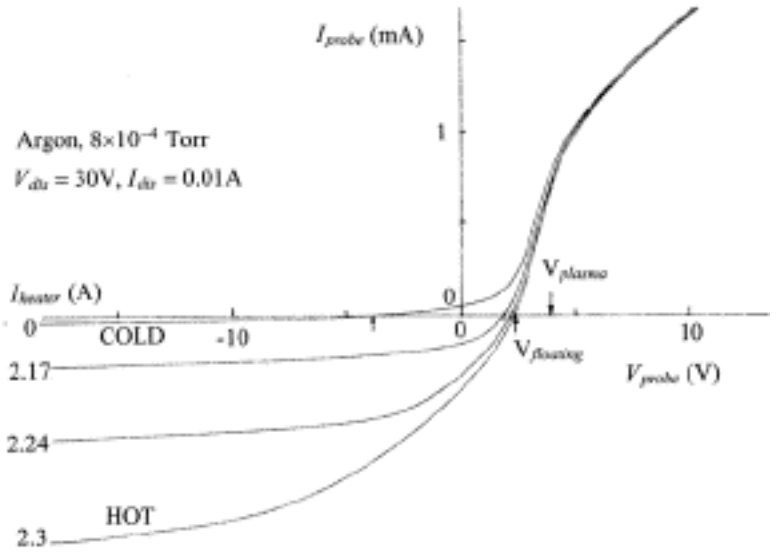

Figure 3.6. Current-potential characteristic of an emissive probe (Wong).

and therefore, have the disadvantage of requiring a separate circuit utilizing high currents to heat a filament. Since the probe is actively heated, it is less subject to contamination, a serious problem for measurements performed with nonemitting probes (Lieberman and Lichtenberg).

The temperature T_f of the electrons from the heated filament is close to the wire temperature. Therefore, there is a resulting sharp change in the probe current as the probe potential passes through the plasma potential φ_p. This is evident from the relations for the filament emission current I_{ef}.

$$I_{ef} = I_{ef}^{o} \exp\left[\frac{-e(\varphi_p - \varphi)}{kT_f}\right] g_{ef}(\varphi - \varphi_p) \text{ Where } \varphi \le \varphi_p \tag{3.32}$$

$$I_{ef} = I_{ef}^{o} \quad \text{Where } \varphi \ge \varphi_p \tag{3.33}$$

Where I_{ef}^{o} is the saturated filament emission current, T_f is the filament temperature, and g_{ef} is a constant that is can be shown to be approximately $\sqrt{1 + e(\varphi - \varphi_p)/(kT_f)}$ (Hershkowitz).

Figure 3.6 shows several swept traces of an emissive probe in a low pressure argon glow discharge. Each trace corresponds a different filament temperature. As the filament is heated, it emits more electrons and I_{ef}^{o} is increased as illustrated in Figure 3.6. The floating potential shifts toward the plasma potential. The larger the emission current, the closer φ_f will be to φ_p. If the probe is left to float with substantial emission current, it is possible to measure the plasma potential nearly instantaneously (Wong).

$$\vec{E} = -\ \varphi_p \tag{3.34}$$

Emissive probes are often used to determine electric fields within a plasma. Measurements of the electric field can be made using a cold probe floating potential φ_f in place of φ_p, but these measurements are generally too ambiguous. Gradients in the value of φ_f measured by a nonemissive probe are very sensitive to gradients of the electron temperature and density. However, the difference between φ_f and φ_p can be used to estimate the electron temperature (Wong).

The relationship between the plasma potential φ_p and the floating potential φ_f can be determined for a floating emissive probe in a collisionless plasma by examining the relations for the ion flux Γ_i and electron flux Γ_e.

$$\Gamma_i = n_s u_s \tag{3.35}$$

$$\Gamma_e = \frac{n_s \bar{c}_e}{4} \exp\left[\frac{-e(\varphi_f - \varphi_p)}{kT_e}\right] \tag{3.36}$$

Where n_s is the plasma density at the sheath edge and u_s is the drift velocity of the ions at the sheath edge. Several assumptions are required for Equations 3.35 and 3.36 to be valid. First, the ion flux is assumed to be constant. Second, the electron flux to the surface is retarded by a sheath which affects only the electrons. An estimate for the sheath edge ion velocity is obtained from the Bohm criterion (Lieberman and Lichtenberg).

$$u_s \geq u_B = \sqrt{\frac{kT_e}{M}} \tag{3.37}$$

Where M is the ion mass and u_B is the Bohm drift velocity. Strictly, the above relation only applies to a collisionless, field free, stationary plasma. However for the more generalized case, it does provide a lower bound estimate of the speed of the ions entering the sheath.

In the case of a floating conductor immersed in a plasma, the difference between the plasma and floating potentials can be determined by equating Γ_i and Γ_e, and substituting u_B for u_s.

$$\varphi_f - \varphi_p = -\frac{kT_e}{e}\ln\left[\frac{M}{2\pi m_e}\right]^{1/2} \tag{3.38}$$

Therefore, if both the plasma and floating potentials are known, an approximation to the lower bound of the electron temperature may be determined (Lieberman and Lichtenberg).

3.4 Plasma Emission

3.4.1 Thermal Equilibrium Considerations

The integrated emission from an excited state is given by an equation similar to Equation 3.5.

$$S_f = \eta_d h\nu_{12} N_2 V A_{21} \frac{\Omega}{4\pi} \tag{3.39}$$

Since there is no external optical pumping, $I_\nu = 0$. The relation of the upper state population N_2 to the populations of other states is no longer clear. If there are sufficient collisions between the particles, equilibrium will result in the population of each state N_j described by a Maxwell-Boltzmann distribution at a temperature T (Vincenti and Kruger).

$$N_j = N\frac{g_j \exp\left(\frac{-\varepsilon_j}{kT}\right)}{\sum_i g_i \exp\left(\frac{-\varepsilon_i}{kT}\right)} \tag{3.40}$$

Where g_i is the degeneracy of the i^{th} energy level, N is the total population, and the denominator is known as the partition function.

Often in low pressure plasmas, there are insufficient collisions to allow the energy levels to equilibrate. In addition, the various species are not necessarily in equilibrium with one another. Electrons, due to their high mobility, are often the most energetic particles in a plasma. Their low mass makes collisional energy transfer with heavier particles inefficient. Therefore while it is relatively easy to transfer energy into electrons, it is difficult to transfer energy to the other plasma particles. Thus, the electrons are more likely to be in equilibrium with a separately defined electron temperature T_e. For heavy particles, the concept of temperature becomes ambiguous if Equation 3.40 is no longer valid. Each energy state in the partition function can then be described as having a distinct temperature. For example, neutrals in the highly excited states of low pressure plasmas are most likely to have been created by recombination of ions with free electrons. The upper states will subsequently not be in equilibrium with the lower states (Griem 1964, Mitchner and Kruger). Emission measurements in the near field plume of a SPT-100 Hall thruster have shown that highly nonequilibrium conditions prevail (Manzella 1993).

3.4.2 Corona Equilibrium

From Equation 3.40, it is evident that in highly nonequilibrium plasmas emission measurements can be used to determine the relative, or absolute, populations of excited states. Without a model of the behavior of the excited states, it is nearly impossible for any determination of plasma parameters to be made. The corona model for equilibrium assumes that the upper states are produced by collisions and depopulated by radiative decay (Griem 1997). The plasma must then be optically thin so that radiation escapes the system. In the simplest application of a collisional radiative model, a two level system like that in Figure 3.7 can be envisioned where a rate equation determines the number densities n_1 and n_2 of

the lower and upper states, respectively. The collisional excitation mechanism in this case is limited to the collisions with the more mobile electrons with density n_e.

$$\frac{dn_2}{dt} = n_1 n_e S^{1 \to 2} - n_2 A_{21} \tag{3.41}$$

Where $S^{1 \to 2}$ is the electron collisional excitation coefficient for the lower state which is a function of T_e. A reasonably good choice for the cross-section is the Seaton cross-section for electronic excitation which after integrating over all electron energy classes yields a value for $S^{1 \to 2}$ (Seaton).

$$S^{1 \to 2} = \frac{1.6 \times 10^{-11} f_{12}}{\sqrt{T_e}\varepsilon_{12}} \exp\left(\frac{\varepsilon_{12}}{T_e}\right) g_G \tag{3.42}$$

Where ε_{12} is the energy level difference between levels 1 and 2, f_{12} is the oscillator strength of the transition, and g_G is the mean Gaunt factor accounting for quantum mechanical effects. Note that in Equation 3.42, ε_{12} and T_e are specified in electron volts (eV).

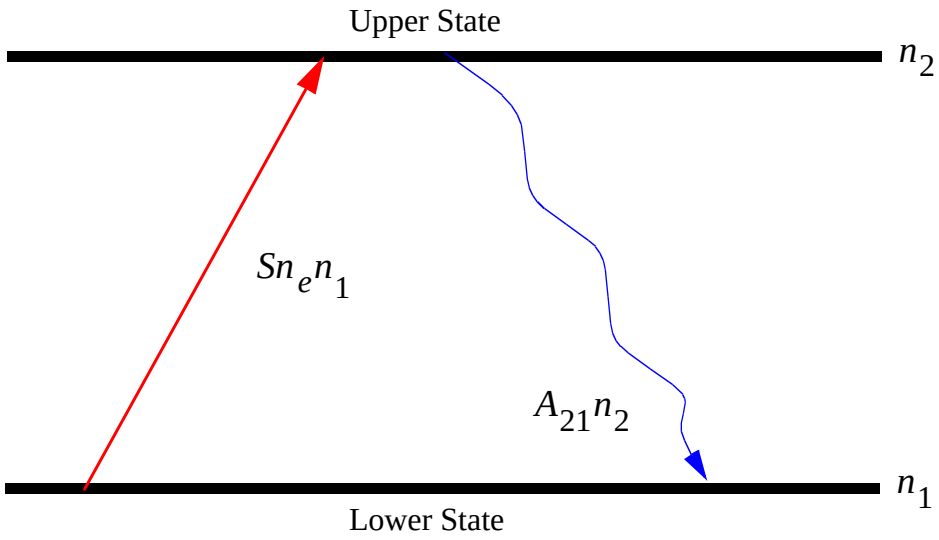

Figure 3.7. Simple two energy level diagram for corona equilibrium.

Assuming steady state conditions, the left hand side of Equation 3.41 may be set to zero and solved for the electron number density n_e.

$$n_e = \frac{n_2 A_{21}}{S^{1 \to 2} n_1} \tag{3.43}$$

With emission data from the upper electronic state to determine n_2, electron temperature data to determine $S^{1 \to 2}$, and an estimate of n_1, a reasonable estimate of the electron number density may be made.

A model such as described by Equations 3.41 through 3.43 would ideally be performed on a ground state transition. For xenon, these lie in the vacuum ultraviolet and are not readily accessible. An alternative is to consider an electronic transition to a metastable state for which electric dipole radiative decay is forbidden. Generally, the optical emission of these states is more accessible. The neutral xenon $6s[3/2]_2^0 - 6p[3/2]_2$ transition at 823.2 nm is one of the brightest features in the spectrum of xenon. The lower $6s[3/2]_2^0$ state is metastable and has a measured lifetime of 42.3 seconds (Walhout et al. 1994). For the purposes of a two level corona model, the $6s[3/2]_2^0$ state may be considered a virtual ground state.

Alternatively under corona equilibrium if the fractional excited state population is small, spectral line intensities are simply proportional to the electron density. This is true for transition energies less than the mean electron energy. Otherwise, the collisional excitation rate coefficient is strong function of T_e (Griem 1997).

Chapter 4. Experimental Apparatus

4.1 Prototype Hall Thruster

4.1.1 Design of Prototype Hall Thruster

A prototype Hall thruster was designed and constructed in the Fall of 1995 and first operated in early 1996. The general design is similar to other laboratory Hall thrusters (Brown and Pinsly, Szabo and Pollard). Shown in Figure 4.1, the thruster consists of a central north magnetic pole and outer south pole enclosing a toroidal insulated acceleration channel annulus 12 mm wide and 15 mm deep. The south magnetic pole is generated by four outer windings supporting the front plate. One central winding generates the north magnetic pole and also structurally supports the alumina (Al_2O_3) electrical insulator. The magnetic circuit is constructed using mild steel for the magnet cores and commercially pure iron for both the front and rear plates. The outer windings consist of cores 95 mm long with a 6.5 mm diameter wrapped with 6 layers of 22 gauge kapton insulated copper magnet wire. The resulting magnetic field has an approximate maximum value of 90 G at the maximum rated winding current of 2.0 A. The thruster dimensions, not including the hollow cathode neutralizer, are approximately 100 x 120 x120 mm.

The cast alumina electrical insulator with an acceleration channel 12 mm wide supports the 90 mm diameter stainless steel anode. Propellant distribution through the anode is accomplished by 32 evenly distributed holes each with a diameter of 0.5 mm. The anode is secured from below the insulator by 4 stainless steel bolts (not shown) which also provide electrical and propellant access. The anode is 15 mm below the furthest extension of the insulator. The cathode used to neutralize the ion beam is an Ion Tech, Inc. HCN-252 commercial hollow cathode capable of producing a maximum emission current of 5 A. It is mounted to the rear of the thruster on a stainless steel bracket so that the cathode exit is 2 cm beyond the thruster exit plane.

Figure 4.2 shows current-voltage traces typical to the prototype Hall thruster operating on xenon propellant. The constant discharge voltage region at lower anode current

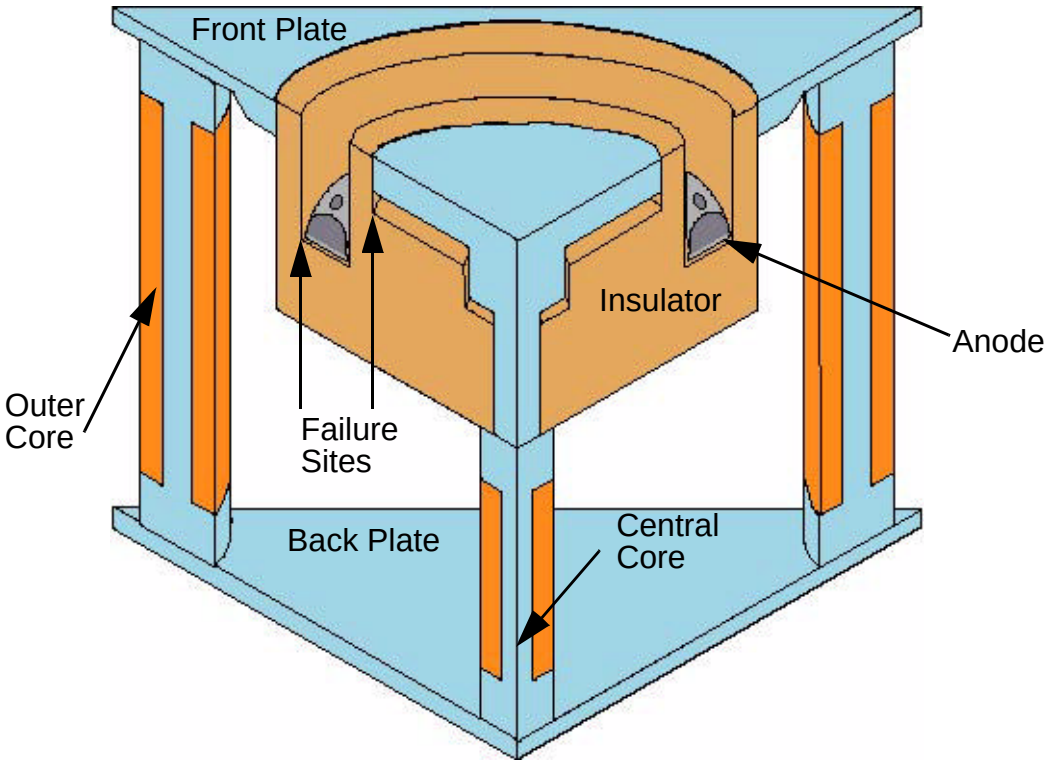

Figure 4.1. Isometric view of the prototype Hall thruster.

is the portion of the characteristic where incomplete ionization is occurring. The main feature is a transition from near constant current operation to near constant voltage operation. This portion of the characteristic corresponds to the threshold of nearly complete ionization of the propellant (Morozov et al. 1972). The transition is more clearly defined for gases with lower ionization potentials. For example when the prototype thruster was operated on argon, the current-voltage characteristic is a much shallower upward sloping curve.

4.1.2 Lessons Learned from Prototype Hall Thruster

The prototype Hall thruster exhibits several operational difficulties. The most important shortcoming of the design was the relatively weak radial magnetic field. As shown in Figure 4.3, the magnetic field is severely limited by magnetic circuit saturation. Above currents of approximately 500 mA, the magnetic field is saturated and no longer increases linearly with the current. This does not allow the radial magnetic field to exceed a value of approximately 95 G. It should also be noted that the wire used in the magnetic circuit has a maximum rated current of 2 A. The relatively small central magnetic core is responsible for

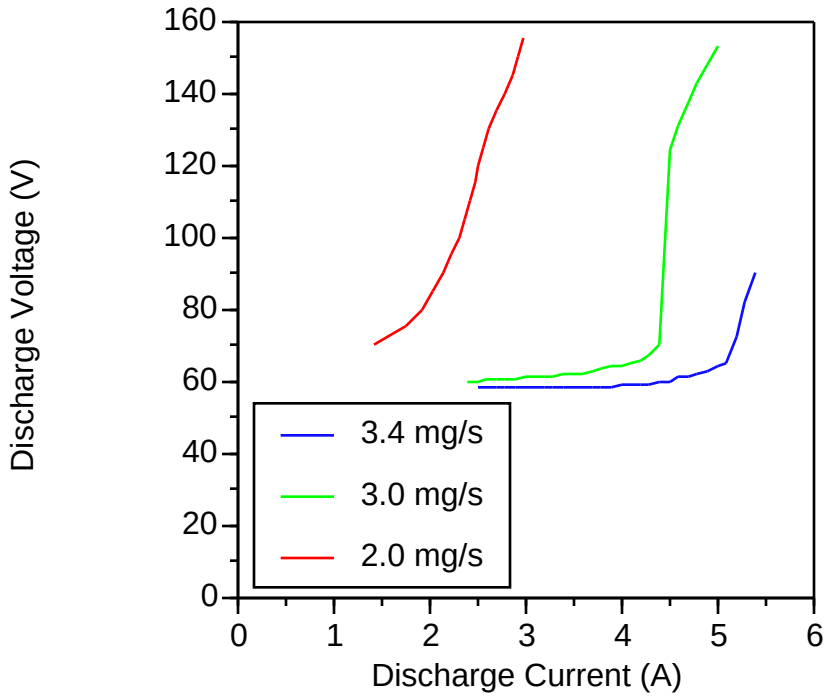

Figure 4.2. Current-voltage characteristic of prototype Hall thruster at a number of anode flow rates (Xe) and at a magnetic circuit current of 2.0 A.

the weak radial magnetic field. Due to the design of the insulator, it proved impossible to modify the central core design without investing in a new insulator.

The weak field was not due to the choice of materials. An effort was made to replace the original mild steel cores with commercially pure iron; however, the magnetic field within the thruster did not appreciably improve. Iron has the second highest saturation flux density of common engineering materials and a relatively large permeability (Lidde). Therefore, the low field strength within the prototype Hall thruster may only be attributed to the design of the magnetic circuit. The only engineering material with a higher saturation flux density than commercially pure iron (21,000 G) would be an alloy of approximately 50% iron and 50% cobalt (24,000 G). The high cost of this material and the added complexity in properly machining this material prohibited this option.

As shown in Figures 4.4 and 4.5, the magnetic field profile varies little along the depth of the insulator. More efficient thrusters have their peak magnetic fields near the thruster exit (Morozov et al.). This thruster channel has a region in which $dB/dZ > 0$ ($Z < 5$ mm) and $dB/dZ > 0$ ($Z > -5$ mm). As discussed by Morozov et al., the axial variation

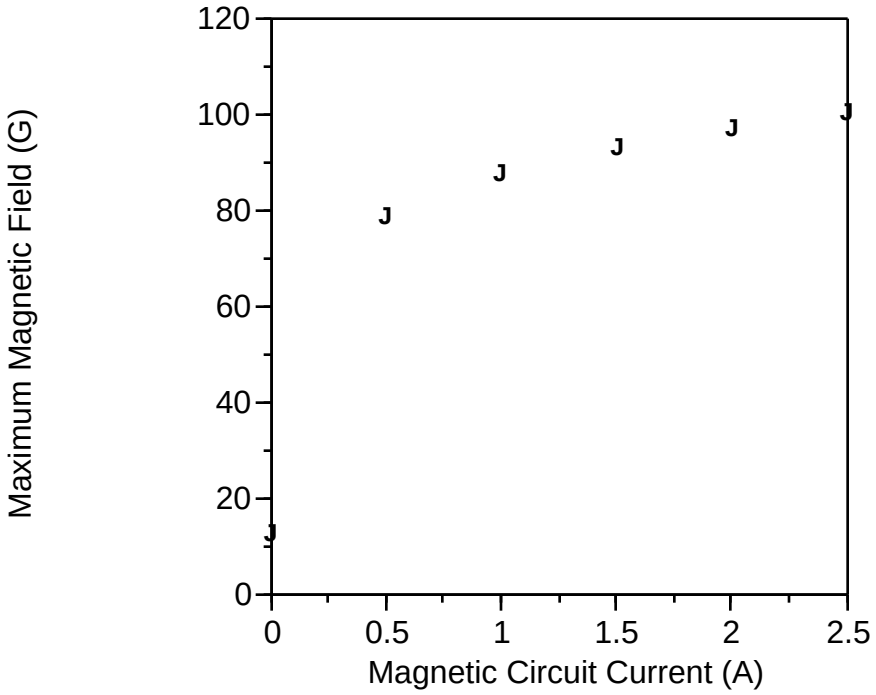

Figure 4.3. Saturation plot of prototype Hall thruster magnetic field. Values shown are maximum values of the radial magnetic field in the center of the acceleration channel.

in the magnetic field has a significant affect on the transitory response of these discharges. His studies reveal that for discharges in which $dB_r/dZ \geq 0$ over the entire channel, the ratio of the average ion current (I_i) to total average discharge current (I_d), $\xi = I_i/I_d$ can exceed 60%. In contrast when $dB/dZ < 0$, $\xi \leq 0.4$, the enhanced electron current conductivity is attributed to the instabilities associated with the low-frequency traveling azimuthal drift waves predominant in the region of the discharge where $dB/dZ<0$. These disturbances give rise to equi-potential surfaces that connect the exit plane to the anode along which electrons can migrate. The magnetic field distribution present in this discharge supports the growth of such waves, and gives rise to values of $\xi \sim 0.4$ at the cathode plane under nominal operating conditions. This relatively low value indicates that the thruster is operating at below optimum performance which is attributed to the shape and strength of the radial magnetic field.

A less subtle design flaw was the catastrophic failure of the alumina insulator. The typical event would occur at discharge voltages above 150 V. Portions of the outer, or inner, wall of the insulator would fail. On occasion, the entire outer ring would separate

from the main body of the insulator. The common failure points are specified in Figure 4.1. Initially, electron heating of the acceleration channel walls was blamed. Later, two facts were determined from the manufacturer, Astomet, Inc. The first batch of 3 insulators was scrapped since stresses induced during the firing of the alumina caused cracks to form at the base of the inner and outer points specified in Figure 4.1. In the second batch of 3 insulators, the shrinkage due to the firing process was larger than expected. In order to reach specified dimensions, portions of the acceleration channel were diamond ground by the manufacturer. These incidents suggest that small cracks and stresses were introduced by the diamond grinding, or were present from the initial curing process. The presence of these flaws then led to the catastrophic failure of the insulator when it was heated beyond a critical threshold. Temporary repairs of the insulator were made by using an alumina cement (Cotronics, Inc. HP-408). After a heat treatment of several hours, the insulator is suitable for use.

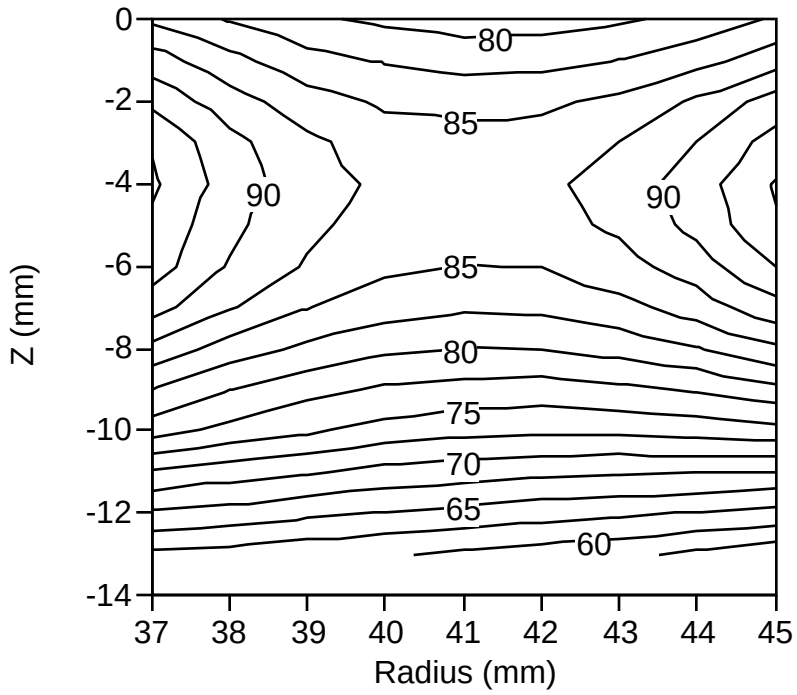

Figure 4.4. Radial component of magnetic field (G) in the prototype Hall thruster.

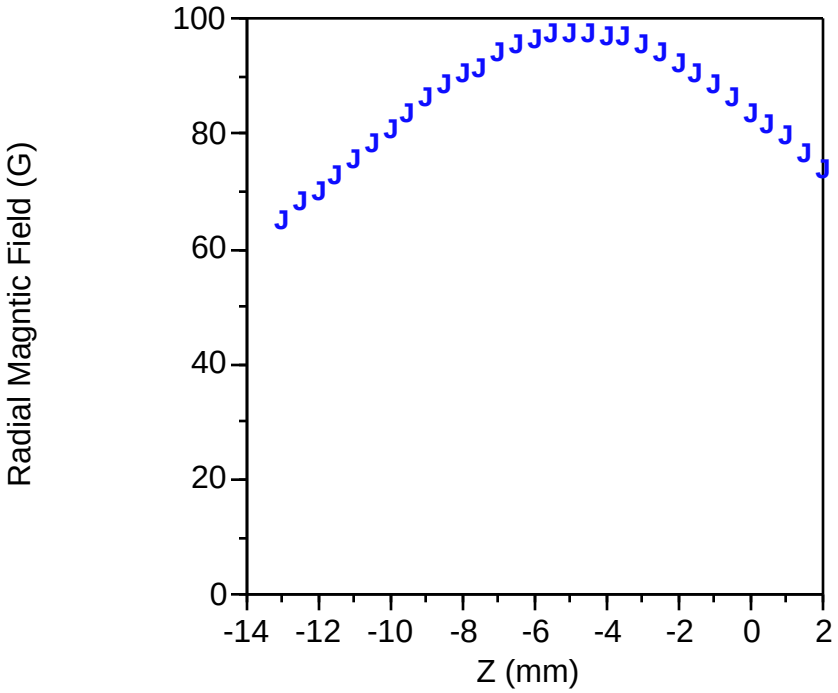

Figure 4.5. Centerline profile of radial magnetic field in the prototype Hall thruster.

4.2 Modified Hall Thruster

4.2.1 Design of Modified Hall Thruster

A second laboratory Hall thruster was constructed to address the design issues raised by the prototype. The primary modifications consist of larger magnetic cores and a redesigned insulator. These modifications resulted in a Hall thruster capable of producing magnetic fields above 350 G and able to operate at discharge voltages above 250 V.

The modified thruster retained the general dimensions of the prototype as well as several parts. A schematic of the modified thruster design is shown in Figure 4.6. It has outer cores of 95mm long with a 25 mm diameters fabricated from commercially pure iron wound with 6 layers of 22 gauge kapton insulated copper magnet wire. The inner core has a 25 mm diameter and is 89 mm long with 12 layers of magnet wire.

In order to tailor the shape of the magnetic field, the electrical insulator was lengthened to a depth of 78 mm (distance from exit plane to the anode). The insulator walls

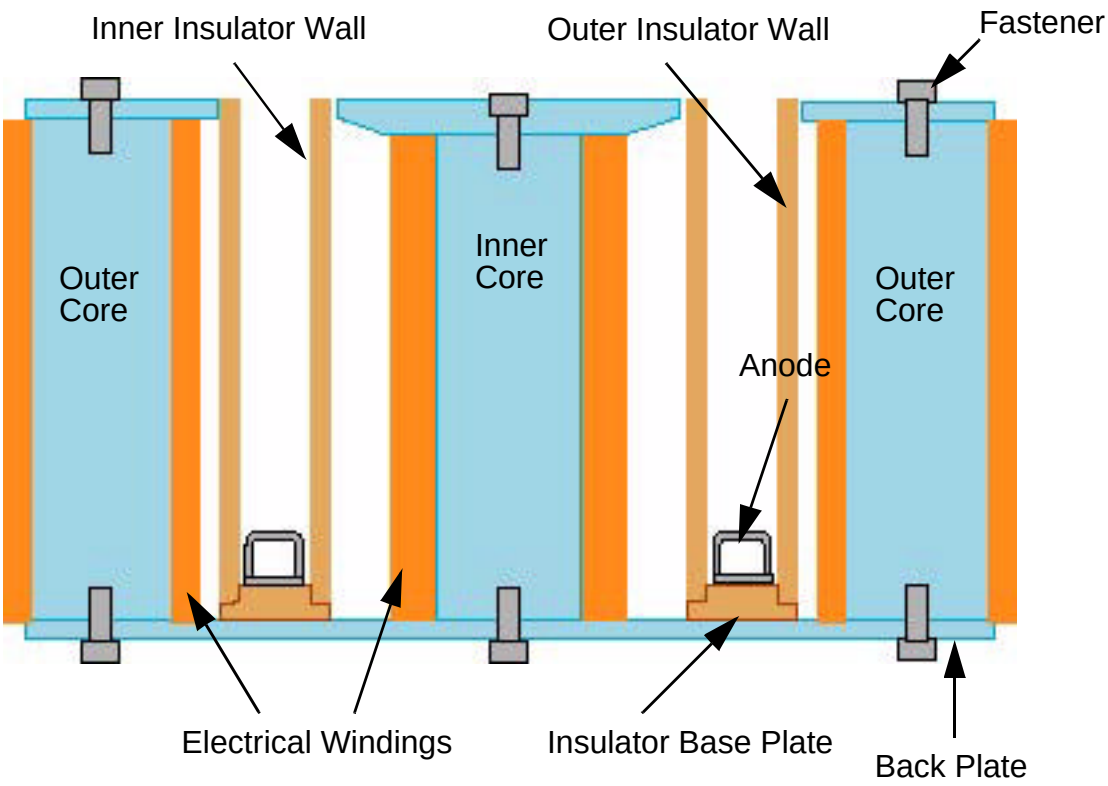

Figure 4.6. Cross-section of modified Hall thruster with main portions labeled.

are constructed from 2 sections of cast 99.9% alumina tubing cut to the required length. The alumina tube used for the outer wall of the insulator is 89 mm in length with an outer diameter of 102 mm and an inner diameter of 94 mm. The inner piece is 89 mm in length with an outer diameter of 70 mm and an inner diameter of 62 mm. These two pieces are cemented to a machinable alumina base plate attached to the back plate of the thruster with non-conducting alumina fasteners (not shown). The anode of the modified thruster is the same as used in the prototype. The cathode is identical to that of the prototype and is mounted similarly. The geometry of the modified thruster is essentially identical to the prototype except for the depth of the acceleration channel. The width of the acceleration channel remains at 12 mm and all other dimensions are identical to the prototype thruster.

A typical profile of the magnetic field in the center of acceleration channel is shown in Figure 4.7. The profile is much improved over the nearly uniform field produced by the prototype. Specifically, there is a positive gradient through the majority of the acceleration channel and the magnetic field magnitude is substantially lower near the anode.

Unlike in the prototype thruster, the radial magnetic field peaks near the exit plane. In addition, the magnetic circuit does not show evidence of saturation over a wide range of operation. Figure 4.8 shows the exit plane radial magnetic field measured at the inside insulator wall, the channel center, and at the outside insulator wall. These data show no evidence of saturation in the range explored. The divergence of the three traces is consistent with the divergence of the magnetic field lines in the radial geometry of the Hall thruster. Figure 4.9 is a vector plot of the axial and radial magnetic fields as measured. Here, the magnetic field within the acceleration channel is shown to be predominantly radial.

Figure 4.10 shows a typical current-voltage characteristic of the modified Hall thruster operating at a total mass flow rate of 2.3 mg/s. Of this flow, 87% flowed through the anode and 13% flowed through the cathode. This cathode/anode propellant fraction corresponds closely to that of other Hall thrusters. A cathode flow fraction on the order of 10% of the total flow rate is generally required to ensure neutralization of the plume.

4.2.2 Modified Hall Thruster Operational Difficulties

An important modification of the magnetic circuit was required after initial testing of the modified Hall thruster. After a series of runs totalling approximately 10 hours of operation, the thruster discharge current-voltage characteristic was no longer consistent with initial measurements. The thruster was removed from the vacuum chamber and examined. The magnetic field at a given magnetic circuit currents no longer matched values measured prior to testing. A residue on the insulator, believed to be iron sputtered from the front plate, was removed by sandblasting the inner and outer walls of the insulator. After several such events, the front plate of the insulator was covered with boron nitride aerosol spray manufactured by Carborundum, Inc. This eliminated the variation in magnetic field strength due to Hall thruster operation.

The only difficulty of this solution was that the aerosol boron nitride uses a nitrocellulose binder. After any period extended operation, the surface layer of the coating darkens and begins to flake off. Between operations, this layer may be gently brushed off, or blown off using compressed air. After several such interim cleanings, the Hall thruster has to be taken from the vacuum chamber and the remaining boron nitride coating removed prior another application. The worst of this darkening always occurs on the surface of the central

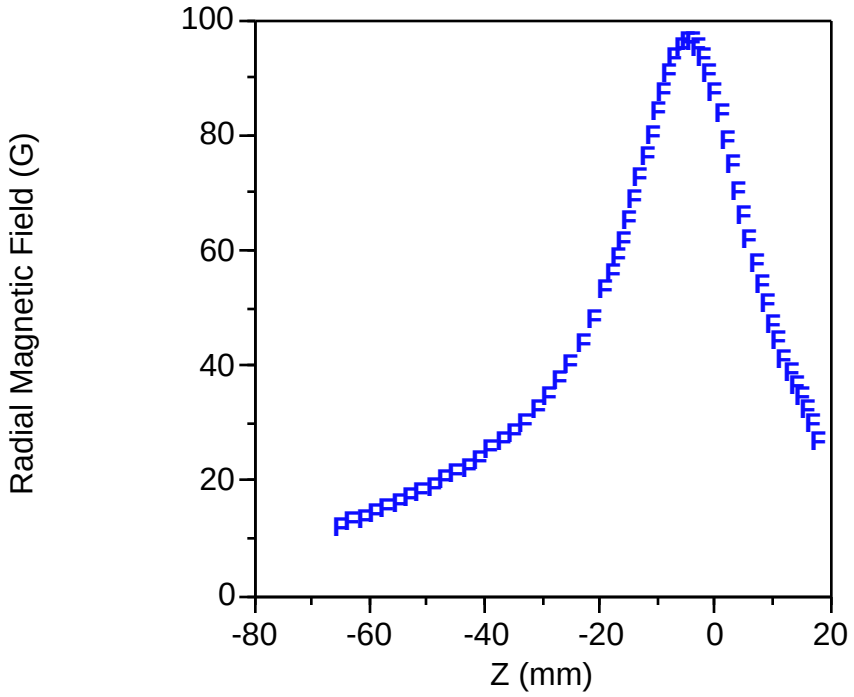

Figure 4.7. Centerline profile of the radial magnetic field of the modified Hall thruster. The magnetic circuit current for this case is 125 mA.

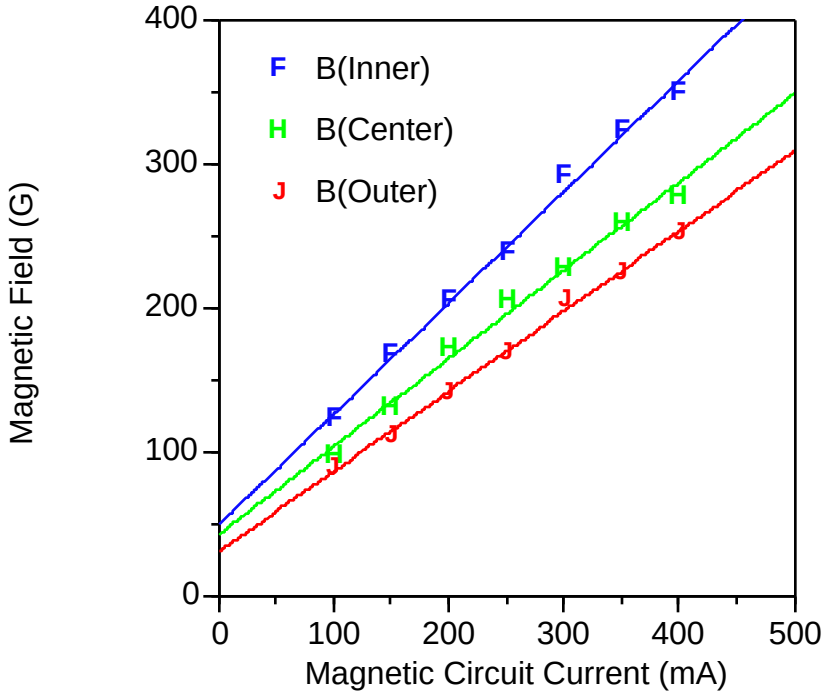

Figure 4.8. Modified Hall thruster radial magnetic field at three radial locations. The linear behavior indicates little, or no, saturation of the magnetic circuit.

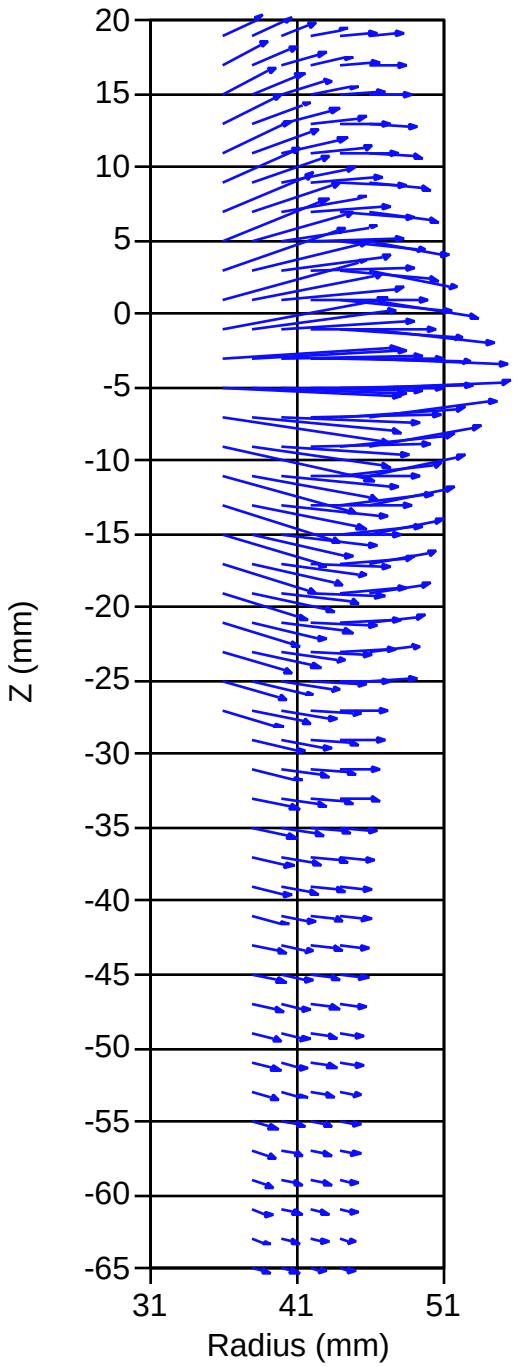

Figure 4.9. Vector plot of magnetic field within the acceleration channel of the modified Hall thruster. The vectors are proportional to the radial and axial components of the magnetic field. The magnetic circuit current for this case is 125 mA.

core. A likely mechanism for this process is that low energy electrons emitted from the cathode follow the magnetic field lines in the plume to the central core. This supposition is supported by the free molecular flow conditions prevailing in the plume which inhibit electron transport across magnetic field lines.

Above discharge voltages of approximately 225 V, it becomes difficult to operate the modified Hall thruster. The discharge current slowly increases over periods of an hour for values near 250 V and over several minutes at discharge voltages in the neighborhood of 300 V. Above a critical value of the discharge current, the discharge will extinguish. Increasing the magnetic field extends the length of operation at higher discharge voltages. Operation at higher background pressures worsens the behavior. At moderate discharge voltages (~150 V), increasing the magnetic field strength lowers the discharge current. It is believed that the relatively high background pressures in the vacuum chamber (~10^{-4} Torr) contribute to plasma instabilities in the thruster which ultimately extinguish the discharge (Randolph et al. 1993, Crofton). This is supported by the observed worsening of the behavior at higher chamber pressures.

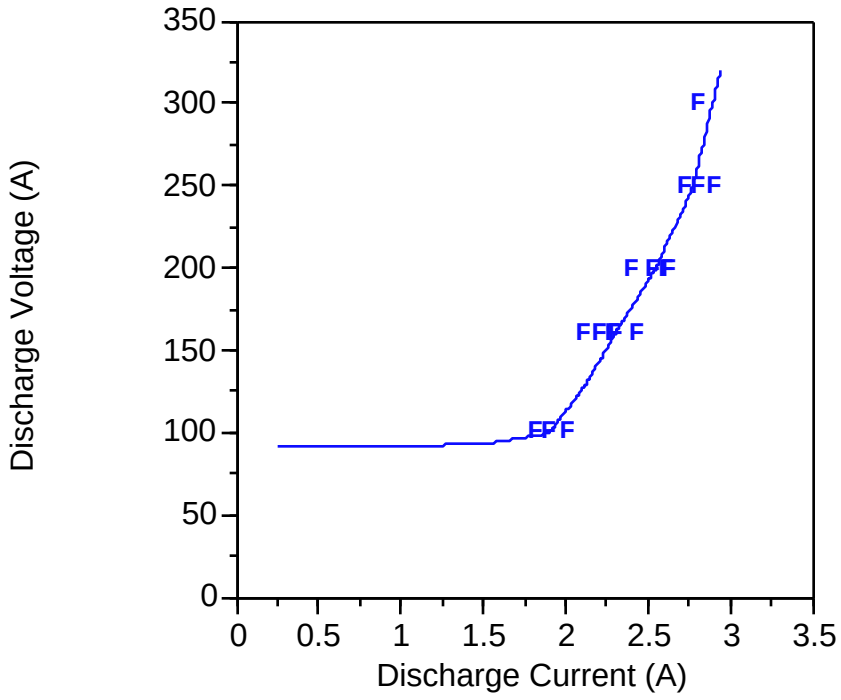

Figure 4.10. Current-voltage characteristic of the modified Hall thruster and a magnetic circuit current of 125 mA and a xenon propellant flow of 2.3 mg/s.

When the thruster is first placed in the vacuum chamber, or after an insulator has been cleaned, the Hall thruster starts first as a glow discharge between the anode and hollow cathode with the application of approximately 100 V. After the Hall thruster has been run at discharge voltages in excess of 200V for periods greater than several hours, start ups become more difficult. Others have also experienced similar behavior from their Hall thrusters (Ashkenazy et al.). These incidents have been attributed to insulating layers deposited on the anode which inhibit the initial break down of the main discharge. However in this case, it is believed that oil from the diffusion pumps, or sputtered materials from the vacuum chamber, deposit on the insulator and thereby change the thruster start behavior. Four methods of dealing with this problem were discovered during testing. The simplest is to apply higher voltages. The initial breakdown will occur if a sufficiently large voltage is applied; however, the power supply available was limited to 310 V and therefore this option is usually not available. The most commonly used method is to maximize the anode voltage and pulse the xenon propellant through the anode. Generally, a single pulse will result in a glow discharge breakdown. The difficulty with this method is that it actually worsens the deposition of pump oil on the thruster. The sudden increase in pressure within the chamber causes the oil diffusion pumps to burp and expel a small amount of pump oil that will eventually coat all surfaces within the vacuum chamber. Another method is to clean the insulator with glow discharge. This discharge only requires a low current and several power supplies capable of providing 600 V, or more, are available for this purpose. The most drastic method is to remove the thruster from the chamber, remove the insulator from the thruster, and clean the insulator. Initially, several solvents including methanol, ethanol, and acetone were used, but these did not alleviate the starting problem. Eventually, the best solution was to remove the insulator and sandblast the contaminated surfaces. After thruster reassembly, this always produces a clean start. Unfortunately, the insulator would soon be coated again with oil and sputtered material if it was run for any period of time, particularly at discharge voltages in excess of 200 V.

Figure 4.11 shows the time history of the DC discharge current at a nominal discharge voltage of 200V. Two cases are shown. The first is of a cold start where the thruster has not been operated since the initial evacuation of the vacuum chamber. The second shows the time history of the discharge current for a warm start where the thruster was operated for

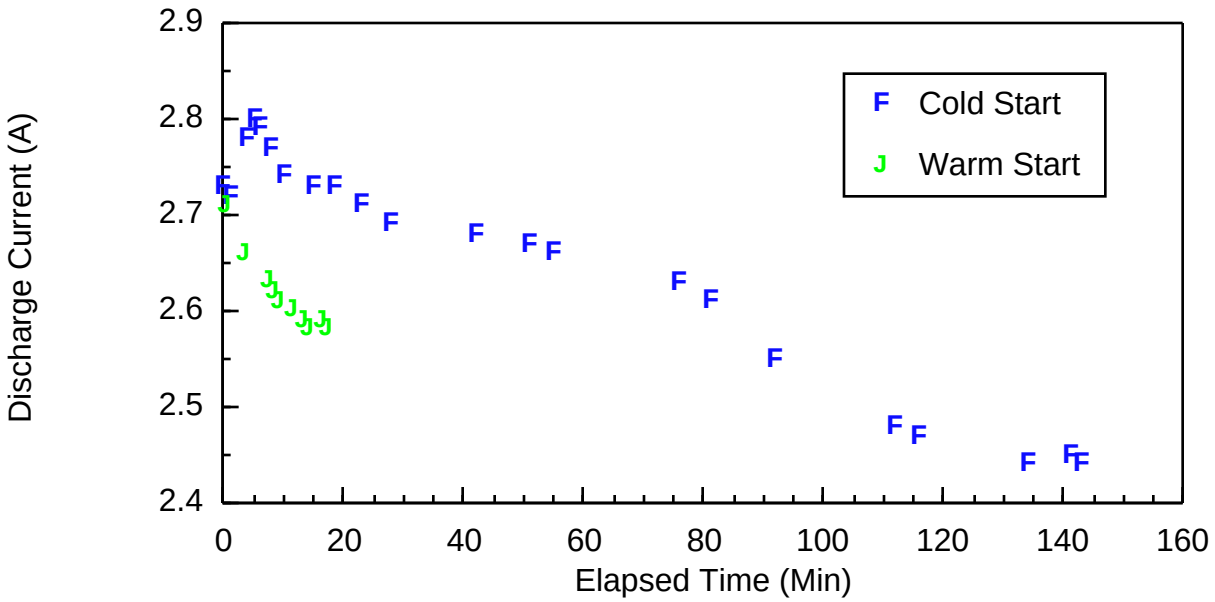

Figure 4.11. Discharge current time variation for a set discharge voltage of 200V, magnetic circuit current of 125 mA, and a xenon propellant flow rate of 2.3 mg/s.

150 minutes prior to being shut down and restarted after approximately 20 minutes. The cold start curve exhibits a sharp increase soon after starting which is followed by a sharp decrease. The discharge current then continues to fall for the remainder of the measurements. In the case of a warm start, the initial current rise does not occur and the slow decrease in discharge current is similar to the cold start case after the initial rise except that the slope is more negative. Similar behavior has been observed by others and has been attributed to the plasma cleaning the insulator interior (Bugrova et al.). The subsequent fall in discharge current is believed to be due to further cleaning of the insulator by the discharge itself. Similar behavior is present for all operating conditions below 200 V. For discharge voltages above 200 V, the behavior is reversed with the discharge current slowly rising. It is possible that the thruster insulator is acquiring more deposits than the discharge can remove. This is consistent with the starting difficulties discussed earlier. The higher energy ions are sputtering more materials from the vacuum chamber walls which may redeposit on the thruster. In addition, the thruster plume exhausts into a diffusion pump. It is likely that oil from this pump is backstreaming into the test section especially when the thruster is operating at higher discharge powers. This is supported by increased oil deposits on interior surfaces after tests at discharge voltages above 200 V.

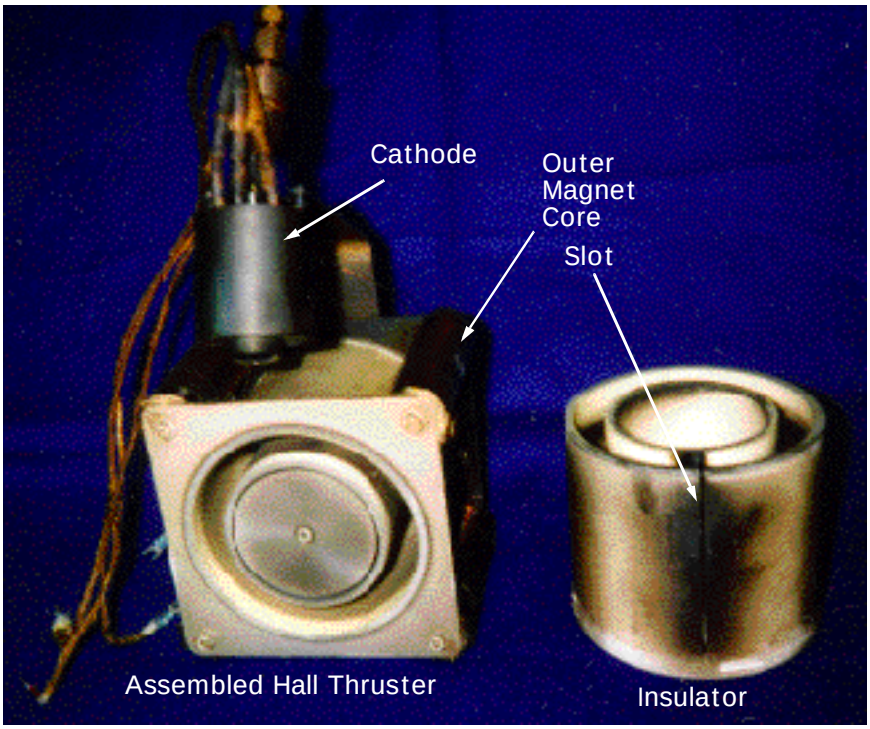

Figure 4.12. Photograph of Hall thruster and of slotted insulator.

4.2.3 Optical Access of Interior

A second insulator was constructed for the modified Hall thruster. It is identical to the insulator described previously; however, a slot approximately 1 mm wide along the length of the outer wall of cast alumina was diamond sawn prior to assembly. The slot is used to provide optical access to the interior of the Hall thruster. Operation of the Hall thruster with the slotted insulator does not differ significantly from the operation with the unslotted insulator. The current voltage characteristic is unchanged. Ionic xenon laser velocimetry and plasma potential measurements in the plume also show no deviation in Hall thruster operation. A photograph of the modified Hall thruster and slotted insulator is shown in Figure 4.11. In the figure, the insulator is shown after extensive testing has been completed. The dark deposits on the insulator are the result of the partial carbonization of the phenolic thruster mount.

The optical access provided by the slot is blocked near the exit plane by the front plate of the magnetic circuit. The front plate is not cut since this would modify the local

magnetic field. The magnetic field is one of the most important parameters determining the behavior of the plasma in the Hall thruster discharge and any change in the field would immediately change the plasma characteristics. The less than 4 mm field of view blocked by magnetic circuit is less important than preserving the uniformity of the magnetic field within the Hall thruster.

4.3 Experimental Facility

4.3.1 Vacuum System

The Stanford high vacuum test facility is constructed of non-magnetic stainless steel. The main section is a tank approximately 1 m in diameter and 1.5 m in length. Two 50 cm diameter elbow sections are attached on either end of the main section on large aluminum flanges. Each elbow supports an oil diffusion pump. The entire chamber is mounted on

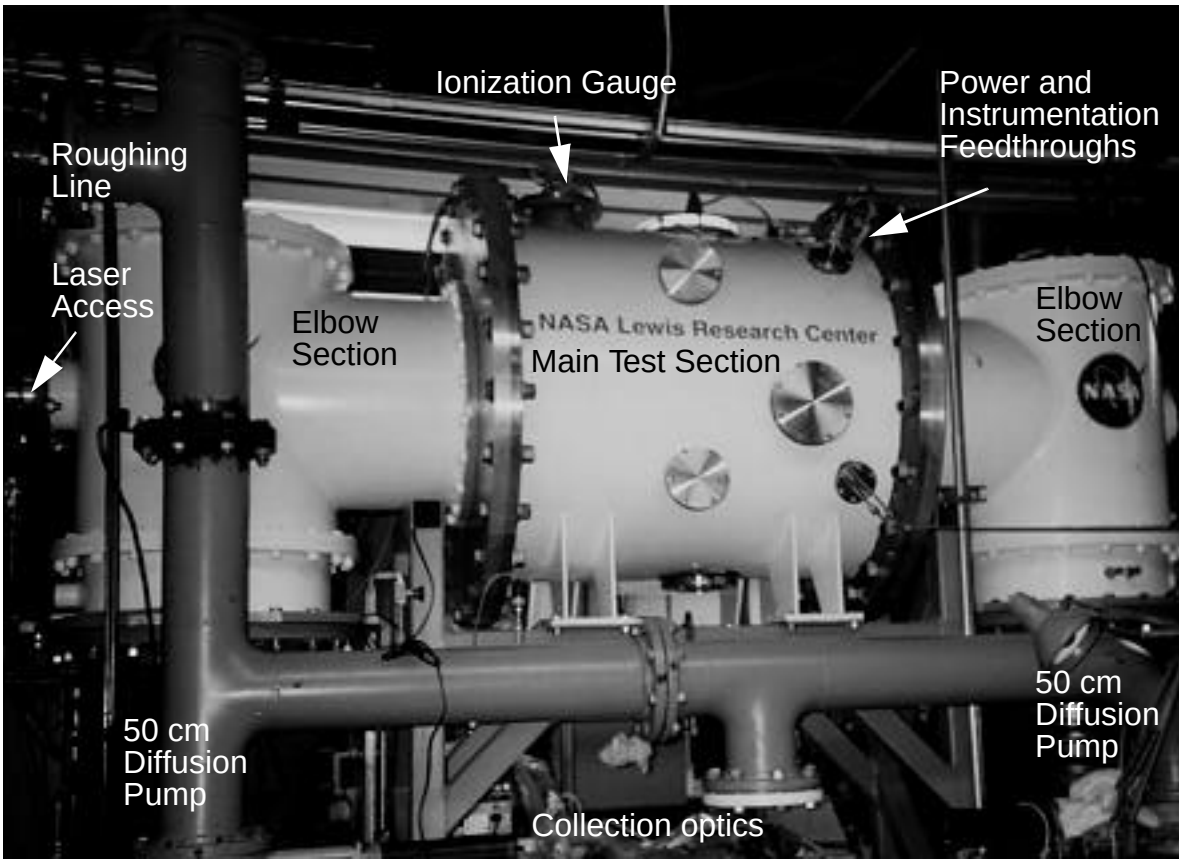

Figure 4.13. Photograph of the Stanford high vacuum facility. Note the two 50 cm diffusion pumps at either end of the vacuum chamber.

a steel frame which provides the diffusion pumps a ground clearance of approximately 40 cm. The chamber was provided to Stanford University by NASA Lewis Research Center in 1994. A photograph of the facility is shown in Figure 4.13.

The facility is pumped by two Consolidated Vacuum Corporation 50 cm diffusion pumps. Each pump has a rated air pumping speed of 18,000 l/s. Accounting for conductance losses due to the elbow geometry, the actual pumping speed of the facility is estimated to be 16,500 l/s for air (Redhead et al.). The measured system pumping speed is 15,000 l/s for argon. The diffusion pump oil used is a silicone terminated hydrocarbon (Dow Corning 705) which is highly inert and has an atomic mass of approximately 500 amu. The two diffusion pumps are backed by a Stokes 425 l/s mechanical pump through a single foreline ballasted with a flow of dry nitrogen to maintain the roughing line pressure at approximately 80 mTorr. Pneumatically actuated gate valves allow for either, or both, of the pumps to be used during a test.

The pressure within the vacuum chamber is measured with a single Bayard-Alpert hot filament ionization gauge manufactured by Duniway Stockroom, Inc. calibrated for nitrogen. For other gases, a correction factor dependent on the appropriate ionization cross-section is available. The multiplicative correction factor for xenon is approximately 0.3. However even when nitrogen is the primary residual gas, ionization gauges are seldom accurate to better than ±50%, or repeatable to ±25%. Measurements of background pressure will be given for the nitrogen calibration to avoid the complexity of dealing with partial pressures of residual gases in the vacuum chamber and to conform with the majority of the literature.

The base pressure of the vacuum facility is approximately 10^{-6} Torr as measured by the ionization gauge uncorrected for gas species. Chamber pressures during thruster testing at xenon flow rates of 2 to 3 mg/s (20-30 sccm) are in the region of 10^{-4} Torr. This indicates that the facility has a xenon pumping speed of at least 3,000 l/s, and as high as 9,000 l/s if the pressure correction for xenon is made. At these relatively high pressures, there is some back flow of diffusion pump oil into the vacuum chamber.

Propellant flow to the anode and cathode is controlled by two Unit Instruments 1200 series mass flow controllers. The anode mass flow controller has a controllable flow rate of 2.5 to 50 sccm (0.3 - 5 mg/s) of xenon. The cathode flow is controlled by a mass flow

controller with a range of 0.3 to 5 sccm (30 - 500 µg/s) of xenon. Both mass flow controllers are factory calibrated for xenon flow into zero back pressure. The grade of xenon propellant in this study is research grade (99.99%) xenon purchased from Prax Air, Inc. The major contaminant consists of 80 to 90 ppm of krypton. Water and oxygen content is less than 5 ppm.

4.3.2 Thruster Electrical Circuit.

A schematic of the electrical power circuit for the Hall thruster is shown in Figure 4.14. The main discharge is powered by a Sorensen DCR300-6 laboratory power supply capable of providing 310 V and 6 A to the anode. A 4 Ω ballast resistor (Dale 250 W, 1%) is placed in series with the anode and power supply to mitigate the initial start-up transient. The cathode heater element is powered by an unregulated DC power supply which provides 8.5 A to initially heat the cathode and 4.0 A after establishment of the anode discharge. The cathode keeper uses a Sorensen SCR600-1.7 power supply which provides 250 V to initiate cathode ignition and approximately 10 V and 250 mA during thruster operation. The magnetic circuit current is provided by a regulated DC power supply. All electrical grounds shown on Figure 4.14 are made to a common point on the support frame of the vacuum chamber.

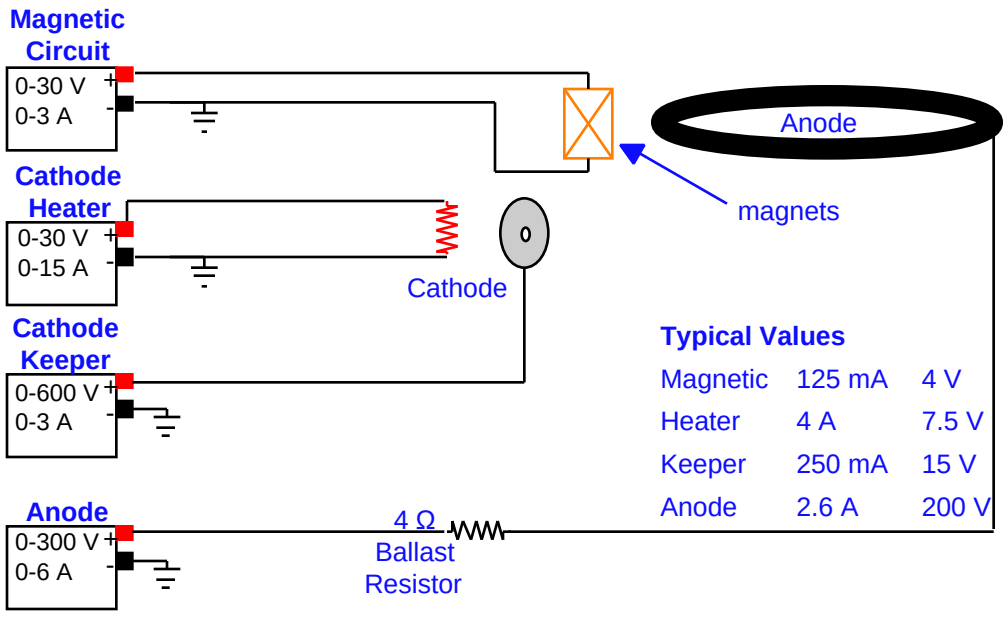

Figure 4.14. Electrical circuit for the Hall thruster with all major components labeled. Values quoted are for the modified Hall thruster.

The current of the anode discharge and the cathode heater were monitored using calibrated 10 mV/A current shunts. During Hall thruster operation, the voltage drop across the shunts are monitored with handheld digital voltmeters (Goldstar DMM50). The main discharge voltage is also monitored with a digital voltmeter. It should be noted that the discharge voltage is monitored upstream of the ballast resistor in Figure 4.14 relative to ground. Therefore, the values quoted for the discharge voltage represent the actual anode potential.

4.3.3 Typical Thruster Operational Procedure Procedures

The typical start up for the modified Hall thruster consists of the following procedure.

- The cathode flow rate set to 3 sccm (300 μg/s).
- Cathode heater current set to 8.5 A.
- Keeper voltage set to 250 V and current limited to 250 mA.
- Wait approximately 3 to 5 minutes for cathode discharge to ignite.
- Set anode xenon flow rate to 20 sccm (2 mg/s).
- Current limit main discharge power supply.
- Turn on main discharge power supply and slowly raise voltage until main discharge ignites.
- If main discharge does not ignite, raise anode potential to maximum and pulse mass flow.
- With main discharge ignited, turn on magnet power supply and raise current to specified level.
- Remove current limit on main discharge and transition to voltage control mode.
- Lower cathode heater current to 4.0 A.

Under most operating conditions the thruster behaves well and requires little, or no, monitoring during operation. The procedure for shutdown of the thruster is given below.

- Turn off main discharge power supply.
- Turn off anode propellant flow.

- Turn off magnetic current power supply.
- Turn off cathode heater current.
- Turn off cathode keeper power supply.
- Reduce cathode xenon flow to 1 sccm (100 µg/s) and allow cathode to cool for 30 minutes.
- Stop cathode propellant flow.

4.4 Thrust Stand

4.4.1 Description of System

The thrust stand used for these studies was based on the inverted pendulum design of Haig at NASA Lewis Research Center (Haig and Curran). The principles of an inverted pendulum thrust stand are described in Chapter 3. Figure 4.15 shows a photograph of the thrust stand used in this study. The stand was built by the Jet Propulsion Laboratory

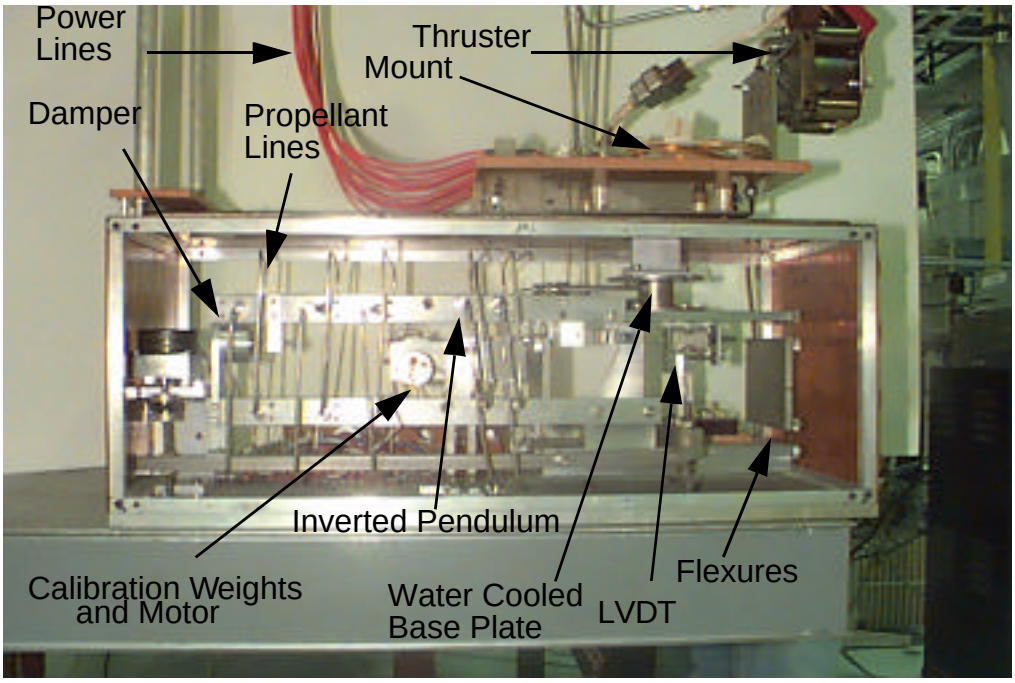

Figure 4.15. Photograph of inverted pendulum thrust stand at the electric propulsion group of the Air Force Research Laboratory. Note the Russian SPT-70 Hall thruster in the upper right.

for the electric propulsion group of the Air Force Research Laboratory and loaned to Stanford for approximately 6 months.

For thrust measurements, the thruster is placed on a mount atop the inverted pendulum. The mount is actively cooled with a water cooled base plate and electrically isolated by ceramic spacers. By water cooling the portion of the stand which supports the thruster as well as the top and front surfaces exposed to the thruster plume, thermal drift is minimized. As shown in Figure 4.15 the power lines may be hung from above and connected to the thruster mount provided the lines are sufficiently flexible. Alternatively, they can be attached between the stationary portion and the pendulum portions of the thrust stand as are the propellant lines. In either case, the power lines affect the spring constant of the thrust stand. Active damping and excitation of the thruster is performed by a damper with closed loop feedback. The damping is required to control vibrations so that a useful measurements may be taken. The excitation of the thrust stand is required due to the combined sticking and friction of the effective spring that supports the inverted pendulum. It is therefore necessary to introduce an oscillation into the pendulum and then damp it out in order to produce a valid measurement. Thrust is determined from the pendulum displacement measured by a Lucas Schaevitz linear voltage differential transducer (LVDT). The signal from the LVDT is read on a Lucas Schaevitz DTR-451 digital transducer readout.

4.4.2 Measurement Procedure

Calibration of the thrust stand is provided by four 5.0 g weights. The weights are mounted on monofilament line and are raised and lowered by a small DC motor with a rotary encoder. A calibration curve is show in Figure 4.16. The linearity of the thrust stand is excellent, better than 1%. However, the zero drift of the device is appreciable. The stand requires frequent recalibration in order to produce meaningful results. The resolution of the LVDT and the spring constant of the system as well as a number of environmental pertubations limit the resolution of the thrust stand to approximately ± 0.5 mN. Therefore, each thrust measurement requires the thruster be run for a period of 15-20 minutes to stabilize the thruster and to allow the thrust stand to reach thermal equilibrium. At this time, 3 to 5 measurements of the thrust stand displacement are made, interspersed with induced oscillations

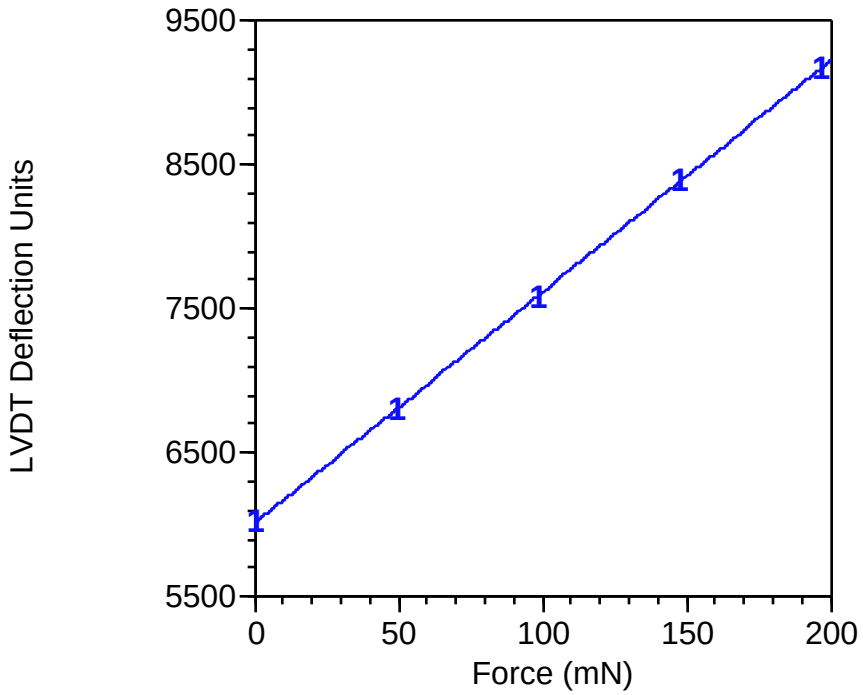

Figure 4.16. Calibration curve of the inverted pendulum thrust stand through its full scale 0 to 200 mN.

to reduce stiction. All power and propellant flow to the thruster are then stopped and a thrust stand calibration follows.

4.4.3 Difficulties in Thrust Measurements

With each change of the thruster operating condition, the zero point drifted significantly corresponding to as much as several mN of uncertainty. The solution to this problem was to ensure that the thruster and thrust stand thermalized. Measurements were then taken as quickly as possible. Then the thruster was shut down and a calibration performed.

Frequent recalibration also helped to solve a difficulty with the water cooling. Pressure and temperature changes in the building water supply can be recognized by the drift on the LVDT readout. Sudden changes in the building water pressure during daylight hours produce distinct oscillations in the thrust stand. These difficulties are mitigated by running predominately after nightfall when the temperature and pressure of the cooling water are less variable.

No solution was found for mechanical vibrations in the laboratory. The Stokes roughing pump produced high energy, low frequency vibrations that are impossible for the damping circuit on the thrust stand to completely eliminate. Although the roughing line is vibrationally isolated from the roughing pump, the pump is on the same foundation as the laboratory. Therefore, the vibrations are directly coupled to the vacuum facility. The 7,000 lb. mechanical pump could not be moved for this experiment. The vibrations represent a serious limitation to thrust measurements and unless eliminated will continue to do so for future measurements.

4.5 Laser Induced Fluorescence Apparatus

4.5.1 Optical System

The apparatus used for the laser induced fluorescence velocimetry consists of a tunable Coherent 899-21 single frequency titanium sapphire laser system shown in Figure 4.17. The titanium sapphire laser is actively stabilized to provide line widths on the order of 1 MHz with near zero frequency drift. Scan widths of up to 20 GHz can be realized at center wavelengths between 680 to 1060 nm. The tunable laser is pumped by Coherent solid state Verdi pump laser. The pump laser provides 5 W of single mode pump power at 532 nm. The laser wavelength is monitored by a Burliegh Instruments WA-1000 scanning Michealson interferometer wavemeter with a resolution of 0.01 cm^{-1}. The probe beam is directed into

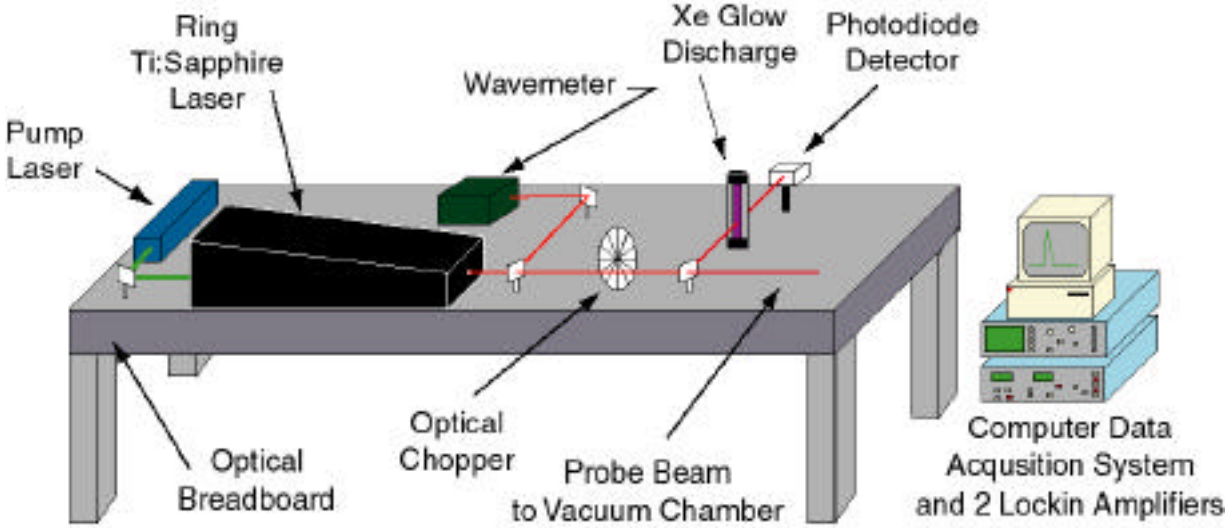

Figure 4.17. Laser setup for LIF velocimetry experiments.

the Hall thruster plume by a series of mirrors. The slightly divergent beam (1.7 milliradians full angle) is focused to a submillimeter beam waist in the discharge plasma. For the axial velocity measurements shown in Figure 4.18, the probe beam is focused by a 50 mm diameter, 1.5 m focal length lens. While for the radial velocity measurements, the probe beam is focused by a by a 50 mm diameter, 500 mm focal length lens as shown in Figure 4.19.

The collection optic is a 75 mm diameter, 60 cm focal length fused silica collimating lens. The collected fluorescence is then focused on to the entrance slit of a 0.5 m Ebert-Fastie monochrometer with a 50 mm diameter, 30 cm focal length lens. An optical field stop is placed between the two lenses to match the F/# of the optical train with that of the monochrometer.

The monochrometer acts as a narrow band optical filter so that only light from the transition of interest is collected. With entrance and exit slits full open (425 μm), the 600 groove/mm plane grating blazed for 600 nm within the monochrometer allows the Hamamatsu R928 photomultiplier tube (PMT) to sample a wavelength interval of approximately 1 nm. The orientation of the monochrometer allows the height of the slits to define the length of the probe beam along which the fluorescence is collected. Prior to each test and with the PMT housing removed, a HeNe laser is reversed through the entire collection optical train to ensure alignment with the probe beam.

A portion of the pump bean is picked off by a beam splitter, passed through several neutral density filters, and through a xenon glow discharge tube which serves as a stationary reference for LIF velocimetry. The beam is then incident on a photodiode detector where the absorption spectrum of the stationary reference is measured. Due to the relatively short pathlength, <1 cm, and low ionization fraction in the glow discharge, the stationary reference is only useful for neutral velocity measurements.

The LIF signal is recorded using a Stanford Research Systems SRS-850 digital lock-in amplifier. The probe beam is mechanically chopped at 3 kHz by a SRS-540 optical chopper with a 40 blade wheel prior to the beam splitter. The absorption signal from the stationary reference is collected using a SRS-530 lock-in amplifier referenced to the SRS-540. Data from the absorption signal, laser power output, and the wavemeter wavelength output are then stored on the SRS-850 using 3 analog inputs along with the LIF signal. The data are then retrieved by a Macintosh computer for later analysis. Typical tests consist of a 0.4 cm^{-1}

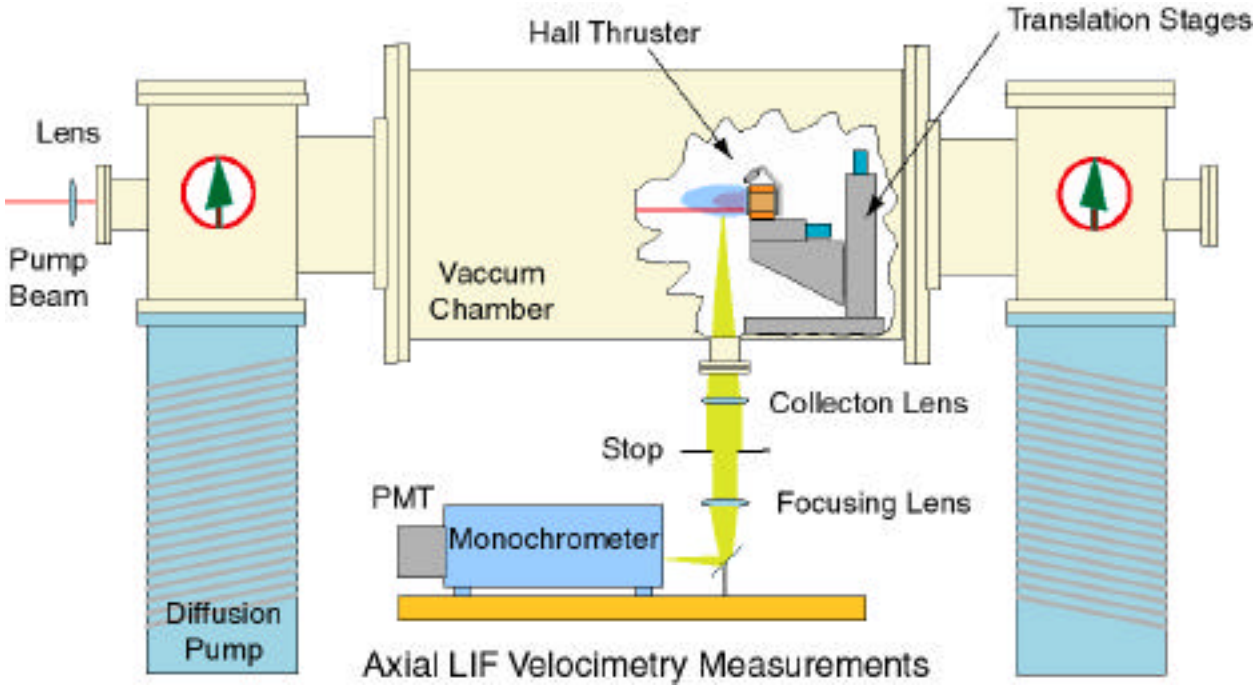

Figure 4.18. Probe and collection optics for axial LIF measurements. Note the thruster mounted on the translation system.

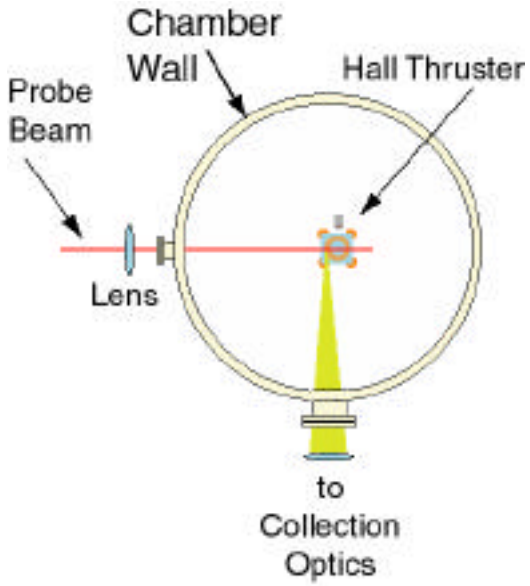

Figure 4.19. Probe and collection optics for radial LIF measurements.

scan of the probe laser frequency over a 4 minute period. The beam is chopped at a frequency of 1.5 kHz. Both lockin amplifiers use 1 s time constants. Data are sampled at 8 Hz, producing four traces of approximately 2,000 points for each velocity measurement.

4.5.2 Thruster Positioner System

As shown in Figure 4.18, the thruster is placed on a two axis translation stage. For axial velocity measurements in the Hall thruster plume, the Hall thruster is mounted on a Velmex Unislide® translation stage with a total travel of approximately 80 mm in the axial direction. In all cases, the thruster is attached to the translation stage and electrically isolated by a phenolic fixture. The vertical stage has an extra long 20 cm slide which provides support for the cantilever load of the horizontal stage and the Hall thruster. The total travel in the vertical direction is approximately 40 cm.

For optical measurements through the slot in the insulator, the horizontal stage is modified by placing the thruster mount on a U shaped 4 mm thick aluminum plate. The plate is supported on one side by the previously described horizontal stage and on the other side by a steel guide rail attached to the thruster mount by a linear ball bearing pillow block. This configuration allows the thruster to translate in the axial direction while providing optical access from below through the insulator slot. The vertical stage described in the first configuration is retained to allow motion along the vertical axis. For radial velocity measurements, the horizontal stage described above is replaced by a longer stage oriented in the radial direction. As in the other configurations, the vertical stage is used as originally described.

Both stages are driven by Superior Electric NEMA 23 encapsulated stepper motors providing approximately 100 oz.-in of torque. The resolution of the motion is controlled by the thread pitch of the translation stage lead screw (1.0 mm/rev) and by the number of steps per revolution (200 step/rev). The stages are controlled by a Keithly Metrobyte two axis stepper motor controller card mounted in a personal computer.

4.6 Emissive Plasma Potential Probe

4.6.1 Probe Construction

Figure 4.20 shows a diagram of the basic emissive plasma potential probe configuration. The probe design is based on Russian measurements performed on early Hall thrusters (Morozov et al. 1972). The probe filament is formed from 150 μm diameter 2% thoriated tungsten wire by winding the wire around a 0.9 mm mandrel for 8 turns for a total length of approximately 1 cm. The filament is suspended between two 0.50 mm diameter tantalum wires with a separation of 5 mm. The tantalum wires are sheathed in a 6 mm diameter multibore mullite tube. The probe filament is heated using a 10:1 step down transformer powered by a Superior Electronics Variac 10 A manual variable transformer which is connected to wall current (120 V, 60 Hz). This transfers AC power to the probe while isolating the probe circuit. The current provided to the probe is monitored by an ammeter to ensure that the filament current is constant during measurements. The floating potential of the

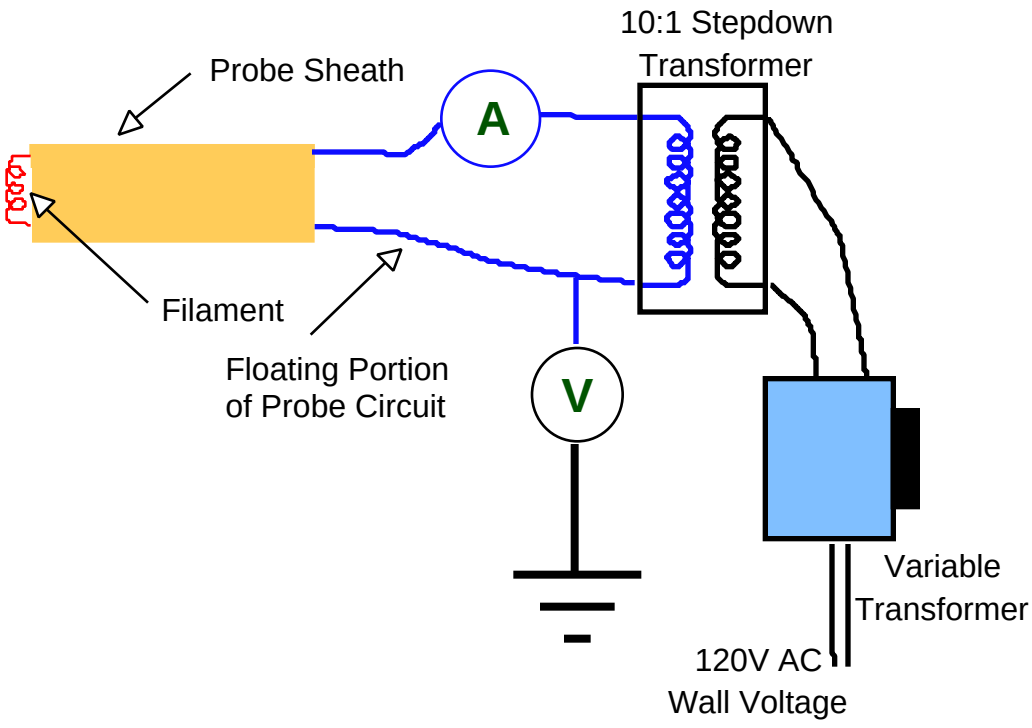

Figure 4.20. Diagram of a emissive plasma potential probe including the probe body, the instrumentation and the heater circuit.

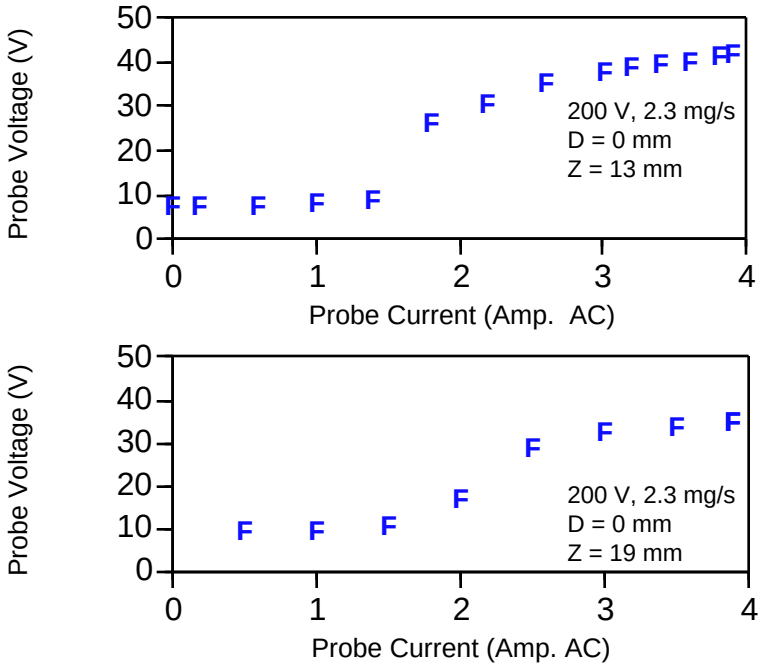

Figure 4.21. Probe potential plotted against probe filament current for two locations.

probe during operation is monitored at the center tap of the transformer by a voltmeter referenced to the vacuum facility ground.

The probe is mounted in front of the thruster on a translation stage with a 15 cm range of motion along the thruster axial direction. The thruster is mounted on the translation system described in section 4.5.2. The horizontal stage is disabled and the thruster is only able to move in the vertical direction. In this way, two axis motion of the probe relative to the thruster is preserved. The translation system is otherwise identical to that used for LIF measurements.

Figure 4.21 shows the approach of the probe potential to the true plasma potential for two plasma conditions. As described in Chapter 3, the emissive probe only asymptotically approaches the true plasma potential from below. The curves in Figure 4.21 were taken prior to testing to show that the plasma potential measured by the probe is consistent with the expected behavior of an emissive probe. Probe filament currents above 4.0 A inevitably leads to shortened filament life and cause failure due to filament evaporation within minutes.

4.6.2 Evolution of the Emissive Probe

The initial plasma potential probe used copper lead wires rather than the tantalum wires described above. Also, the leads were sheathed in two separate 1.25 mm diameter alumina tubes. At low anode discharge voltages, this arrangement worked well. However, when the anode voltage was raised above 150 V, the primary failure mode consisted of melting the copper leads and the thoriated tungsten filament losing electrical contact. In one particularly eventful failure, the copper leads melted and deposited a copper film on the thruster insulator interior walls. This film could only be removed by sand blasting. At this time, the copper leads were replaced with the tantalum leads previously described.

After the copper leads were replaced by tantalum, several difficulties were encountered. First, tantalum is a poor electrical conductor relative to copper, marginally worse than thoriated tungsten (Lidde). At design currents, the tantalum leads heat significantly and it is difficult to maintain a constant current through the filament. The solution to this problem is to only heat the filament for approximately 30 seconds during each measurement. Second, the alumina sheaths heat significantly when placed into the thruster due to ion recombination on the surfaces. The sheaths become incandescent for all discharge voltages above 100 V. In addition, the sheaths sag under the heat load and accurate knowledge of probe position is lost. At higher discharge voltages, the sheaths break and measurements must be halted until a new probe is constructed. This difficultly is solved by using a single multibore mullite tube as the lead sheath. Although mullite has a lower melting point than alumina, it has a higher thermal shock resistance due to its higher thermal conductivity. When inserted into the thruster at high discharge voltages, the mullite sheath shows evidence of severe heating, yet there has never been any sag, or breakage, in this configuration.

A difficulty remains in the current design as presented in Figure 4.20. The probe lifetime is limited by the evaporation of the thoriated tungsten filament. At the probe current utilized, the lifetime of the probe is on the order of several hundred points. There appears to be no solution to this difficulty other than that the probes may be constructed relatively quickly when the materials are at hand.

4.6.2 Test Procedure

A typical test procedure of the emissive plasma potential probe consists of the following steps.

- The probe is placed in the desired position relative to the thruster.
- The cold probe floating potential is noted.
- Power is applied to the variable transformer.
- The voltage of the variable transformer is then raised so that 4.0 A is flowing through the filament.
- The floating voltage of the heated plasma potential probe is recorded.
- Power to the probe is switched off.
- The probe is moved to the next measurement position and the process is repeated.

4.7 Emission Spectroscopy

Emission spectroscopy of the xenon plasma may be performed using the collection optics of the laser velocimetry apparatus shown in Figure 4.18. Scans of the visible spectrum are obtained by placing a Stanford Research Systems SRS-540 optical chopper in front of the monochrometer entrance slit. The resulting scan is recorded on the SRS-850 digital lockin amplifier previously described in section 4.5.1. The monochrometer used is Jarrel Ash 0.5 m Ebert-Fastie monochrometer. The grating is blazed for 600 nm with 600 G/mm. Curved entrance and exit slits are coupled with widths that may be varied from 10 to 425 μm with slit heights as large as 15 mm. With the entrance slit width at 10 μm, the wavelength resolution of these scans is approximately 0.3 Å. For time resolved emission, data are collected using a Tektronics TDS-200 digital oscilloscope. The data are later downloaded from the oscilloscope onto a PC for analysis. For a record of DC emission, a digital voltmeter can be used in place of the oscilloscope for ease of use. In all measurements, the monochrometer slits are full open so that the entire line is captured and no chopper is used for time resolved measurements.

Chapter 5. Results and Discussion

5.1 Thrust Measurements

5.1.1 Prototype Thruster

Table 5.1 contains the results of thrust measurements performed on the prototype Hall thruster. For each test case, the combined flow of the anode and cathode are noted as are the anode voltage, total power, and percentage of power consumed by the anode discharge. In all these thrust measurements, the magnetic field is generated by a magnetic winding current of 2.0 A corresponding to the nominal magnetic field presented in Chapter 4. In all but one case, the cathode mass flow rate is 0.1 mg/s.

Table 5.1. Prototype Thruster Thrust Measurements

Case	Total Flow (mg/s)	Anode Flow (mg/s)	Anode Voltage (V)	Total Power (W)	Anode Power (%)	Specific Power (MJ/kg)	Thrust (mN)
P.1	3.03	2.93	63	238	77	78	8.0 ± 1.7
P.2	3.03	2.93	100	517	88	170	25.0 ± 1.8
P.3	3.03	2.93	85	430	86	142	17.7 ± 0.5
P.4	2.05	1.95	100	277	80	135	11.0 ± 0.2
P.5	2.25	2.15	150	608	91	270	18.2 ± 1.1
P.6	2.05	1.95	150	538	89	262	16.8 ± 1.1
P.7	1.86	1.76	150	411	86	221	14.6 ± 0.6
P.8	2.44	2.34	150	582	91	239	20.6 ± 0.9
P.9	2.54	2.34	150	615	91	242	23.1 ±0.9
P.10	2.05	1.95	150	447	88	218	16.2 ± 0.1
P.11	2.05	1.95	175	577	92	282	18.8 ± 0.3

Table 5.2. Prototype Thruster Performance Parameters

Case	Anode Voltage (V)	Thrust (mN)	I_{sp} (sec)	$\bar{v}$ (m/s)	η
P.1	63	8.0 ± 1.7	270	2650	0.04
P.2	100	25.0 ± 1.8	839	8230	0.20
P.3	85	17.7 ± 0.5	594	5830	0.12
P.4	100	11.0 ± 0.2	544	5341	0.11
P.5	150	18.2 ± 1.1	823	8080	0.12
P.6	150	16.8 ± 1.1	837	8220	0.13
P.7	150	14.6 ± 0.6	784	7690	0.13
P.8	150	20.6 ± 0.9	861	8450	0.15
P.9	150	23.1 ± 0.9	927	9090	0.17
P.10	150	16.2 ± 0.1	805	7900	0.14
P.11	175	18.8 ± 0.3	934	9160	0.15

Table 5.2 shows the derived performance values for the measurements presented in Table 5.1 including specific impulse, mean exit velocity, and efficiency calculated using total mass flow and total system power. Total system power includes power dissipated in supporting the cathode discharge and in producing the magnetic field. Adjustment is not made to account for cathode and magnetic circuit inefficiencies. For all but one case, a minimum of 90% of the mass flow and 80% of the power is dissipated in the main discharge. The prototype Hall thruster design has several limitations. The most severe of these is the inability of the electrical insulator to withstand operations at discharge voltages over 150 V, above which breakage of the alumina insulator invariable occurs.

Figure 5.1 shows measured thrust levels and calculated mean propellant exit velocities for a number of propellant flow rates at a discharge voltage of 150 V. Laser induced fluorescence (LIF) based ion velocity measurements performed on the prototype thruster indicate that the maximum ionic velocities correspond to ion energies equal to the discharge voltage less approximately 50 V (Cedolin). The 50 V differential corresponds to the combined anode and cathode falls. Plasma potential measurements made with a heated

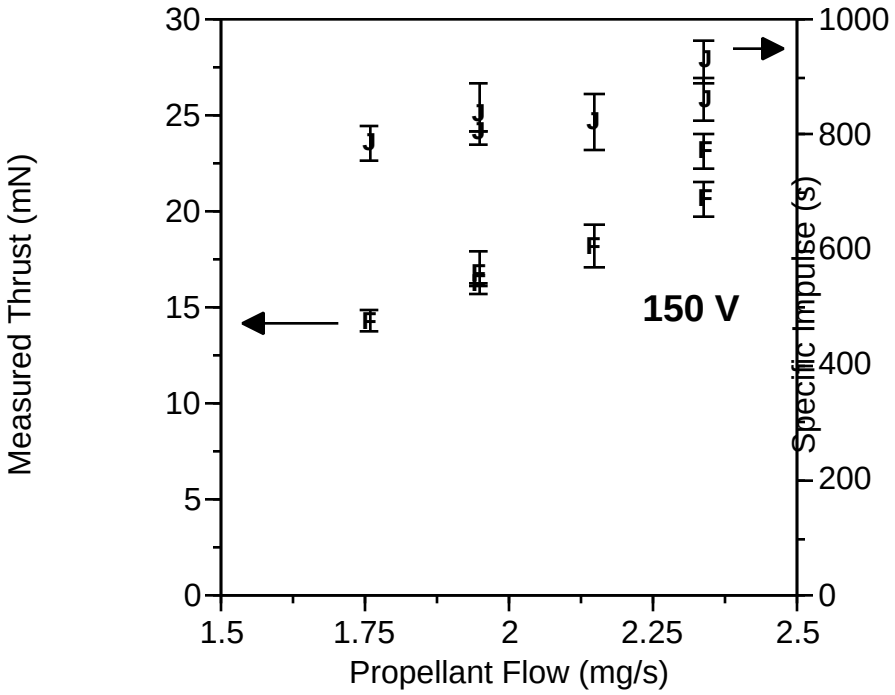

Figure 5.1. Measured thrust and calculated mean propellant exit velocity at a discharge voltage of 150 V and at a variety of propellant flow rates for the prototype thruster.

emissive potential probe substantiate this, showing that at lower discharge voltages the majority of ion acceleration occurs between the thruster exit and the cathode plane. The mean exit velocities calculated from the thrust measurements correspond to approximately 70% of the maximum measured via LIF. This difference is due to incomplete ionization of the propellant, beam divergence, and distribution of the bulk ion velocities.

The mean propellant velocity calculated from thrust measurements increases with increasing propellant flow through the thruster. Similar behavior, where thrust efficiencies increase with propellant flow, is seen elsewhere (Morozov et al., Barnhart et al., Randolph et al.). This is evidence of background xenon ingestion by the acceleration region. Since the vacuum system pumping speed is fixed, the background pressure (~10^{-4} Torr) is proportional to the propellant flow. The amount of ingestion increases proportionally with propellant flow. Therefore, when the expected constant current behavior of the thruster current-voltage characteristics is not in evidence, it is the result of significant ingestion of background neutrals.

Figure 5.2 shows more evidence of the uncertainty introduced by ingestion. The thrust levels measured at higher propellant flows, hence higher background pressures, are significantly higher than those measured at lower propellant flow. If the efficiency of the thruster is taken to be independent of the propellant flow rate, the differences between the trends for 3.03 mg/s and 2.05 mg/s may only be explained by ingestion. However, it is more probable that the efficiency is actually dependent on the propellant flow rate and the differences in the measured trends can not be solely attributed to ingestion. It is problematic to isolate the effect of ingestion on the performance measurement which is also made more difficult by plasma oscillations within the thruster that increase significantly at pressures similar to those in this study (Sankovic et al., Randolph et al.). Accounting for the difficulties and limitations associated with the vacuum system, the thrust measurements should be viewed with some caution.

Figure 5.3 shows the prototype thruster efficiency as a function of the discharge voltage. Several general trends are visible. Efficiency rises with discharge voltage at fixed propellant flow and rises with mass flow at fixed discharge voltage. These effects appear to

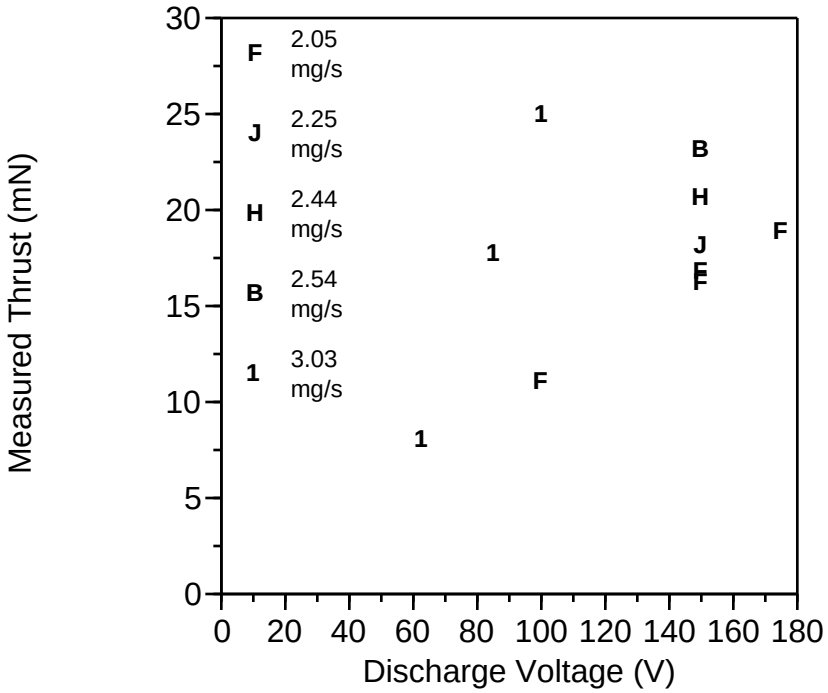

Figure 5.2. Measured thrust of the prototype thruster relative to the discharge voltage for a number of propellant flow rates.

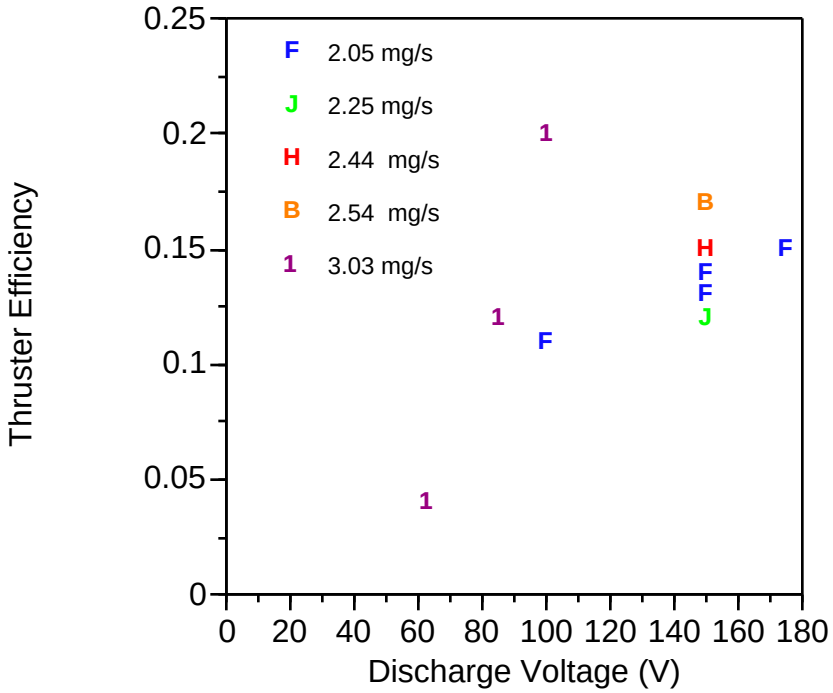

Figure 5.3. Efficiency of the prototype thruster relative to the discharge voltage for a number of propellant flow rates

be amplified at higher propellant flow rates. The peak efficiencies measured are in the neighborhood of 20%, low by the standards of space qualified hardware, but useful as laboratory model with which to study and better understand the physics important to Hall thrusters.

5.1.2 Modified Thruster

Table 5.3 contains the test conditions and results of thrust measurements performed on the modified Hall thruster. In all cases, the cathode mass flow rate is 0.2 mg/s. Unlike the prototype thruster, the magnetic field of the modified device may be varied over a significant range. A majority of the measurements were performed at the maximum winding current for which the main discharge was stable generally corresponding to peak radial magnetic fields ranging between 100 and 200 G. It should be noted that the size of the outer windings on the modified thruster was increased after thrust measurements were performed. Although the magnitude was increased slightly, measurements indicate that the shape of the magnetic field profile did not change.

Table 5.4 presents the derived performance values for the thrust measurements in Table 5.3 including specific impulse, mean exit velocity, and efficiency. As for the prototype thruster, these quantities for the modified thruster are calculated using total mass flow and total system power. Total system power includes power dissipated in supporting the cathode discharge and producing the magnetic field. Adjustment is not made to account for cathode and magnetic circuit inefficiencies. Discharge extinction proved to be the main limiting factor of thruster operation and all measurements were made at magnetic fields below those that led to unstable operation. This extinction may be due to the so-called *loop,* or *circuit,* instabilities, which are in the range of 1-20 kHz (Choueiri). The origins of these instabilities is not completely understood, but are generally believed to be closely coupled to the properties of the external electrical circuit. Others, have reported instabilities due to high test pressures similar to the pressure regime of the Stanford vacuum facility (Sankovic et al., Randolph et al.).

Table 5.3.Modified Thruster Thrust Measurements

Case	Total Flow (mg/s)	Anode Flow (mg/s)	Anode Voltage (V)	Total Power (W)	Anode Power (%)	Magnetic Current (mA)
M1	2.15	1.95	150	425	93	400
M2	2.15	1.95	200	685	95	400
M3	2.15	1.95	250	690	96	600
M4	2.54	2.34	200	689	95	550
M5	2.54	2.34	200	710	96	500
M6	2.74	2.54	200	719	96	600
M7	2.34	2.15	200	631	95	500
M8	2.15	1.95	200	736	97	400
M9	2.34	2.15	250	870	97	500

Figure 5.4 shows the measured thrust and calculated mean exit velocities of the modified thruster at a discharge voltage of 200 V and a number of propellant flow rates. The

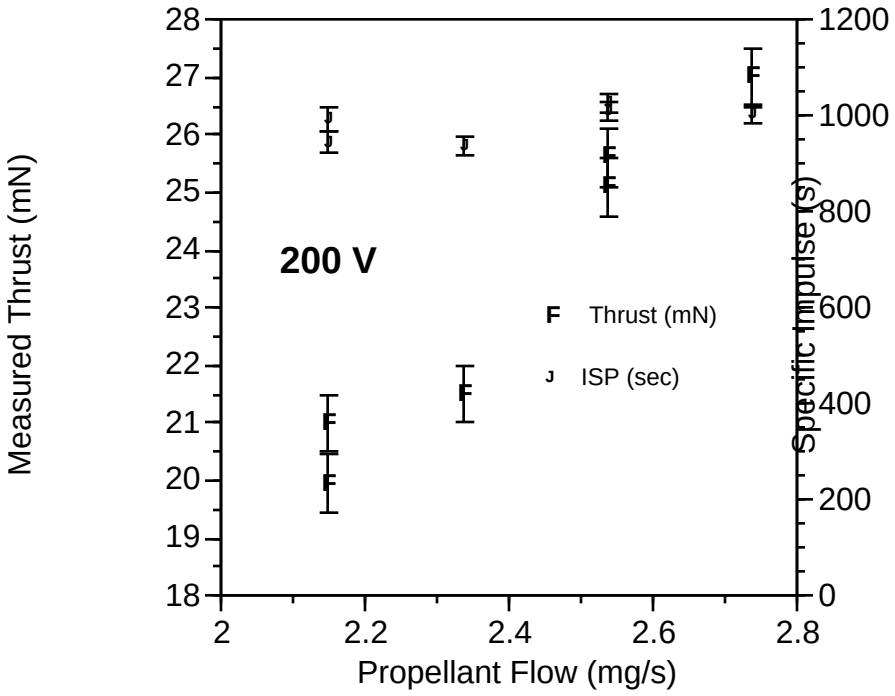

Figure 5.4. Measured thrust and calculated mean propellant exit velocity at a discharge voltage of 200 V and at a variety of propellant flow rates for the modified thruster.

mean axial propellant exit velocity is approximately 10 km/s. This corresponds to an ion beam with mean directed energies of nearly 70 eV. Unlike the prototype thruster, the mean exit velocity does not increase with increasing propellant flow. This indicates that ingestion is less for the modified thruster at this discharge voltage. As for the prototype thruster, the higher mass flow rates also correspond to the highest calculated efficiencies and caution must be taken in interpreting these results.

Figure 5.5 shows the measured efficiency of the modified thruster versus the anode discharge voltage. At the lowest propellant flow rate, increases in efficiency coincide with increases in discharge voltage. At a slightly higher propellant flow, this trend is no longer apparent. The range of thrust measurements taken on the modified thruster is limited by several factors. The thruster does not operate in a stable manner at discharge voltages below 100 V. When the discharge voltage is lowered below this value, the main discharge will extinguish after several minutes. If the discharge voltage is lowered below 60 V, the discharge will immediately extinguish. At discharge voltages above 200 V, operation is also

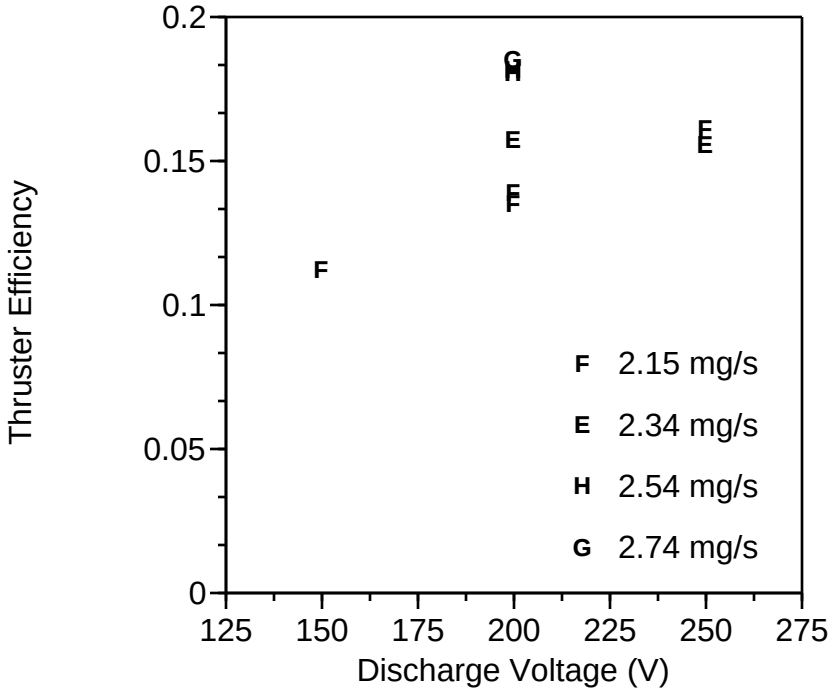

Figure 5.5. Efficiency of the modified thruster relative to the discharge voltage for a number of propellant flow rates.

problematic. The thruster will only operate for several tens of minutes and only at the lower propellant flow rates. After the diffusion pumps of the vacuum facility are cleaned and recharged with new pump oil, the thruster behavior improved dramatically. It is believed that the background pressure within the vacuum facility affects the operation of the Hall thrusters, particularly at higher discharge voltages.

Iron, believed to have sputtered from the front plate of the thruster, was discovered deposited on the insulator which substantially reduced the magnetic field within the acceleration channel. After this phenomena was discovered, the insulator was periodically sand blasted clean. This issue was finally solved by covering the exposed iron components of the thruster front plate with a layer of boron nitride. The magnetic field strength remained steady after this treatment. This effect was only an issue for the modified thruster and no such deposits were found on the prototype thruster, probably due to the more energetic ions produced by the higher discharge voltages of the modified thruster.

Table 5.4. Modified Thruster Performance Parameters

Case	Anode Voltage (V)	Thrust (mN)	I_{sp} (sec)	$\bar{v}$ (m/s)	η
M1	150	14.3 ± 0.5	680	6660	0.11
M2	200	19.9 ± 0.5	945	9270	0.13
M3	250	21.8 ± 0.5	1035	10150	0.16
M4	200	25.1 ± 0.5	1005	9880	0.18
M5	200	25.6 ± 0.5	1025	10070	0.18
M6	200	27.0 ± 0.5	1005	9840	0.18
M7	200	21.5 ± 0.5	935	9190	0.16
M8	200	21.0 ± 0.5	995	9750	0.14
M9	250	25.2 ± 0.5	1095	10750	0.16

It has been reported that for each point of the Hall thruster current-voltage characteristic, an optimum magnetic field strength B^* exists where the discharge current is a minimum (Raistes et al. 1998). At magnetic field strengths below B^*, the electron confinement in the volumetric ionization zone is not optimum, and when the thruster magnetic field strength is above B^*, the plasma instabilities that promote cross-field diffusion of electrons increase. Some of this behavior is evident in the modified thruster. As current through the magnetic circuit increases, the discharge current reduces and approaches an asymptotic value as shown in Figure 5.6. If the magnetic circuit current is further increased, the Hall discharge eventually extinguishes. This behavior initially was believed to be anode electron starvation due to the increased impedance to electron transport of the magnetic field. However at higher discharge voltages, spontaneous extinction of the discharge occurs at relatively low magnetic fields. Experience has shown that at a constant magnetic current, increasing the discharge voltage will eventually result in discharge extinction. The only way to perform measurements at higher discharge voltages is to decrease the magnetic current and thus the radial magnetic field strength. This results in an increased discharge current and is responsible for the lack of measurements at voltages approaching 300 V due to the hollow cathode neutralizer current limitations (5.0 A).

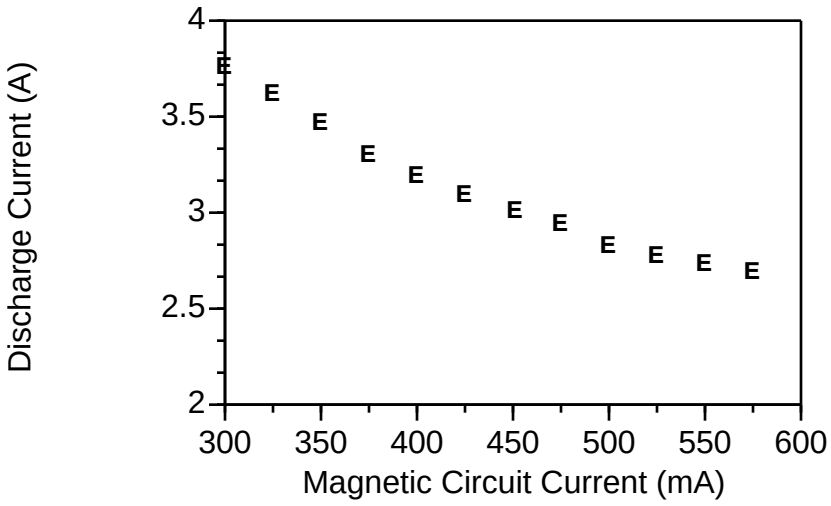

Figure 5.6. Variation of the main discharge current in the modified Hall thruster main as a function of magnetic circuit current. Total propellant flow of 2.54 mg/s at a main discharge voltage of 125 V.

The effect of the vacuum system on thruster operation can not be ignored. The limited pumping speed results in background pressures on the order of 10^{-4} Torr. Ingestion of background gases into the Hall thruster during operation almost certainly occurs. Ingestion has the effect of both increasing the discharge current and the measured thrust since a portion of the ion acceleration occurs beyond the Hall thruster exit plane. Operation of the thruster at lower chamber pressures would eliminate these uncertainties. It has been estimated that performance data should be taken at pressures less than $5x10^{-5}$ Torr (Randolph et al.). Other chamber effects must also be considered, especially back streaming of oil from the diffusion pumps. The diffusion pumps on the Stanford vacuum facility use a silicone based oil (Dow Corning 605). During testing, an oil film coats surfaces within the vacuum chamber including the insulator and anode. Some of the difficulties experienced during testing may have been due to layers of chemically modified diffusion pump oil on various thruster surfaces. These generally manifest themselves as a brown, or black, discoloration on surfaces within the vacuum facility.

Despite difficulties, thrust measurements of both the prototype and modified Hall thrusters have been performed and have shown that efficiencies near 20% are achieved in these laboratory devices. While this efficiency is relatively low compared to space qualified Hall thrusters, it is reasonable for laboratory models and certainly suitable for use as test

beds for increasing understanding of basic physics occurring within the Hall thruster. Due to the limited operational range of the prototype Hall thruster, the remainder of this study focuses on the modified Hall thruster. It is capable of operating at higher discharge voltages which are more representative of the operation of Hall thrusters used for satellite propulsion applications.

5.2 Laser Induced Fluorescence Velocimetry of the Xenon Ion

5.2.1 Saturation Study

In order to measure the spatially resolved velocity profiles of xenon ions in the plasma discharge of the Hall thruster, the $5d[4]_{7/2} - 6p[3]_{5/2}$ ionic xenon transition at 834.7 nm was probed to extract local velocity data from the Doppler shift of the measured fluorescence. Figure 5.7 shows the saturation fluorescence curve of the transition at a location 13 mm from the exit plane and at the center of the acceleration channel. Here, the laser beam is propagating normal to the thrust vector and is measuring a near zero radial velocity component for the xenon ions. A typical saturated trace used to determine the velocity in the probed volume is compared to an unsaturated trace from the same location in Figure 5.8. Both traces are normalized to unity peak signal.

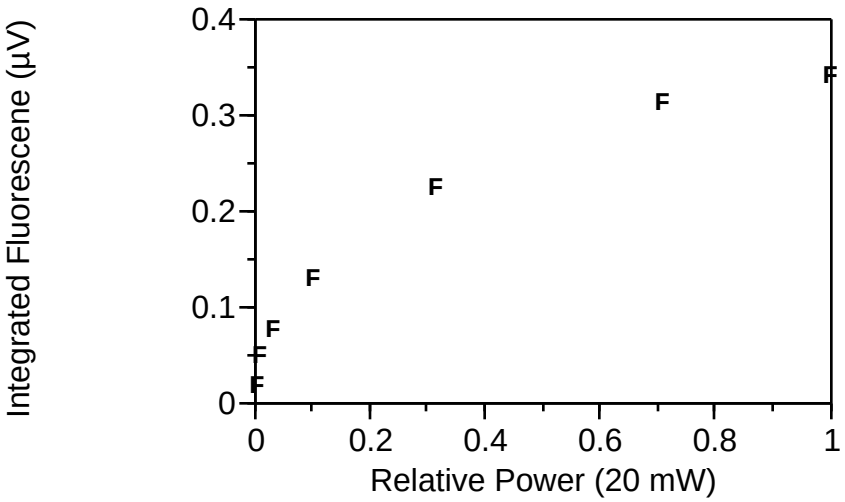

Figure 5.7. Saturation curve for the ionic xenon $5d[4]_{7/2} - 6p[3]_{5/2}$ transition.

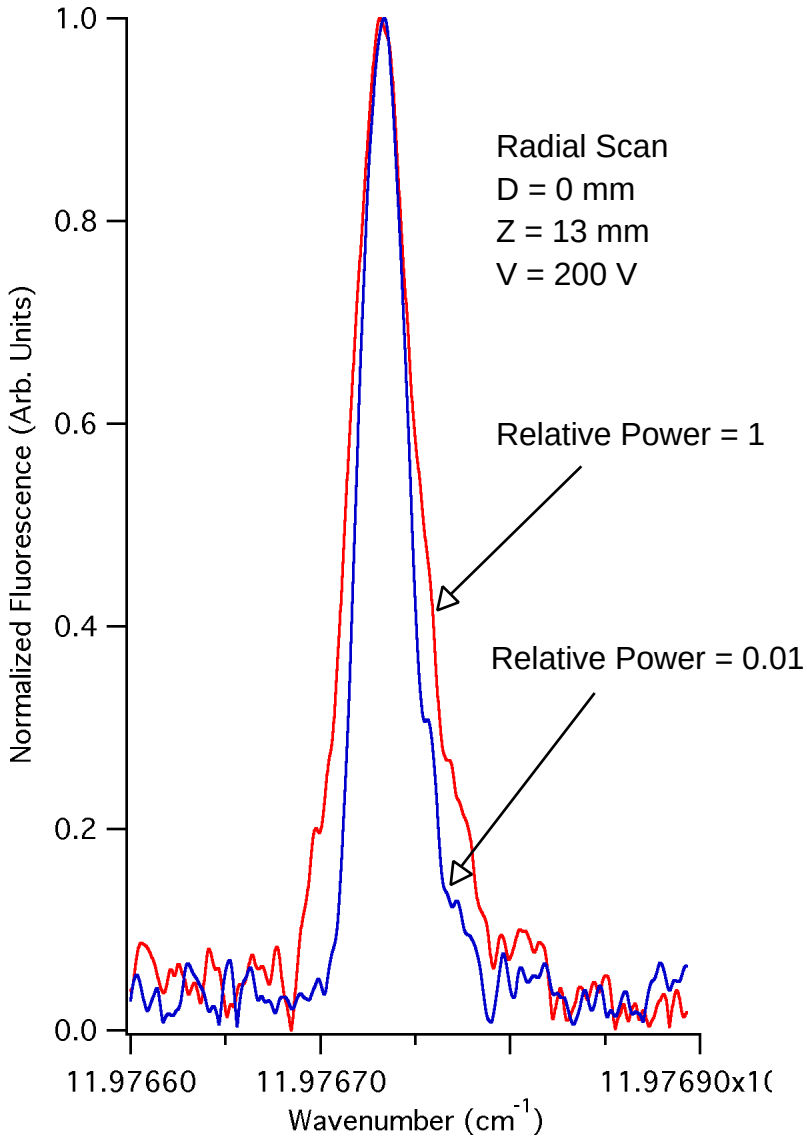

Figure 5.8. Typical fluorescence trace (outer trace) compared to an unsaturated trace (inner trace). Note that the fluorescence signals in each case have been normalized.

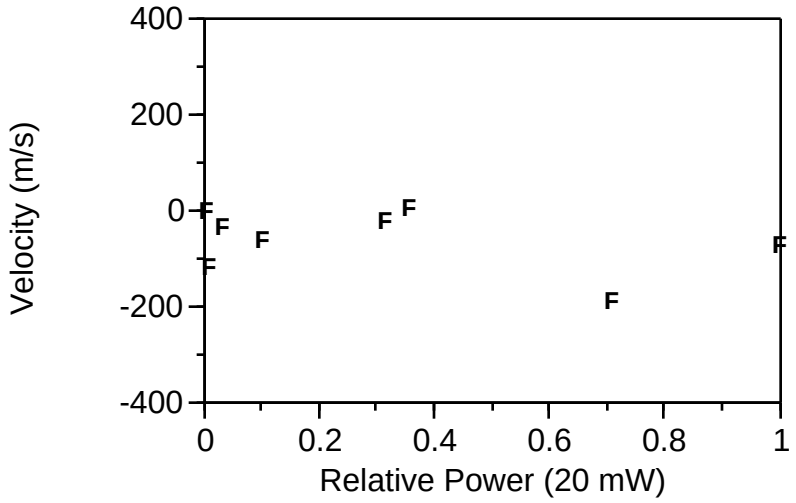

Figure 5.9. Measured ion velocities for a variety of saturation parameters.

Velocity measurements for each of the saturated line shapes making up Figure 5.7 are shown in Figure 5.9. The mean velocity for these data points yields a value of -62 m/s with a standard deviation of 65 m/s and a range of 127 m/s. The uncertainty of the measurements is determined by the uncertainty of the wavelength measurements which is equivalent to approximately ±500 m/s. The most important conclusion that can be drawn from Figures 5.7 and 5.9 is that the $5d[4]_{7/2} - 6p[3]_{5/2}$ ionic transition of xenon will provide useful LIF velocimetry data when partially saturated which is within the uncertainties of the measurement of the Doppler shift. This conclusion allows the collection of saturated fluorescence signals, maximizing the signal to noise ratio and allows faster scans to be taken while still extracting velocity data.

All spatially resolved measurements are referenced to a two coordinate reference system. The position in the radial coordinate is referenced from the distance to center of the acceleration channel D as shown in Figure 5.10. The axial coordinate is given by Z which is the distance from the thruster exit plane and is defined as positive along the thrust vector. These two coordinates are defined in Figure 5.10 relative to the modified Hall thruster.

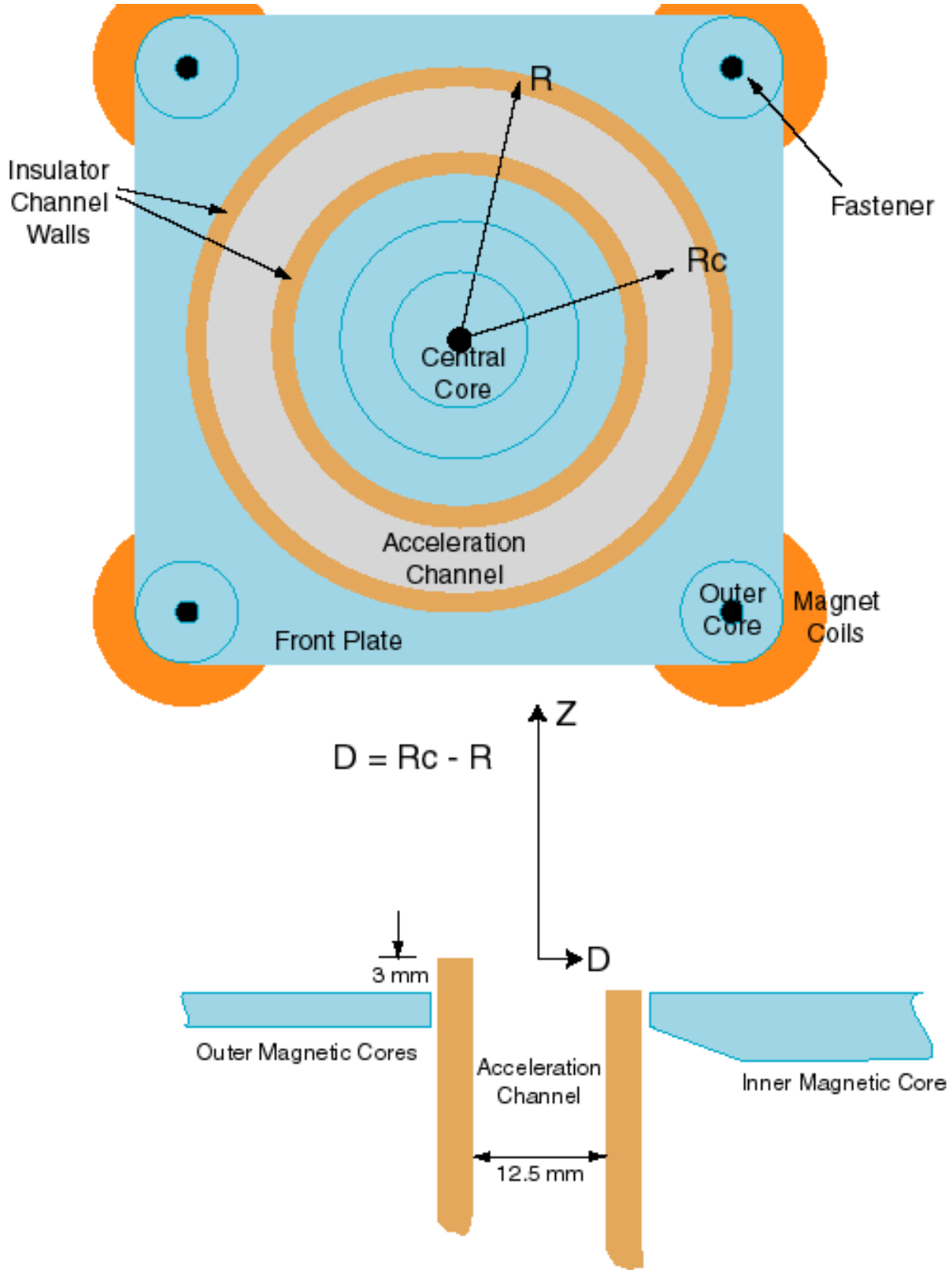

Figure 5.10. Position reference used for all spatially resolved measurements.

5.2.2 Initial Measurements with the Slotted and Unslotted Insulator

An initial set of external velocity measurements were taken at a discharge voltage of 160 V. These measurements consisted of axial velocities in a cylindrical sample volume 2 mm in length with a 100 μm diameter as defined by the focused probe beam and the aperture of the collection optics. The measurements were taken with probe volumes separated by 2.5 mm on center. After these initial measurements, the original Hall thruster insulator was replaced with the slotted insulator. The slot is approximately 1 mm wide and provides optical access into the interior of the thruster. A second set of measurements were then performed to determine if the presence of the slot significantly perturbed the ion velocity field. The results of these measurements are shown in Figure 5.11. The diamond symbols denote the velocity data taken on the thruster with the unslotted insulator while the round symbols are from the thruster with the slotted insulator. Both data sets overlap and indicate that slot does not significantly affect the propellant acceleration. Although the axial ionic velocities taken on the thruster with the slotted insulator are slightly lower than those for the

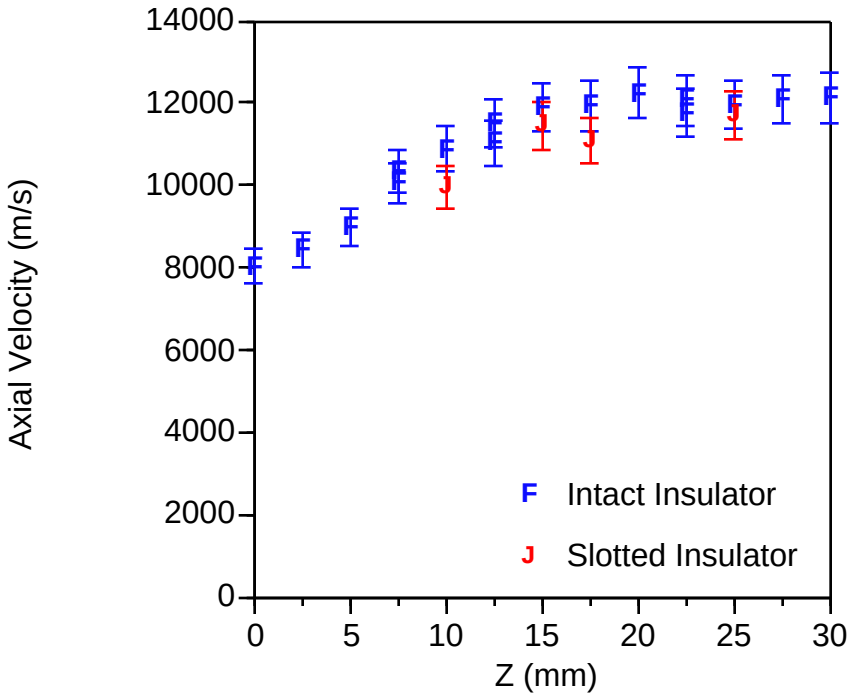

Figure 5.11. Comparison of axial velocities measured for thruster with slotted and intact insulators at a discharge voltage of 160V and at D = 0 mm.

nominal case, the overlap of the uncertainties associated with the measured Doppler shifts precludes a general statement.

Ideally, thrust measurements would indicate the effect the slot has on the behavior of the Hall thruster; however, a thrust stand was not available for this purpose. The current-voltage characteristic showed no obvious departure from the norm established by the unslotted insulator configuration. This is deemed to be a good measure of the effect of the slot on the thruster as a whole. The slot could provide a path for electrons to bypass the magnetic confinement near the exit plane. The lack of change in the current-voltage characteristic between the two configurations indicates that there is no significant leakage of electron current through the slot. Experience with the prototype thruster has shown that insulator breakage will lead to increased anode current due to electron current bypassing the high magnetic field, high impedance, portion of the acceleration channel. This behavior is not exhibited by the thruster with the slotted insulator.

The slot does not affect Hall thruster operation since the local electron Larmor radius is on the same order or larger than the slot width and depth through the insulator. Electrons are therefore not able to utilize the slot to enter, or exit, the acceleration channel. Although the overall performance of the thruster does not appear to be affected by the slot, scorch marks outlining the slot are visible on the phenolic thruster mount after every extended run. Some plasma leakage through the slot is occurring during operation. However, the leakage is not sufficient to adversely affect the operation of the Hall thrusters in the examined operating regimes.

5.2.3 Axial Velocity Measurements

With the exception of the data at a discharge voltage of 160 V, all the axial velocity data consist of two sets of data taken with the slotted insulator. The first set consists of ionic velocities taken externally extending from the exit plane to approximately Z = 35 mm. The second data set consist of internal axial velocity data from the exit plane to approximately Z = -75 mm. These limits are imposed by the limited range of the translation stage providing axial motion of the Hall thruster. Between the two data sets, the translation stage had to be manually repositioned within the vacuum chamber so that the subsequent data set could be taken. Data points were taken every 2.5 mm with a sample probe volume 100 μm

in diameter and 2 mm length. Overlap of the two data traces ensures that the measurements are continuous. For several test conditions, profiles of the axial velocity across the coordinate D are also examined.

The complete axial velocity profiles for the four test conditions are shown in Figures 5.12 to 5.15. The error bars correspond to the uncertainty associated with the determination of the magnitude of the Doppler shift. The axial velocity profiles exhibit a common behavior. The velocity is near zero close to the anode (Z = -78 mm), and only begins to rise near Z = -10 mm. The ions are rapidly accelerated near the exit plane and reach their full velocity in the neighborhood of Z = 20 mm. This latter position corresponds to the axial location of the hollow cathode neutralizer relative to the body of the thruster and is often referred to as the *cathode plane* (Manzella 1994).

The length of the acceleration region for each case shown in Figures 5.12 to 5.15 is invariant at 30 mm. For each case, the acceleration occurs over a finite length, and increases in the anode potential result in linearly increased electric fields within the acceleration channel. The propellant acceleration initially begins 10 mm within the thruster where the magnetic field has a value of approximately 85% of the centerline (D = 0 mm) maximum. The propellant acceleration is completed 20 mm beyond the exit plane where the magnetic field has a value of approximately 25% of the centerline maximum. Table 5.5 presents an analysis of the relative contributions of the external and internal axial acceleration of the propellant. This table quantifies some of the important information contained in the

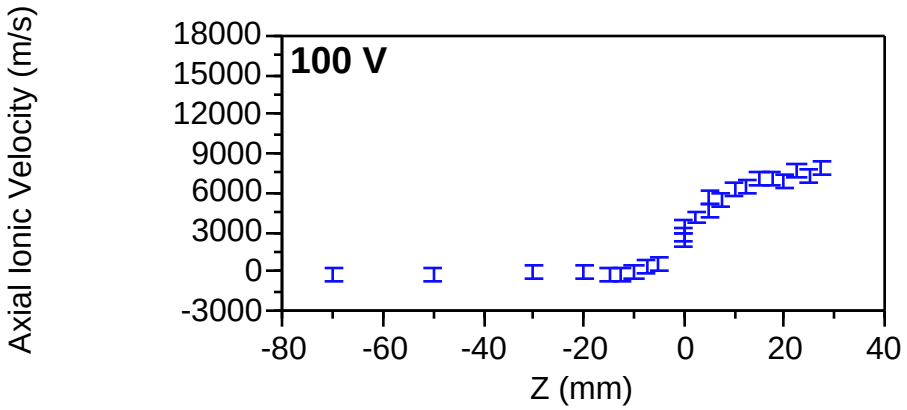

Figure 5.12. Axial velocity profile for the 100V discharge voltage case at D = 0 mm.

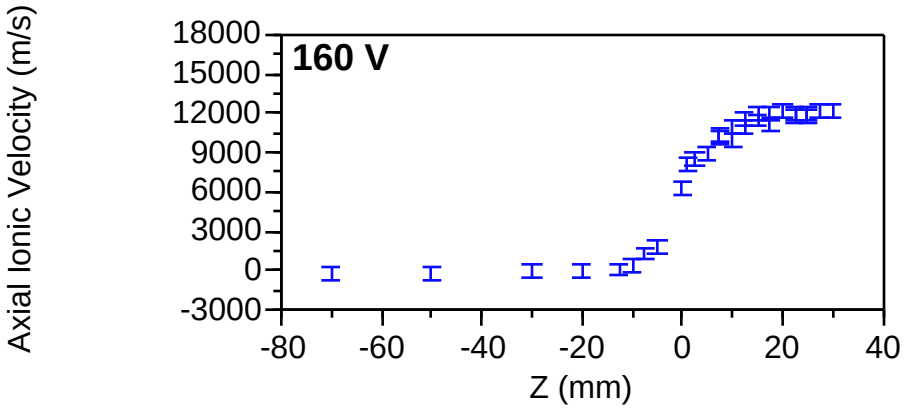

Figure 5.13. Axial velocity profile for the 160V discharge voltage case at D = 0 mm.

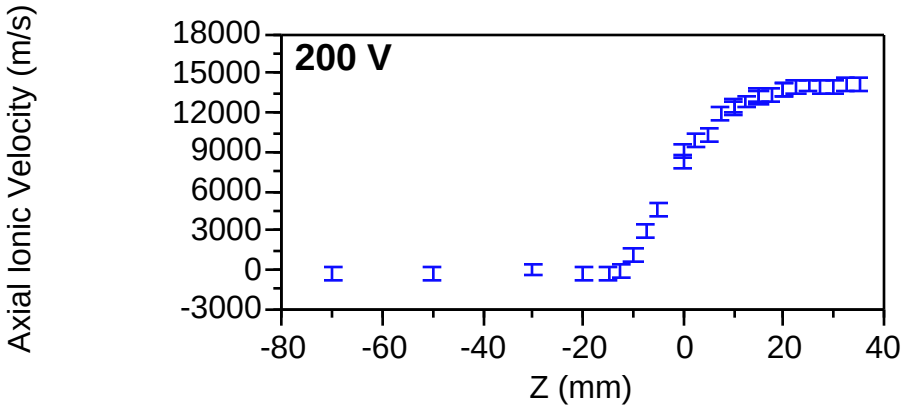

Figure 5.14. Axial velocity profile for the 200V discharge voltage case at D = 0 mm.

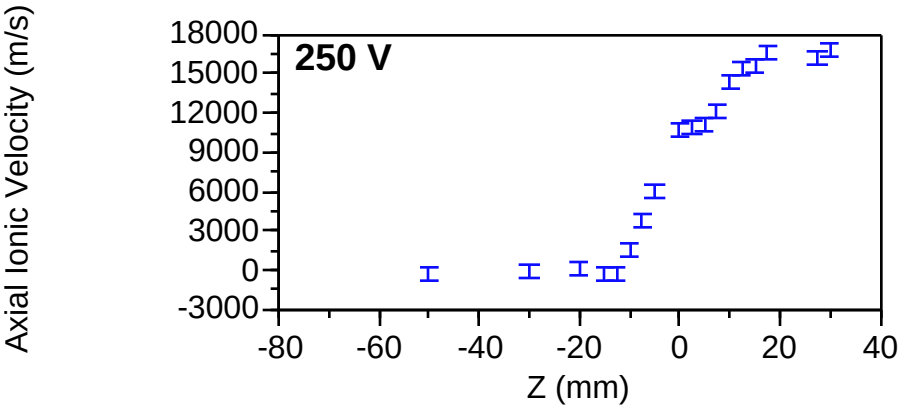

Figure 5.15. Axial velocity profile for the 250V discharge voltage case at D = 0 mm.

axial ionic velocity profiles shown below. The first issue is the acceleration occurring outside the thruster. Taking into account the uncertainties inherent to the velocity measurements (±500 m/s), the velocity imparted into the propellant outside the Hall thruster is nearly constant with an average value of 5,000 m/s. Only for the case of a 100 V discharge voltage, does the majority of the acceleration occur outside the thruster. Higher discharge voltages have a constant percentage of the acceleration occurring externally. It is also informative to examine the energy deposited into the propellant in Table 5.5. In the case of a 100 V discharge voltage, approximately 90% of the energy is deposited into the propellant beyond the exit plane. For all discharge voltage cases above 160 V, the fraction of energy deposition beyond the exit plane is nearer to 60%. Therefore in all cases, the majority of the energy deposition into the Hall thruster propellant stream occurs outside the thruster body. However since the thrust is equivalent to the momentum flux, the majority (~65%) of the thrust is still generated within the thruster body in all cases but the 100 V discharge voltage case.

Table 5.5. Ion acceleration through the Hall thruster for various discharge voltages

Property	100 V	160 V	200 V	250 V
Exit Plane: Velocity	2,900 m/s	8,000 m/s	9,200 m/s	10,800 m/s
Energy	5 eV	44 eV	58 eV	79 eV
Maximum: Velocity	8,000 m/s	12,200 m/s	14,200 m/s	16,800 m/s
Energy	44 eV	102 eV	138 eV	191 eV
External Acceleration	5,100 m/s	4,200 m/s	5,000 m/s	6,000 m/s
(% of maximum)	(65%)	(35%)	(35%)	(35%)
External Energy	39 eV	58 eV	80 eV	112 eV
(% of maximum)	(90%)	(55%)	(60%)	(60%)
Lost Energy	56 eV	58 eV	62 eV	59 eV
(% applied voltage)	(55%)	(35%)	(30%)	(25%)

An important measure of the losses occurring in the Hall thruster is shown by examining the energy that does not contribute to the acceleration of the propellant. In all the

test cases, approximately 60 eV does not contribute to propellant acceleration. This value is constant to within the uncertainties of the velocity measurements which implies that the mechanism responsible for this loss is invariant with the applied anode potential. This energy loss is most likely a product of the anode and cathode potential falls and other mechanisms inherent to the thruster design. It must be noted that the measurements presented thus far are limited to axial velocities and do not account for losses due to plume divergence.

A feature that all the axial velocity profiles in Figures 5.12 to 5.10 exhibit is a barely perceptible local maximum in the measured axial velocity between Z = -20 and -30 mm. Velocities around this region are negative indicating that the excited state ions probed during the measurements are moving toward the anode. The physics of Hall thruster operation require that a fraction of the ions flow toward the anode along with the electron current so that plasma neutrality holds throughout the Hall thruster. Back flow of ions in the deep interior is therefore expected. The apparent local maximum may alternatively be a manifestation of high frequency transient behavior occurring within the acceleration channel, possibly related to the ionization process. However, it should be noted that the velocities in this region of the Hall thruster are in the neighborhood of 1,000 m/s and have absolute uncertainties of ± 500 m/s.

In addition to the axial velocity profiles shown in Figure 5.12 to 5.15, several radial profiles of the axial ionic velocity are shown in Figures 5.16 and 5.17. Figure 5.16 shows the radial variation of the measured axial velocities for a discharge voltage of 160 V at two locations in the plume. The width of the acceleration channel is approximately 12 mm (-6 mm < D < 6 mm) and it is evident that the plume is sufficiently diverged at the locations examined that the axial velocity profile is flat. Internally, the behavior is similar to that in the plume. Figure 5.17 shows a radial profile of the axial velocity at a discharge voltage of 200 V at Z = -5 mm. The axial velocity profile at this location and condition is also flat. Figure 5.17 strongly implies lines of constant potential within the acceleration channel in the radial direction. Beyond the exit plane, the flatness of the velocity profile also appears to indicate radial lines of constant potential.

The axial velocities in Figures 5.12 to 5.15 can be converted into relative potential curves by converting the measured velocity values into ionic kinetic energy values. The resulting plots are shown in Figures 5.18 through 5.21. These calculations show the evolu-

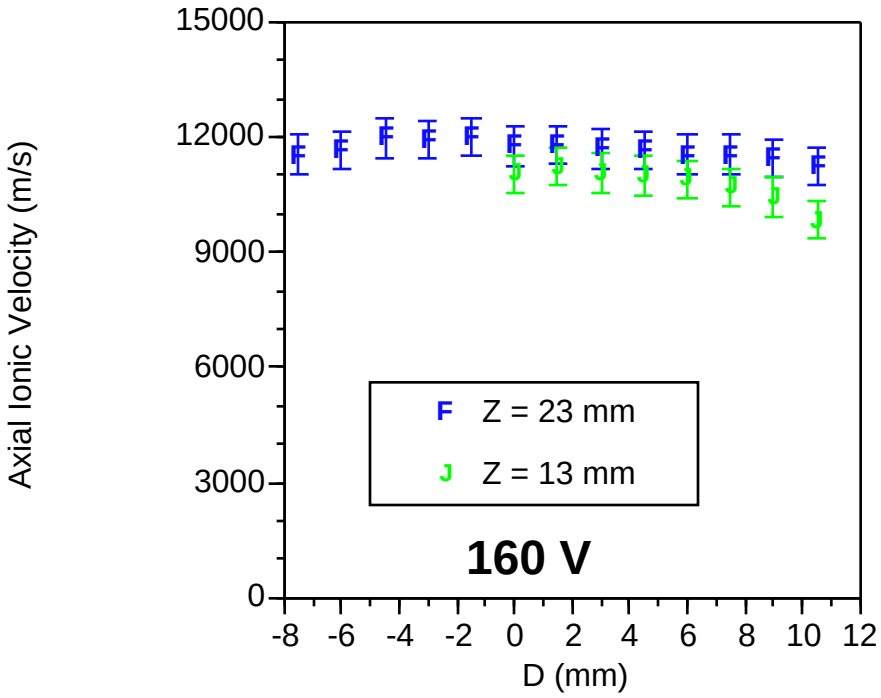

Figure 5.16. Radial profiles of axial velocities at two axial plume locations for a discharge voltage of 160 V.

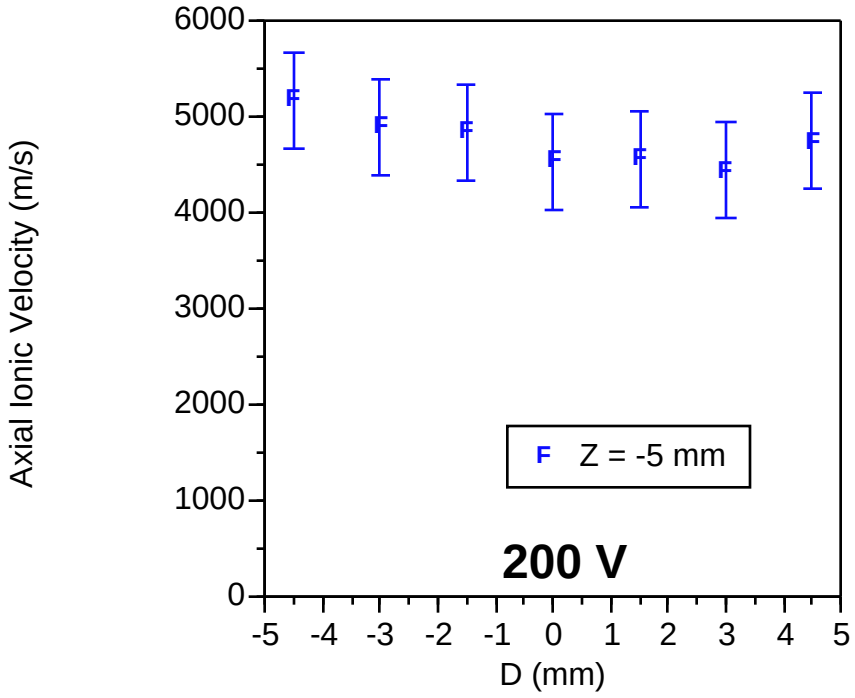

Figure 5.17. Radial profile of axial velocities at one internal axial location for a discharge voltage of 200 V.

tion of the energy deposition into the propellant as it is accelerated out of the Hall thruster and into the plume. The general features are similar in all cases. The energy deposited into the propellant is not significant until approximately 10 mm before the exit plane. At this point the energy deposited into the propellant rapidly increases until about 20 mm beyond the exit plane. The energy deposition shown in these figures is the negative of the potential slope which accelerates the ionized propellant. All the energy deposition curves with discharge voltages above 100 V also exhibit an unexpected feature near the exit plane (Z = 0 mm) which manifests itself as a flat portion of the energy deposition curve. At this location, significantly reduced acceleration of the propellant is occurring.

This feature is more in evidence if the axial electric field strength is calculated from the ion kinetic energies. The axial electric field calculated from the laser velocimetry of the propellant ions is shown in Figures 5.22 through 5.25. Each curve is made up of 100 linearly interpolated points which are smoothed and numerically differentiated to produce a profile of the electric field. The flat portions of the energy deposition curves manifest themselves as troughs in the electric field. In each of the cases with discharge voltages above 100 V, a trough is present just beyond the exit plane. This behavior was not expected apriori. Rather, it was expected that the potential, and hence the electric field, would exhibit smooth continuous behavior. However, the appearance of distinct and repeatable features indicates that this is not so.

It is interesting to note that near the exit plane a very low electric field is indicated. This sudden change in the electric field at the exit plane increases with increased discharge voltage. If it can be assumed that the axial current is a constant and since the local radial magnetic field is continuous, the dips in the electric field may be attributed to changes in the local plasma conductivity indicating either a sharp drop in the electron temperature, a rise in the electron density, or plasma fluctuations. The measured electron temperature does not support the former; therefore, a sharp rise in the electron density may be responsible. A possible explanation for a rise in electron density is that due to the high back pressure within the vacuum facility (10^{-4} Torr) there may be a second ionization zone near the exit plane of the thruster. Backstreaming electrons ionizing background neutrals could produce a higher plasma density in this region thus increasing the local plasma conductivity and lowering the

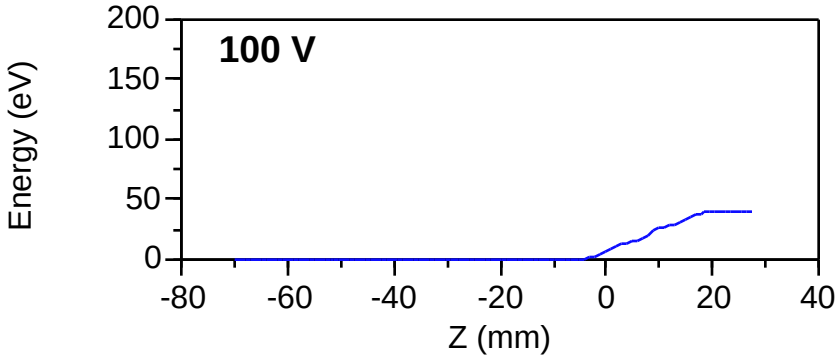

Figure 5.18. Energy deposition at a discharge voltage of 100V.

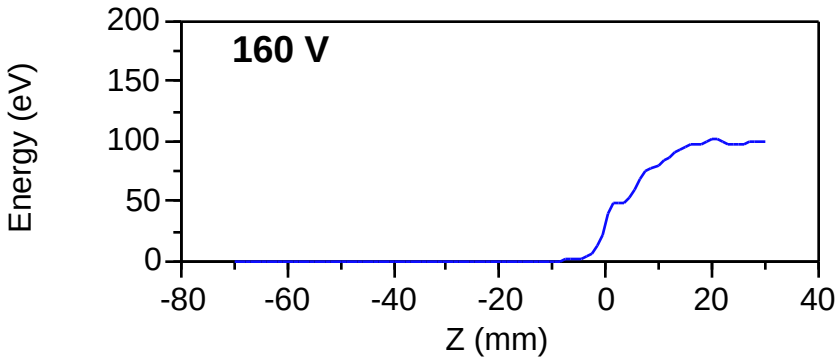

Figure 5.19. Energy deposition at a discharge voltage of 160V.

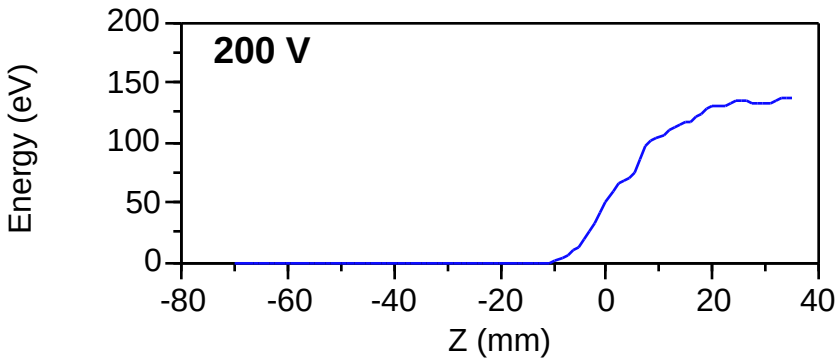

Figure 5.20. Energy deposition at a discharge voltage of 200V.

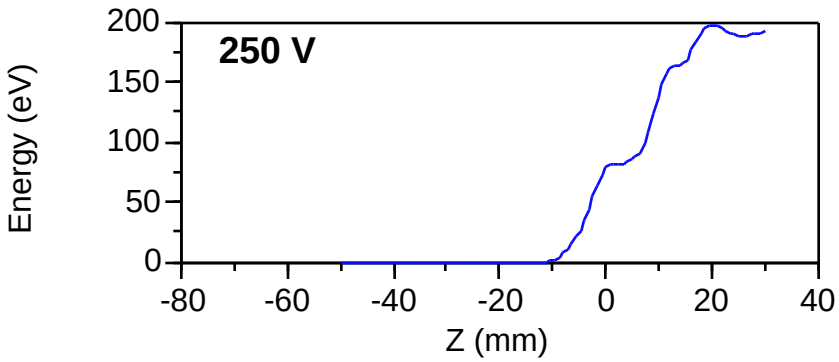

Figure 5.21. Energy deposition at a discharge voltage of 250V.

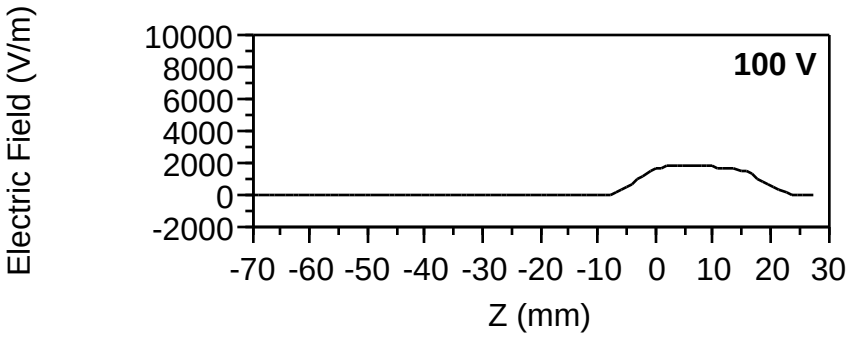

Figure 5.22. LIF derived electric field for discharge voltage of 100V.

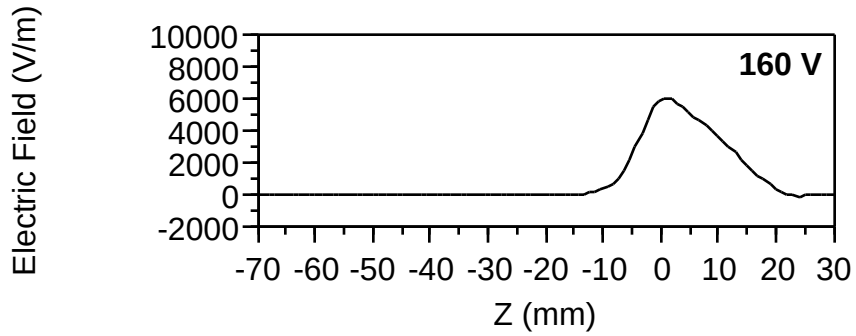

Figure 5.23. LIF derived electric field for discharge voltage of 160V.

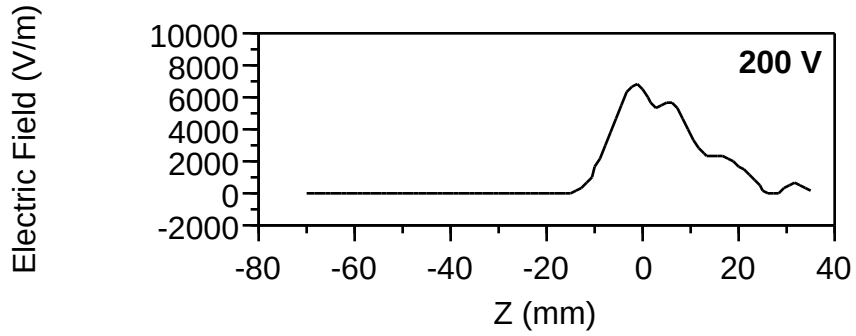

Figure 5.24. LIF derived electric field for discharge voltage of 200V.

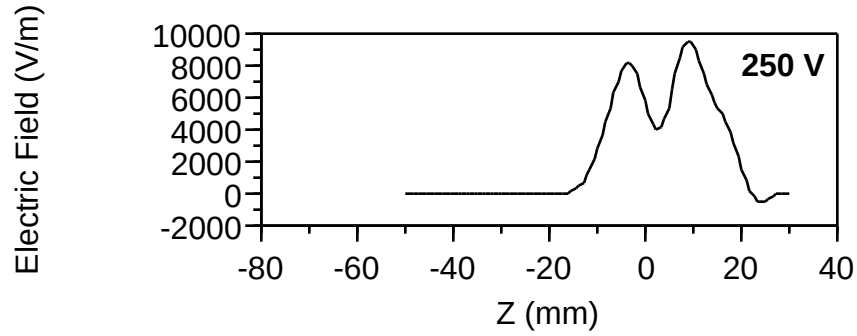

Figure 5.25. LIF derived electric field for discharge voltage of 200V.

local electric field. Plasma oscillations have been shown to be the cause of so called *anomalous diffusion* of electrons through magnetic field lines. Recent studies have shown that significant plasma density oscillations with a characteristic frequency in the region of 10 kHz occur near the exit plane. These oscillations are capable of increasing the local plasma conductivity and lowering the electric field.

5.2.4 Radial Velocity Measurements

Typical results of radial ionic velocity measurements are shown in Figures 5.26 to 5.29. These graphs show the radial component of the ionic propellant flow 13 mm beyond the thruster exit plane (Z = 13 mm). The measurement volume consists of a cylinder 900 μm in length with a 150 μm diameter as defined by the focused probe beam and the aperture of the collection optics. The difference in the collection volume between these measurements and the previously described axial velocity measurements is due to the different orientation of the entrance slit of the monochrometer used as a narrow band filter and changed probe beam focusing optics. Each series of radial velocity measurements are taken with probe volumes separated by 1.6 mm on center. The axial location of the measurements was chosen to be Z = 13 mm since the majority of the acceleration is completed and measurements here should provide an indication of the divergence of the flow that could be compared between the various operating conditions. The measurements presented in Figures 5.26 to 5.29 show that the propellant stream has a substantial radial velocity component. The radial velocity profile appears to be symmetrical and linear. At the centerline of the acceleration channel (D = 0 mm), the radial velocity is near zero.

Using the axial velocity data in Figures 5.12 to 5.15 and the radial velocity data with the knowledge that the axial velocity across the acceleration channel is independent of D, several vector plots of the near Hall thruster plume may be constructed. Figure 5.30 shows the vector plot of two sets of radial measurements while Figure 5.31 shows a similar vector plot of three sets of radial measurements. Shown below each vector plot is an auxiliary figure with flow angles determined from the radial and axial velocities. From the auxiliary flow angle plot in Figure 5.31, it is evident that the plume is externally focused to a minimum between 5 and 23 mm beyond the exit plane. This behavior is evident to the eye during operation. The plume contracts to a minimum cross-section at a location outside the

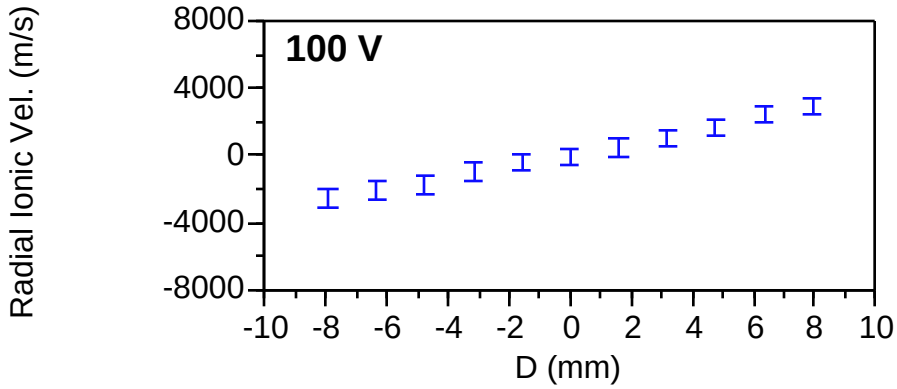

Figure 5.26. Radial velocity at D = 13 mm for a discharge voltage of 100 V.

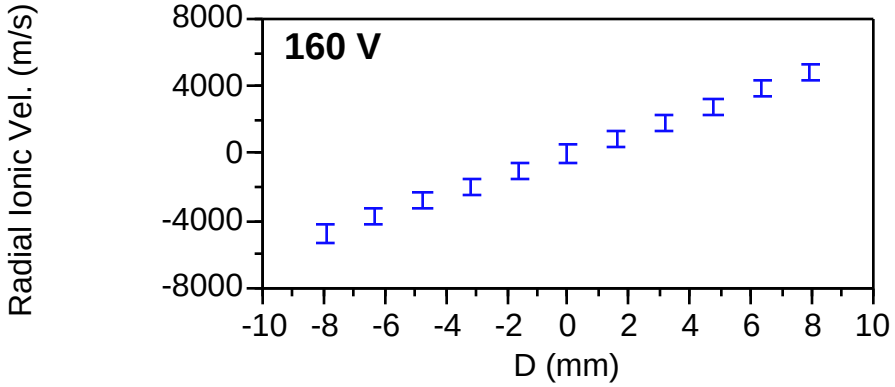

Figure 5.27. Radial velocity at D = 13 mm for a discharge voltage of 160 V.

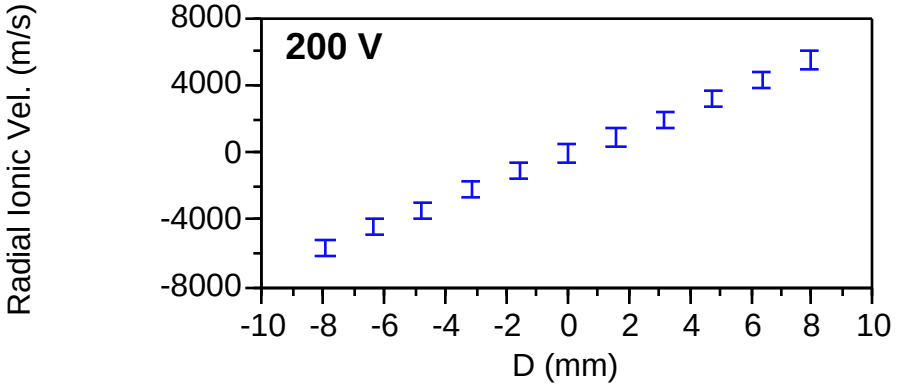

Figure 5.28. Radial velocity at D = 13 mm for a discharge voltage of 200 V.

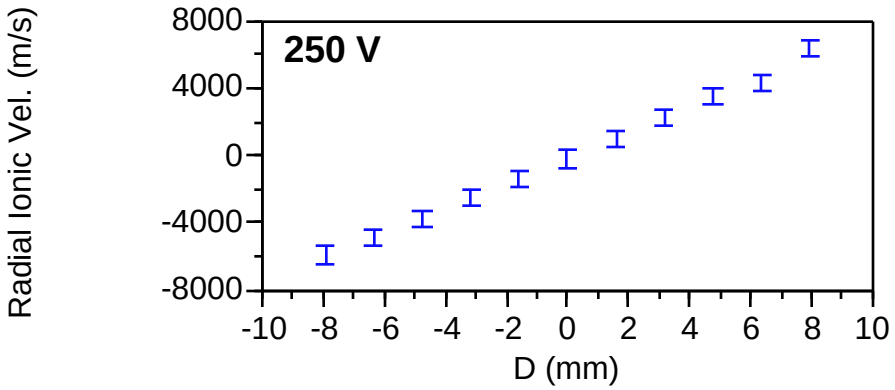

Figure 5.29. Radial velocity at D = 13 mm for a discharge voltage of 250 V.

acceleration channel and then expands. Various sources in the literature have called this behavior a self focusing of the plume and it is most evident at higher discharge voltages (Fife and Martinez-Sanchez 1998).

One of the brightest features in the plume is the central core of the plume. The propellant stream exits the thruster from an annulus, but an intense, optically emitting conical plume starting on the central magnetic core and extending some distance into the vacuum chamber is evident at higher discharge voltages. The inward focus of the data points D > 0 mm likely accounts for the observed plume structure and a portion of the self focusing of the plume.

Figure 5.32 shows the energy lost into radial velocity per ion plotted as a function of radial coordinate D for the four test conditions at an axial location of Z = 13 mm. The losses are a strong function of the discharge voltage. At an anode potential of 100 V, the energy loss at D = 8 mm is slightly less than 5 eV per ion. A 60% increase of the discharge voltage to 160 V increases the loss at D = 8 mm by more than a factor of 3 to approximately 15 eV per xenon ion. Further increases of the discharge voltage appear to produce proportionally lower radial energy losses which may be due to the self focusing of the plume if the plume focus is approaching the axial position of the measurements (Z = 13 mm) as the discharge voltage is increased.

Figure 5.33 shows the radial electric field component calculated from Figure 5.31. It should be noted that the electric fields in this plot are referenced to the spatial variable D which differs from the radius by its sign. The data shows surprisingly strong radial

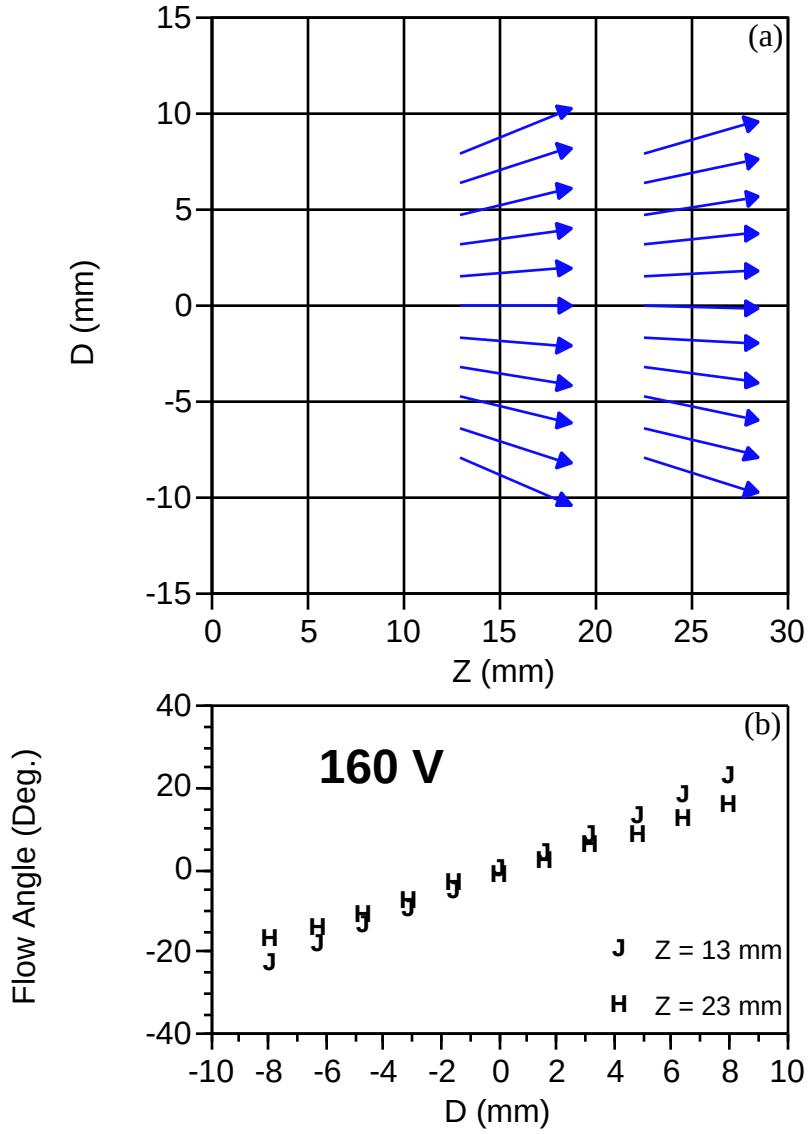

Figure 5.30. (a) Vector plot of radial and axial components of the ionic velocity at a discharge voltage of 160 V. (b) Plot of the estimated flow angles.

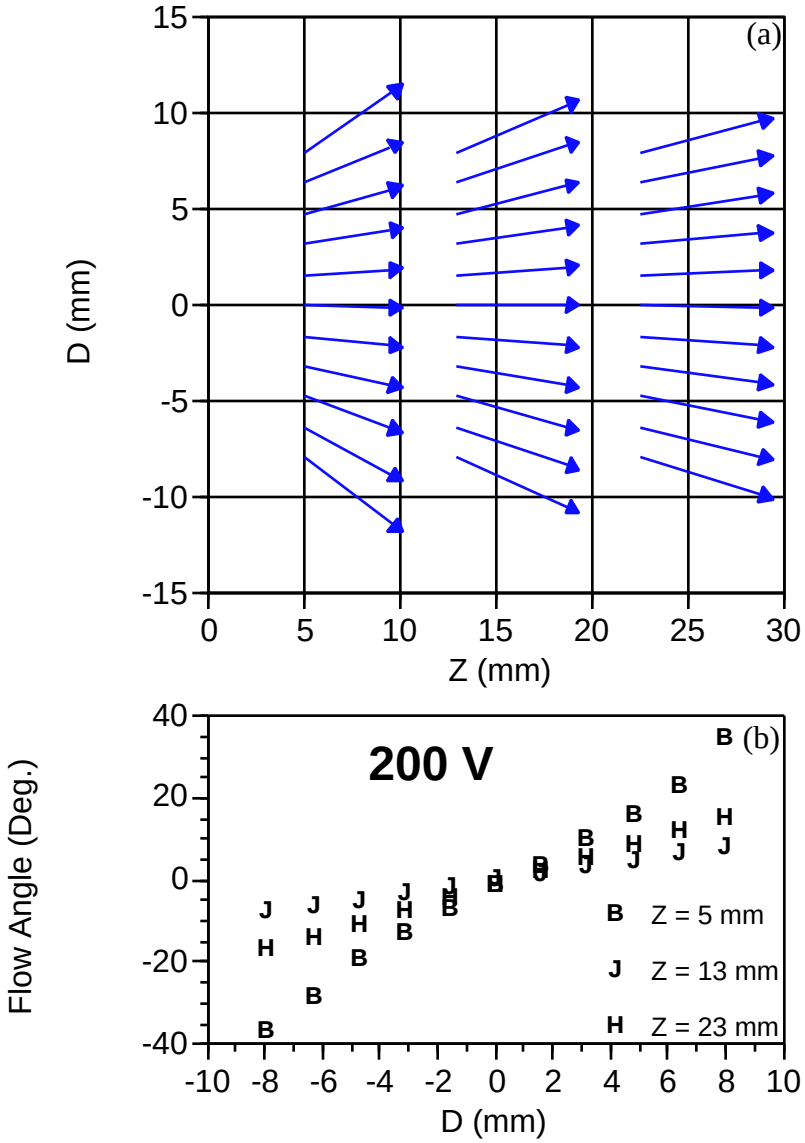

Figure 5.31. (a) Vector plot of radial and axial components of the ionic velocity at a discharge voltage of 200 V. (b) Plot of the estimated flow angles.

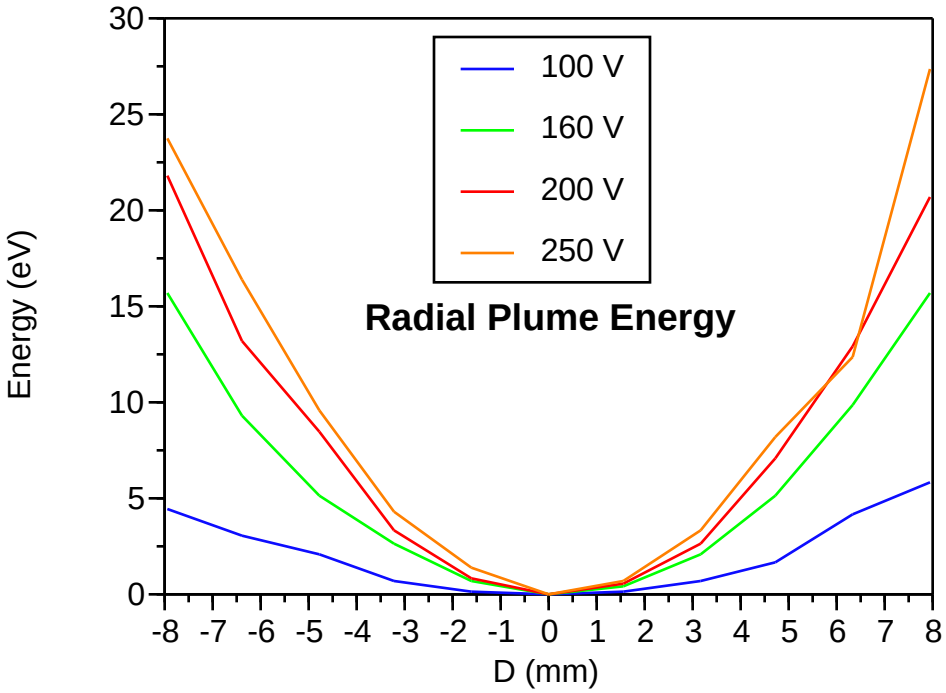

Figure 5.32. Radial component of plume energy at Z = 13 mm relative to acceleration channel centerline (D = 0 mm) for several discharge voltages.

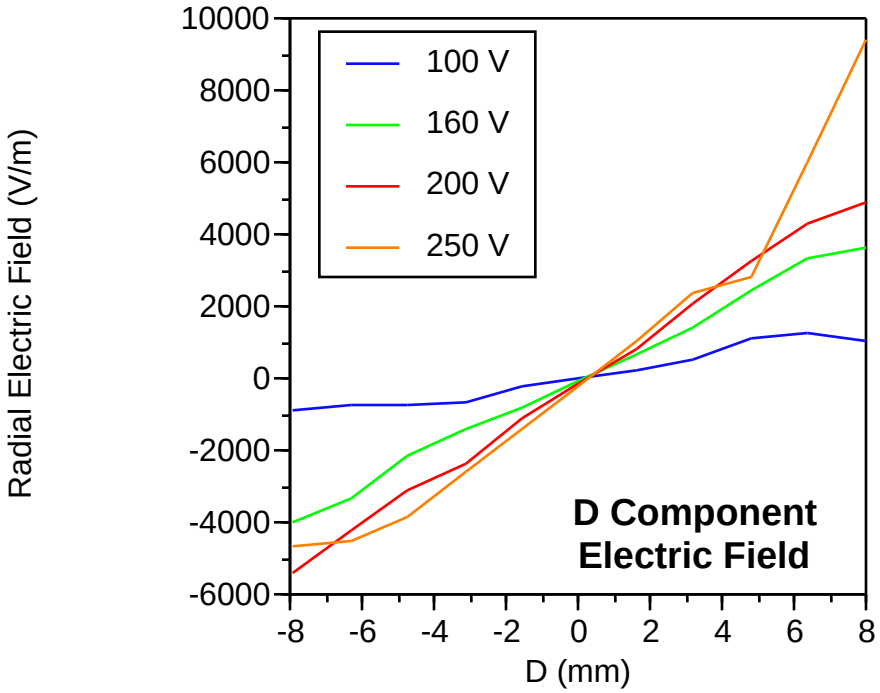

Figure 5.33. Radial component of plume electric field at Z = 13 mm for several discharge voltages.

electric fields in the near field plume of the Hall thruster. The values of which are on the order of the axial electric field derived from laser velocimetry. These large radial fields account for the degree of divergence of the plume.

5.2.5 Line Shape Modeling of the $5d[4]_{7/2} - 6p[3]_{5/2}$ Ionic Transition

The hyperfine splitting constants for the ionic xenon $5d[4]_{7/2} - 6p[3]_{5/2}$ transition at 834.7 nm are only known for the upper $6p[3]_{5/2}$ state. Similarly, the isotope shifts for this transition are unknown. In addition to the lack of spectroscopic information, the plasma introduces uncertainties to the determination of the ionic kinetic temperature from an unsaturated line shape. First, the population of ions under examination must be of a single velocity class. King has shown in energy analyzer data that the axial velocity of the exiting ions have an energy distribution of approximately 10 eV due to plasma oscillations within the Hall thruster. Second, the low density of the plasma may preclude a Maxwellian velocity distribution among the ions. If so, the concept of a kinetic temperature may not be valid.

The issue of the distribution of ionic velocities has been minimized by examining the fluorescence spectra in the radial direction. The radial spectra is taken from the location with the minimum bulk velocity measured, approximately 100 m/s at D = 0 mm and Z =

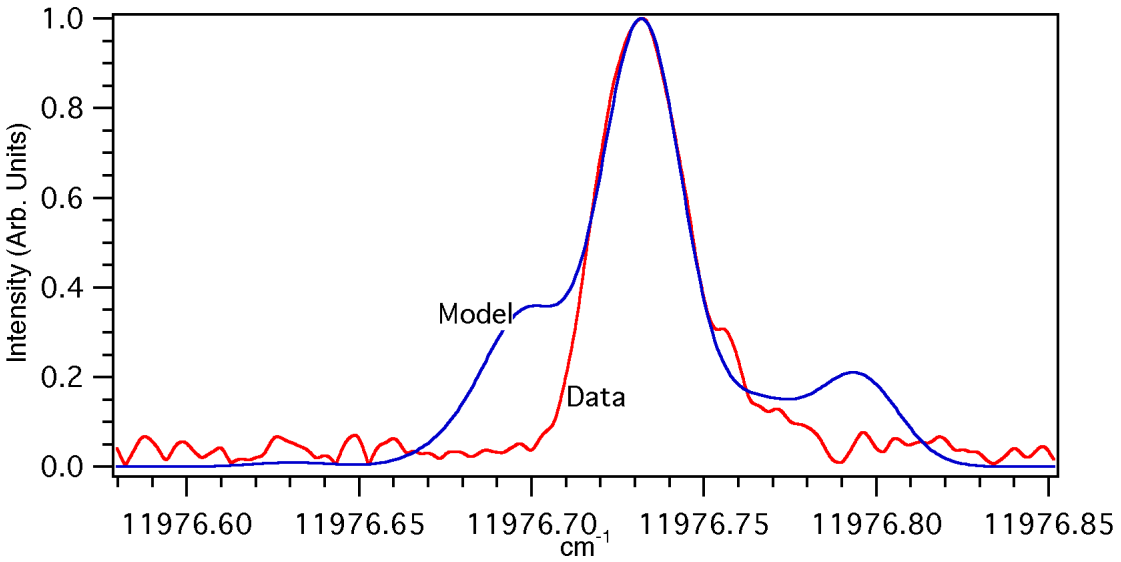

Figure 5.34. Unsaturated ionic line shape compared to model of 605.1 nm transition.

13 mm which is on the acceleration channel center and 13 mm into the plume from the exit plane. The ion population has been assumed to be Maxwellian, or at least frozen into a close approximation.

Despite the inherent limitations, an estimate of the kinetic temperature is still possible if uncertainties of 40-70% are acceptable (Cedolin 1999). Several cases are analyzed below. The first case is shown in Figure 5.34. Here, the model developed by Cedolin for the 605.1 nm ionic transition is used. Lorentzian broadening is neglected and only Doppler broadening is considered. As shown in Figure 5.34, the fit is only to the central peak of the line shape and results in an estimated kinetic temperature of 700 K. The 605.1 transition has hyperfine spin split components that are significantly more displaced from the line center than are the experimental data from the 834.7 transition. These features are primarily due to the 129 amu isotope of xenon and indicate that the A nuclear spin splitting constants of the lower and/or upper states are significantly different. Figure 5.35 shows the results of a similar model, but where the model uses the $5d[3]_{7/2}$ lower level hyperfine spin splitting data from the 605.1 nm transition and the measured splitting data for the upper $6p[3]_{5/2}$ level. It should be noted that the transition isotope shifts correspond to the values for the 605.1 nm transition. The best fit of this model predicts a kinetic temperature of approximately 450 K. As in the first case, the model still does not completely predict the outlying features, but this model is a significant improvement. In Figure 5.36, the unsaturated ionic line shape is compared to a model which ignores hyperfine splitting and accounts only for isotope shifts corresponding to the values for the 605.1 nm transition. The kinetic temperature indicated from this model is approximately 750 K. Neglecting all hyperfine splitting mechanisms, including isotopic and nuclear spin splitting, an absolute maximum temperature of 1,700 K may be implied from examining the Doppler halfwidth of the experimental line shape. This result implies that ions are formed within a small axial location of the acceleration channel, or over a range where the plasma potential does not vary significantly.

From the various models studied, it appears that the kinetic temperature is in the region of 450 to 750 K. The uncertainty of this measurement is in large part due to the uncertainties of the spectral data as well as due to the noise in the fluorescence signal. A similar measurement in the plume of a SPT-100 by Manzella yielded a kinetic temperature

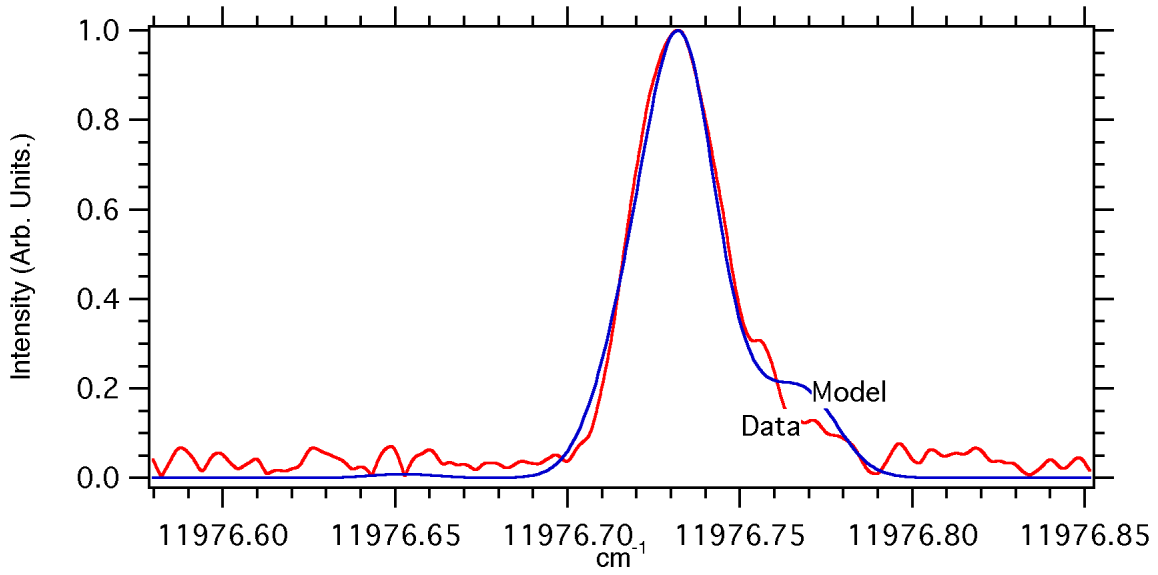

Figure 5.35. Unsaturated ionic line shape compared to a model using $5d[3]_{7/2}$ lower level hyperfine splitting data from the 605.1 nm transition and the correct hyperfine splitting data for the upper $6p[3]_{5/2}$ level. Note that the transition isotope shifts correspond to the values for the 605.1 nm transition.

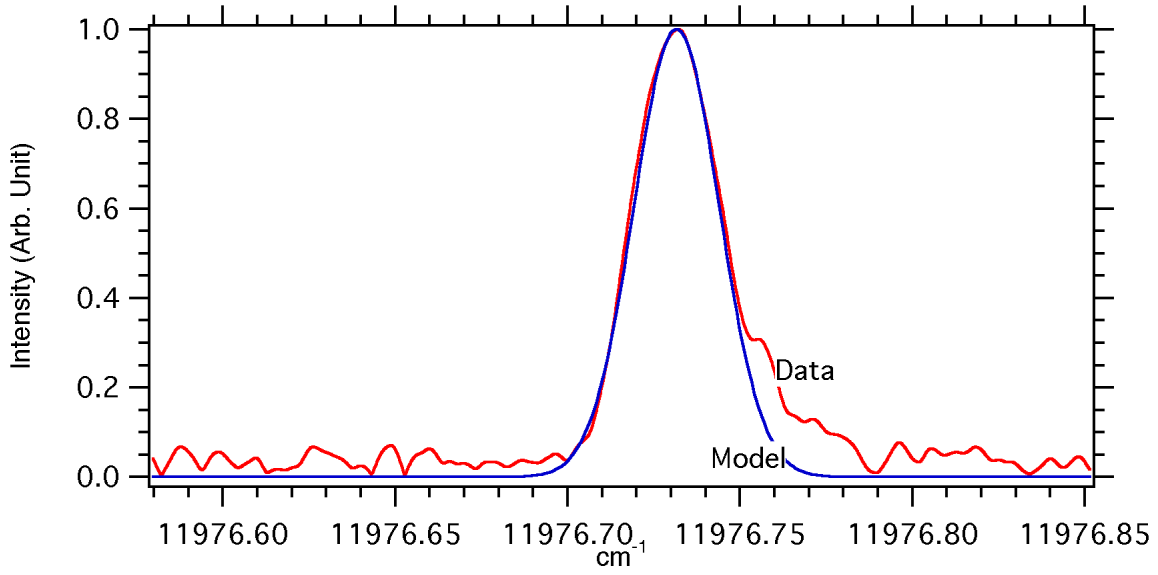

Figure 5.36. Unsaturated ionic line shape compared to a model which ignores hyperfine splitting and accounts only for isotope shifts. Note that the transition isotope shifts correspond to the values for the 605.1 nm transition.

on the order of 800 K. It should be noted that Manzella used the incorrect value of J for the lower state that was first misidentified by Humphreys and propagated by Moore. This may account for the slightly higher kinetic temperature; although, the uncertainty is such that the differences in the temperatures is inconsequential.

5.3 Laser Induced Fluorescence Velocimetry of the Xenon Neutral

5.3.1 Saturation Study

In order to measure the spatially resolved velocity field of the xenon neutrals in a Hall thruster plasma discharge, the $6s[3/2]_2^0 - 6p[3/2]_2$ neutral xenon transition was probed to extract local velocity data from the Doppler shift of the measured fluorescence. Figure 5.37 shows the curve of the peak saturation at a location 3 mm beyond the exit plane and at the center of the acceleration channel (Z = 3 mm, D = 0 mm) for a number of probe laser intensities. Here, the laser beam is propagating parallel to the thrust vector and is measuring the neutral xenon axial velocity. A typical partially saturated fluorescence trace used to determine the velocity in the probed volume is compared to an absorption reference trace

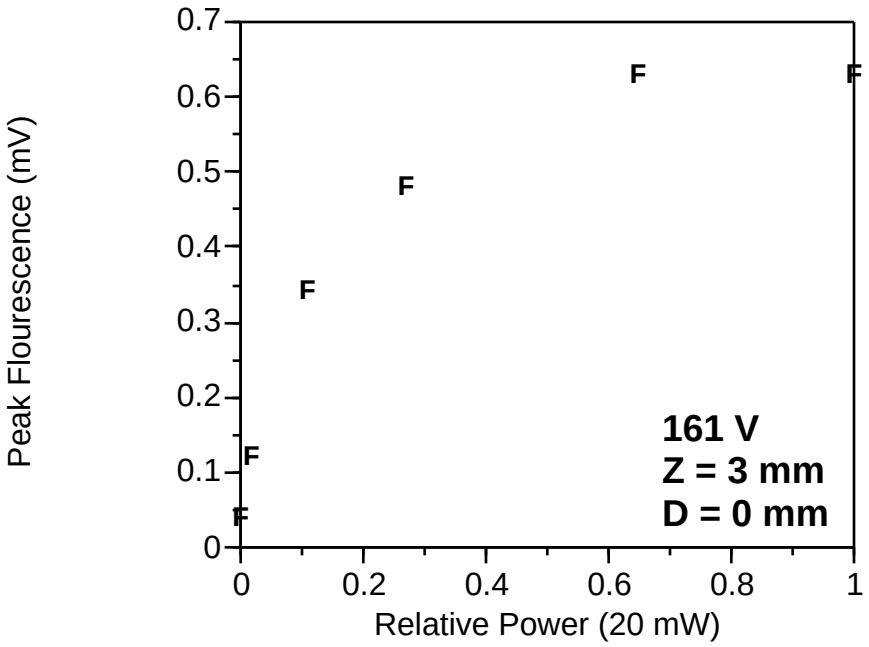

Figure 5.37. Saturation curve for the neutral xenon $6s[3/2]_2^0 - 6p[3/2]_2$ transition.

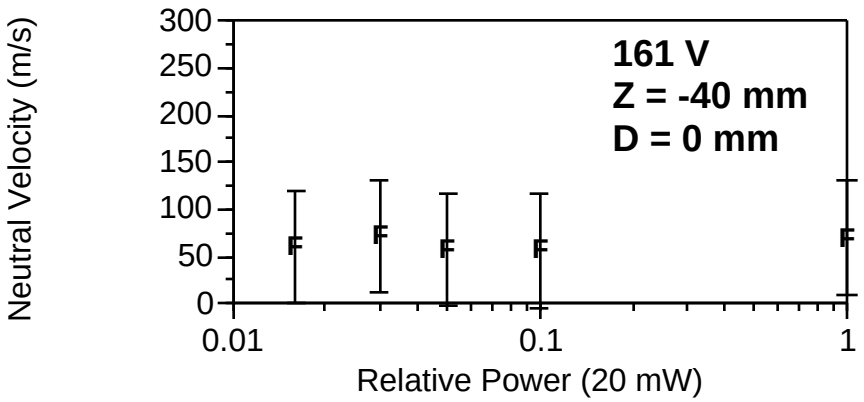

Figure 5.39. Neutral xenon velocity measurements at a variety of partially saturated conditions

from the glow discharge tube in Figure 5.38. Both traces are normalized to unity peak signal.

Velocities determined from the Doppler shift of the partially saturated line shapes are shown in Figure 5.39. The mean velocity is 63 m/s with a standard deviation of less than 10 m/s and a range of 20 m/s where the Doppler shift between the stationary reference and the collected fluorescence is determined by numerical cross correlation. The uncertainty of the measurements is estimated to be ±60 m/s. These results indicate that useful LIF velocimetry measurements may be performed on the partially saturated $6s[3/2]_2^0 - 6p[3/2]_2$ neutral transition of xenon. This allows for the collection of partially saturated fluorescence signals, maximizing the signal to noise ratio and allowing for faster scans to be taken of the transition while still extracting velocity data from the fluorescence signals.

5.3.2 Measurements of the Axial Neutral Velocity

Figures 5.40 to 5.43 show neutral velocities measured within the acceleration channel of the Hall thruster. All four test cases show similar behavior. The initial velocity near the anode is very low. The neutral velocity slowly rises until approximately 20 mm before the exit plane. At this point where the ion acceleration begins, the neutrals are accelerated at a high rate until near the exit plane where the acceleration appears to slow and in some cases even reverse when the thruster is operated at discharge voltages above 200 V.

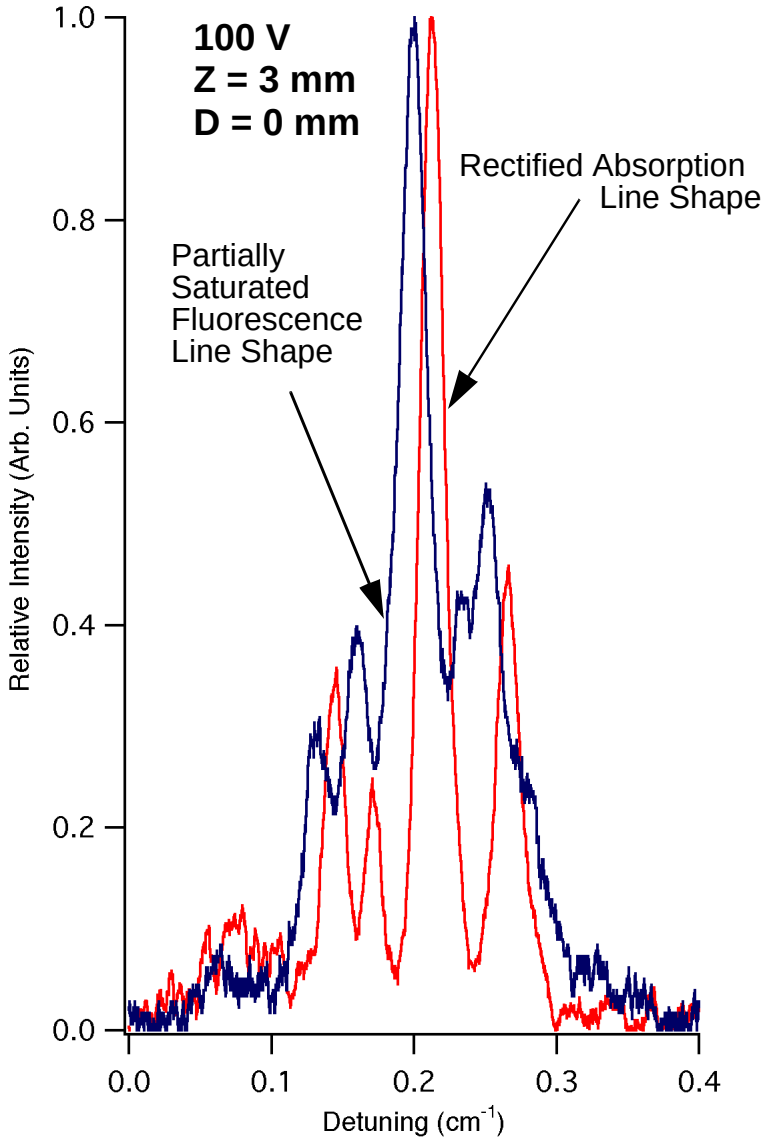

Figure 5.38. Partially saturated fluorescence line shape of the neutral xenon $6s[3/2]_2^0 - 6p[3/2]_2$ transition compared to a stationary reference absorption line shape.

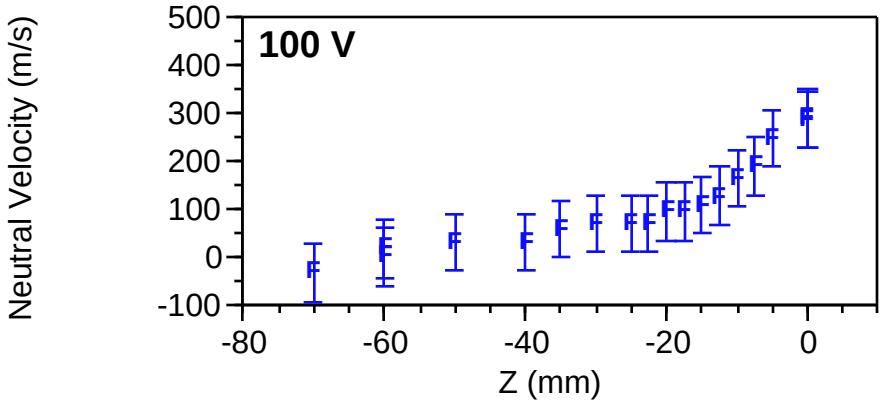

Figure 5.40. Axial velocity profile for 100 V discharge voltage case at D = 0 mm.

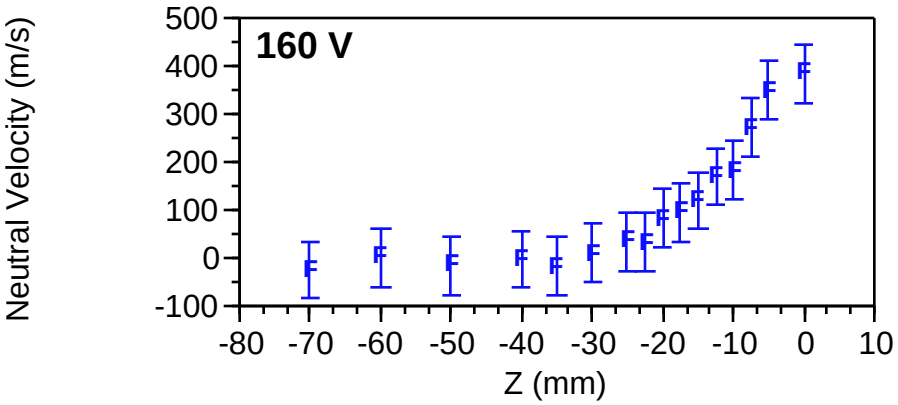

Figure 5.41. Axial velocity profile for 160 V discharge voltage case at D = 0 mm.

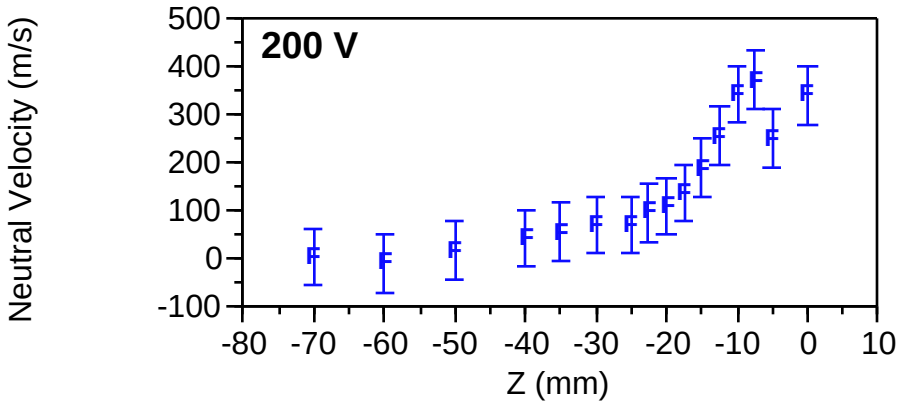

Figure 5.42. Axial velocity profile for 200 V discharge voltage case at D = 0 mm.

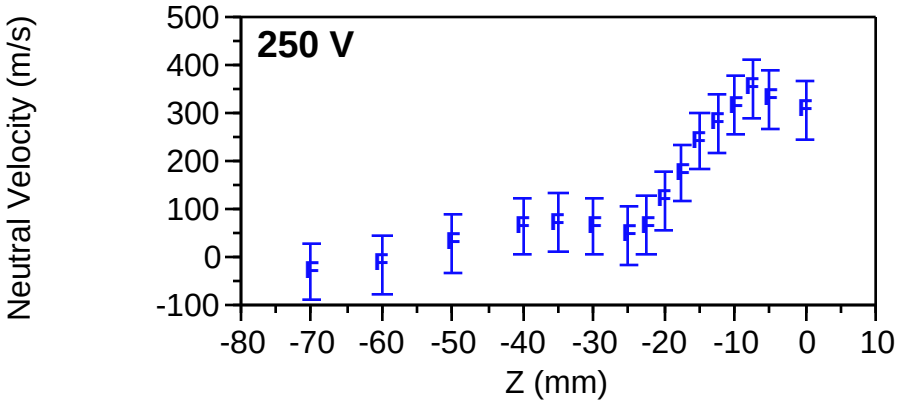

Figure 5.43. Axial velocity profile for 250 V discharge voltage case at D = 0 mm.

The decrease in the neutral velocity may be explained by thruster ingestion of background neutral xenon. Since the effect appears to grow with increased discharge voltage, it is possible that a portion of the exhaust reflected from nearby vacuum facility walls is ingested. Once the background xenon is in the vicinity of the discharge, the high electron density near the exit plane collisionally excite the background atoms. Some of these atoms are ionized and the external electric fields produced by the thruster accelerate the resulting ions downstream, albeit with lower final energies than ions created within the thruster. Some of the atoms will be electronically excited, but not be ionized and will optically decay to the $6s[3/2]_2^0$ metastable level where they could be sampled during LIF velocimetry measurements.

Closer to the anode, the data implies that the neutrals may be moving toward the anode, although it is within the uncertainty of the measurement. It should be noted that the neutral velocities measured are actually the velocities of a particular excited state and may not necessarily be completely representative of the bulk flow. The $6s[3/2]_2^0$ excited state is metastable with a measured lifetime of 42 s. Only collisions with walls, or with other particles, will cause the atom to decay from the $6s[3/2]_2^0$ state to a lower energy state. It is not completely clear where these atoms in the $6s[3/2]_2^0$ state originate, nor is it clear how atoms near the anode are excited into the higher electronic states. It is likely that most of the highly excited neutrals are the product of three body recombinations. Ion collisions with the walls of acceleration channel can be ruled out since the resultant atom is always fully

accommodated on all but the most specially prepared surfaces. Due to the finite electron current, a number of ions must reach the anode in order to ensure universal charge neutrality of the plasma. Three processes may then explain the apparent backward motion of the excited state atoms. Charge exchange between forward flowing neutrals and back flowing ions may result in the creation of some excited state neutrals flowing toward the anode. Unfortunately, little information exists for xenon resonance charge exchange collision cross-sections, especially at low energies. Three body collisions resulting in the recombination of an ion and an electron with excess energy transferred to a third particle could also be the source of these backward flowing excited state neutrals; however, it is unlikely that neutrals created in this way would retain memories of their flow history. Alternatively, atoms excited within the ionization region may diffuse back toward the anode and in the absence of collisions may reach the rear portions of the acceleration channel. The lifetime of the state is sufficiently long and collisions with other particles in the acceleration channel are sufficiently rare for a number of these excited state atoms to reach the near anode region of the acceleration channel. This last mechanism is considered to be the most probable since it has no reliance on collisions and is consistent with the physics governing the $6s[3/2]_2^0$ energy level.

Figure 5.44 shows several radial profiles of the neutral axial velocity for a discharge voltage of 200 V. The measurements at two axial positions show near uniform velocities across the radial coordinate D. The axial position Z = -10 mm is the location where the acceleration of the ions first occurs where a substantial portion of the neutrals have already been ionized. The second location at Z = -50 mm is far upstream from significant fields and high ionization fractions. At this location, the measured neutral velocity is negative although the uncertainties overlap with positive velocities. In both cases, the radial profiles of the axial velocities are flat and uniform to within the uncertainty of the measurement similar to measurements of ion velocities.

No measurements of neutral velocities exterior to the Hall thruster are presented. Initial external measurements indicated substantial entrainment of background neutrals occurred making velocity measurements ambiguous at best and misleading as to the actual neutral velocities. The velocity data is difficult to extract from the increased background emission in the plume. Emission from the $6s[3/2]_2^0 - 6p[3/2]_2$ transition is the strongest

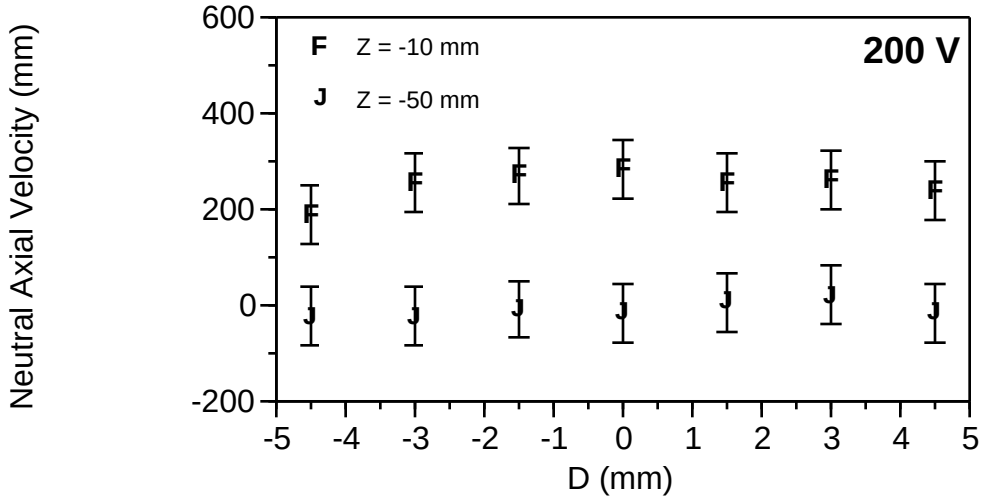

Figure 5.44. Radial profiles of the axial neutral velocity within the acceleration channel.

feature in the spectrum of xenon. In addition, as the discharge voltage is raised, the neutral xenon fluorescence signal lessens significantly with increased ionization fraction.

5.3.3 Neutral Xenon Acceleration Mechanisms

Several mechanisms could be responsible for the characteristics of the neutral axial velocity traces in Figures 5.40 to 5.43, one of which is charge exchange. Charge exchange is a process by which an electron is transferred to a fast moving ion from a slow moving neutral resulting in a fast moving neutral and slow moving ion. In these collision events, it is as if the identity of the colliders is reversed. Cross-sections for low energy (<100 eV) resonant charge exchange colliders have been measured to be on the order of momentum transfer collision cross-sections and increase substantially at lower energies when the colliders are in proximity for a longer period of time. What is essentially an electron tunneling event, therefore, has a higher probability under these conditions. Since neutrals with velocities approaching those of the ions are not evident, it is unlikely that this mechanism is responsible for the apparent acceleration of the neutrals.

Anode heating and propellant gas expansion can be ruled out as the mechanism by which the neutrals are accelerated. Figure 5.45 shows the speed of sound for xenon assuming a perfect gas. If it is assumed that heating of the surfaces of a acceleration channel, or anode, and the subsequent expansion of the xenon propellant through the acceleration

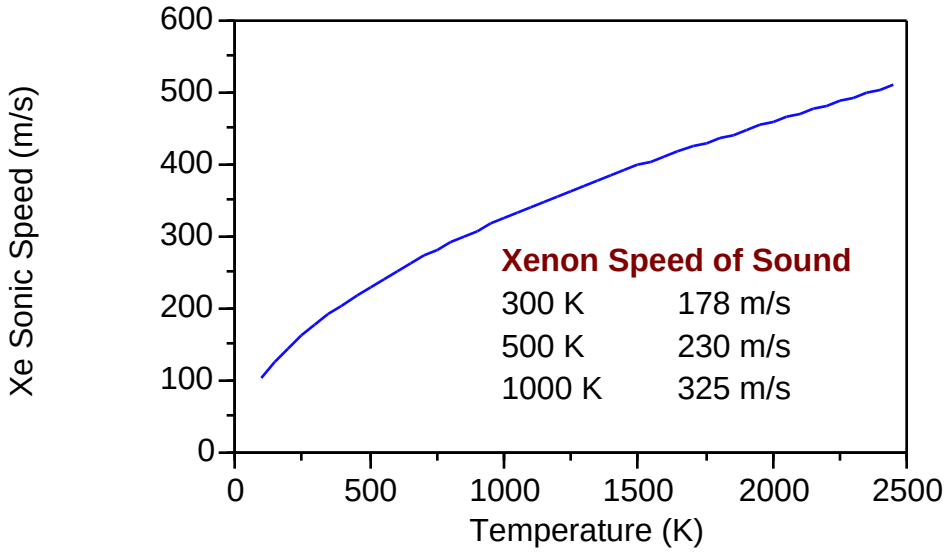

Figure 5.45. Xenon sound speed assuming a perfect gas.

channel accelerates it to sonic velocities, the surfaces would have to be at temperatures approaching 1500 K. These temperatures could not be sustained on the Hall thruster as tested. The temperature of the body measured by attached thermocouples never exceeded 500 K. It is unlikely that the anode which is separated from the thruster body by a 6 mm thickness of alumina would reach such an extreme temperature. It is therefore obvious that the acceleration of the neutrals is not a simple gas expansion process.

The plasma within the Hall thruster must be very diffuse so that the magnetic field effectively restrains the electron flux to the anode. This requirement is in force when the neutral velocity measurements of Figures 5.40 to 5.43 are compared with the ionic velocity measurements presented in Figures 5.12 to 5.15. The disparate velocities of the ions and neutrals indicate that the neutral and ion populations are decoupled. As such, the apparent acceleration of the neutrals may actually be an artifact of the neutrals time of flight through the ionization zone. Slower neutrals, or neutrals that travel a longer effective path length due to collisions with the walls of the acceleration channel, have a proportionally greater chance being ionized than do neutrals in the high energy portion of the velocity distribution. Therefore, atoms from the high energy portion of the velocity distribution have a higher probability of reaching the downstream portion of the acceleration channel. As such,

there is no actual acceleration of the neutrals, but rather a preferential depletion of the slower moving atoms by ionization.

The depletion of the slower neutral velocity classes accounting for the apparent acceleration of the neutrals as seen in Fig. 14 can be shown by starting with the one dimensional Boltzmann equation [Vincenti and Kruger].

$$\frac{\partial}{\partial t}[nf(u)] + u\frac{\partial}{\partial z}([nf(u)] + \frac{\partial}{\partial u}[Gnf(u)]) = \left(\frac{\partial}{\partial t}[nf(u)]\right)_{coll} \qquad (1)$$

Where n is the neutral number density, u is the neutral velocity class, z is the spatial coordinate, $f(u)$ is the velocity distribution function, t is temporal coordinate, and G represents body forces acting on the neutrals. Equation 1 may be simplified by assuming the process is steady, there are no external or body forces acting on the neutrals, and that the sole depletion mechanism for the neutral velocity classes is electron collisional ionization. Implicit in this set of assumptions is that the ions and neutrals do not interact in a significant manner.

$$u\frac{\partial}{\partial z}[nf(u)] = -[nf(u)]n_e S^* \qquad (2)$$

Where n_e is the local plasma electron number density and S^* is the ionization rate coefficient. Equation 19 may be integrated with respect to $nf(u)$ if several limiting assumptions are made. If the ionization rate coefficient S^* and the electron number density n_e are assumed to be constant, the population of the u velocity class, $nf(u)$, exponentially decays with the spatial variable z moderated by the value of u.

$$nf(u) \quad e^{-z/c} \qquad (3)$$

This analysis of the one dimensional Boltzmann equation shows that the neutral density in a model plasma is depleted along the Z axis due to neutral-electron collisional

ionization, and more importantly, that the relative depletion depends on the velocity class. Neutrals which are members of the lower velocity classes are more likely to be ionized when passing through the ionization zone than neutrals which belong a higher velocity class. Therefore, the apparent acceleration of the neutrals is the result of the depletion of the slower moving neutrals rather than an acceleration process.

Since the probability of a neutral being ionized in the volumetric ionization zone is dependent on the residence time, increased Hall thruster efficiency is realized by slowing the neutrals. In short channel thrusters, anode gas distribution is usually indirect so that the neutral propellant exits subsonically. For longer channel thrusters, the geometry of the anode propellant feed system is less important since the neutrals will most likely collide with the walls several times prior to exiting the thruster. Each collision will result in a diffuse reflection in which the atom will lose all memory of its previous velocity history, effectively slowing down the overall speed of the exiting neutrals. This was one of the factors leading to the lengthening of the channel in the modified Hall thruster design.

5.4 Emissive Probe Measurements

5.4.1 Initial Measurements and Evolution of Probe Design

The first probe constructed to measure plasma potential consists of a coiled thoriated filament strung between two tantalum lead wires each individually sheathed in a 1.3 mm diameter alumina tube described in greater depth in Chapter 3. This probe is adequate for measurements in the plume and into the thruster interior of only the lowest discharge voltage examined (100 V). The measurements for this first probe configuration are shown in Figure 5.46. The measured plasma potential rises from a low constant value in the plume (Z ~ 50 mm) to values approaching the discharge voltage near the anode.

Also shown in Figure 5.46 is the plasma potential measured by a second, more robust probe. This probe is similar to the first probe, but the two tantalum lead wires are sheathed in a single 6 mm multibore mullite tube. This probe presents a larger perturbation to the plasma and blocks approximately 50% of the acceleration channel width. It was the only probe constructed that could withstand entrance into the acceleration channel at discharge voltages above 100 V. Failure of the initial design generally consisted of melted lead

wires, or where the sheath had become heated to an extent such that it would sag, losing the probe position. The alumina sheath is also vulnerable to thermal shock and would on occasion fail due to strong localized heating. The mullite sheath of the second probe design also heated substantially to the extent that the ceramic glowed incandescently; however, the probe sheath never failed, nor was any sagging evidenced. One difficulty with the more robust probe is that the leads of the filaments could not be completely insulated to the filament. Therefore, a portion of the lead wires is in contact with the plasma. This may explain the differences between the two potential curves shown in Figure 5.46. The more robust probe averages its measurement over a slightly larger length behind the filament and produces a slightly lower plasma potential measurement than the better insulated, but more fragile, probe. In addition, the second probe due to its large size may perturb the plasma within the thruster more than the initial design. The current-voltage characteristics of the thruster were monitored during the acquisition of both data sets in Figure 5.46 and no change was seen. At higher discharge voltages, introduction of the plasma potential probe into the acceleration channel increases the discharge current substantially. This effect

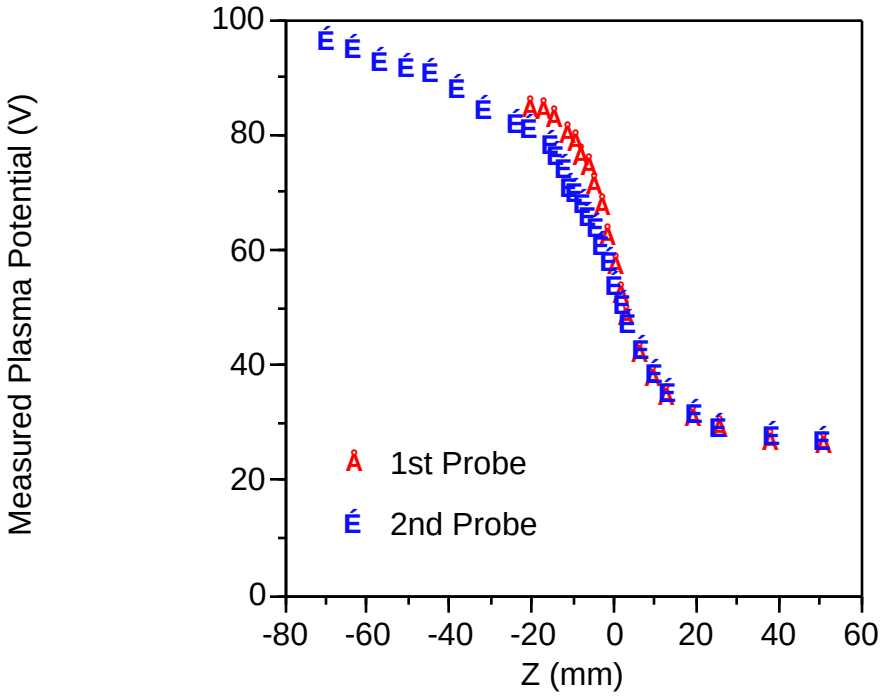

Figure 5.46. Comparison of plasma potential measurements by the first and second emissive probes. The anode voltage for this case is 100 V.

increases with discharge voltage setting from 100 V where the discharge current is steady, up to 200 V where the discharge current increases to 140% of its nominal value.

5.4.2 Plasma Potential Measurements and Electron Temperatures from the Bohm Criterion

Figures 5.47 to 5.50 show the measured plasma potential and electron temperature estimated using the Bohm criterion for the four anode discharge voltages examined. In each plot, the data was taken with the more robust probe due to its ability to successfully withstand the harsh environment within the acceleration channel. Each plot shows similar behavior. The potential is constant in the far plume with a value of approximately 25 V, likely corresponding to the potential of the electrons produced by the hollow cathode neutralizer. As the probe is traversed into the acceleration channel, the potential rises significantly as the impedance of the radial magnetic field to the axial electron current is encountered near the exit plane. The plasma potential rapidly rises and by Z = -20 mm has reached 80-90% of the anode potential. The remaining 10-20% of the potential is distributed between this position and the anode and does not appear to contribute to the propellant acceleration. Figure 5.50 is incomplete due to several successive failures of the probe where the tantalum leads melted and the thoriated tungsten filament lost electrical contact with one, or both, of the leads. Coating of the exposed tantalum leads with high temperature ceramics proved impractical due to the thermal expansion of the leads during heating of the

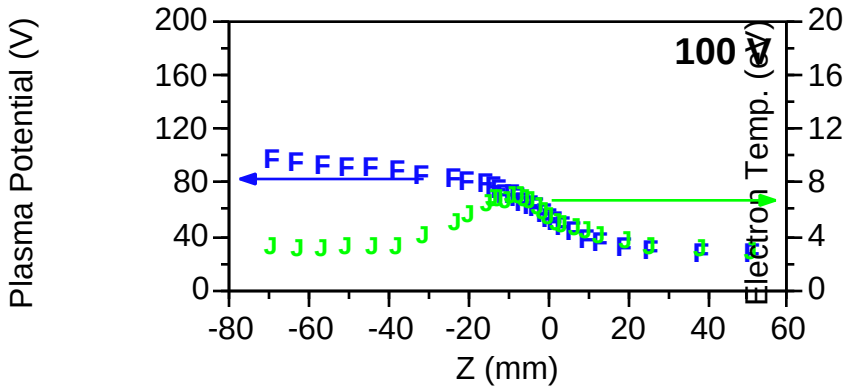

Figure 5.47. Axial profile of measured plasma potential and estimated electron temperature for a discharge voltage of 100 V at D = 0 mm.

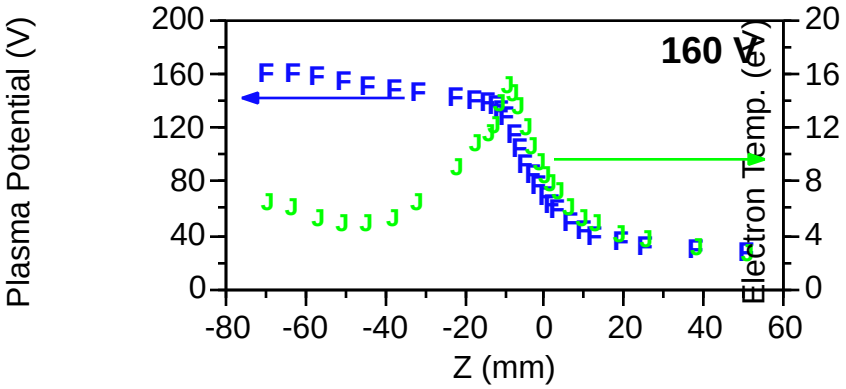

Figure 5.48. Axial profile of measured plasma potential and estimated electron temperature for a discharge voltage of 160 V at D = 0 mm.

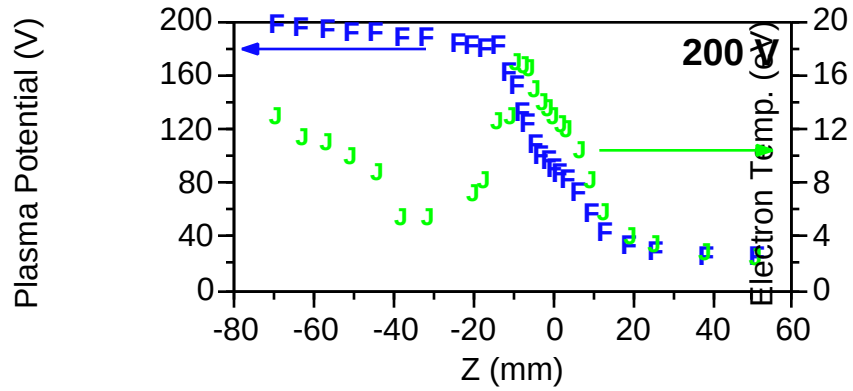

Figure 5.49. Axial profile of measured plasma potential and estimated electron temperature for a discharge voltage of 200 V at D = 0 mm.

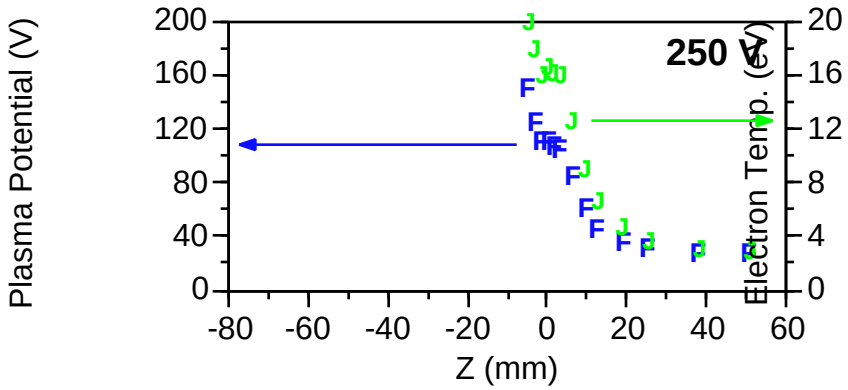

Figure 5.50. Axial profile of measured plasma potential and estimated electron temperature for a discharge voltage of 250 V at D = 0 mm.

probe which caused the coating to flake off. No measurements further into the acceleration channel could be performed for a discharge voltage of 250 V.

The electron temperatures computed from the difference between the floating and plasma potentials using the Bohm criterion are also shown in Figures 5.47 to 5.50. The general trend is a low electron temperature (2.5-3 eV) in the plume which rises with the plasma potential to a maximum located between 8 and 10 mm within the thruster which corresponds to the location of the peak radial magnetic field and the location where the ion acceleration is first evident. The electron temperature then falls although the plasma potential is only at 80% of the anode potential. The rapid fall off of the electron temperature occurring between Z = -10 mm to Z = -40 mm is primarily due to a rapidly rising floating potential. Closer to anode (Z < -40 mm), the electron temperature again begins to rise. Here, the plasma potential is only rising slowly, but the floating potential is dropping, and the electron temperature rises. This effect grows significantly more pronounced with increased discharge voltage. For example at a discharge voltage of 100 V, an electron temperature rise near the anode is nearly imperceptible. At 160 V, the rise in electron temperature is well defined, and at 200 V, the electron temperature near the anode approaches the peak temperatures of the exit plane.

Similar behavior has been seen in the literature (Morozov et al. 1972). In that study, the two dimensional potential field of a Hall thruster of similar geometrical dimensions operating on argon at a discharge voltage of 400 V was measured. Strong variation in the radial plasma potential was found in the 30 mm nearest to the anode within a 138 mm long acceleration channel. Similar measurements could not be performed on the Stanford Hall thruster due to geometrical constraints, but a similar potential field is implied in this case since a potential field distribution similar to that observed by Morozov et al. would produce radial electric fields which would heat local electrons to elevated temperatures as seen in Figures 5.48 and 5.49.

Radial profiles of the plasma potential and derived electron temperature at Z = 13 mm are shown in Figures 5.51 to 5.54. The radial plasma potential traces show a portion of the structure within the near field plume. The annular ion beam has diffused significantly by this axial location, yet retains a distinct structure. The asymmetry of the traces also shows the development of the central core feature. The asymmetry manifests itself at low discharge

voltages where the plasma potential near the central magnetic core remains at a higher value than it does toward lesser values of D. This phenomena is not as evident at higher discharge voltages; however, the absolute magnitude of the potentials within the core and in the outer portion of the plume retain a difference of nearly 10 V in all cases. Less mixing occurs as the ionized propellant stream has greater momentum with increased discharge voltage. This accounts for the extended plume structure seen at the higher discharge voltages. Since the plume structure is also more visible at lower pressures, a portion of the perceived diffusion may actually be entrained and subsequently ionized background xenon.

The electron temperatures calculated from the plasma potential measurements also exhibit the asymmetry of the plasma potential data, particularly at lower discharge voltages. However, the asymmetry is much less pronounced than for the plasma potential data. Otherwise, the electron temperature data follows the plasma potential profile.

Due to the physics inherent to the diagnostic, the emissive probe potential only approaches the plasma potential from below. The data has a repeatability of approximately ±3 V. The plots of apparent plasma potential to probe filament current previously shown in Chapter 4 asymptotically approach a limiting value indicating that the measurements are within several volts of the true plasma potential indicating an uncertainty associated with the plasma potential measurements of approximately -3/+6 V. The related uncertainty of the electron temperature may be calculated from the uncertainty associated with the measurement of the plasma potential and the floating potential. However, the use of Bohm criterion

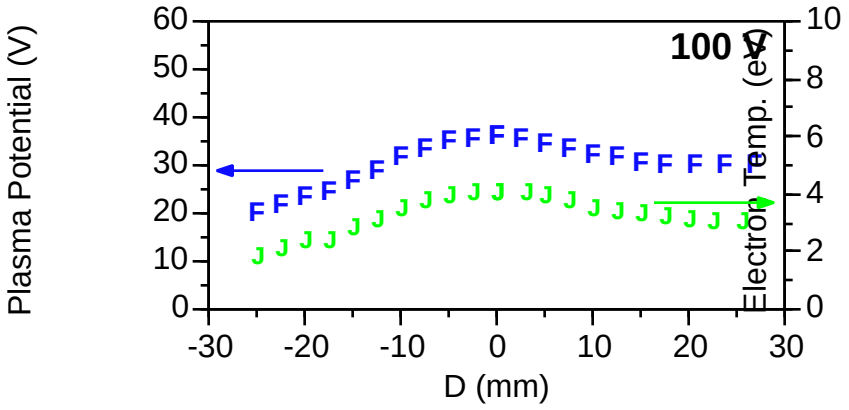

Figure 5.51. Radial profile of the plasma potential and electron temperature for a discharge voltage of 100 V at a Z = 13 mm.

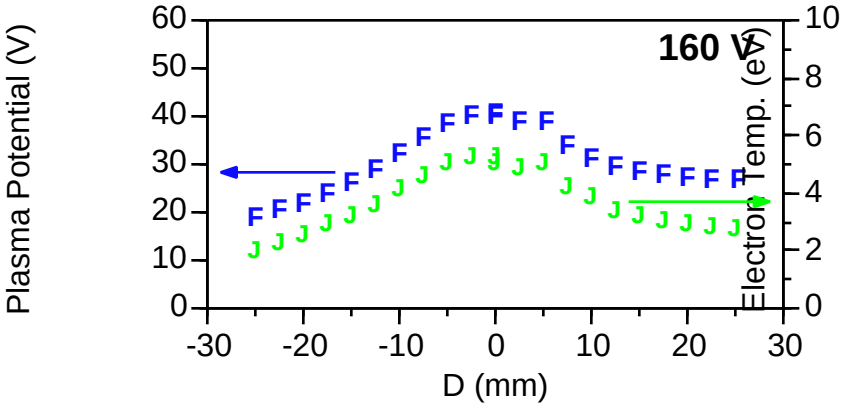

Figure 5.52. Radial profile of the plasma potential and electron temperature for a discharge voltage of 160 V at a Z = 13 mm.

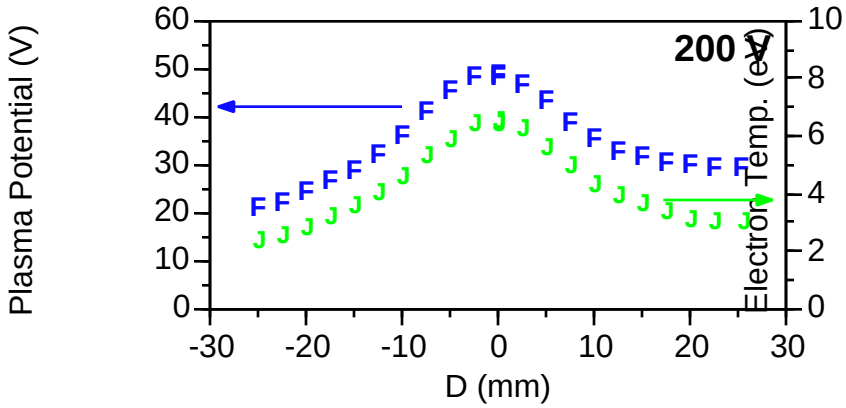

Figure 5.53. Radial profile of the plasma potential and electron temperature for a discharge voltage of 200 V at a Z = 13 mm.

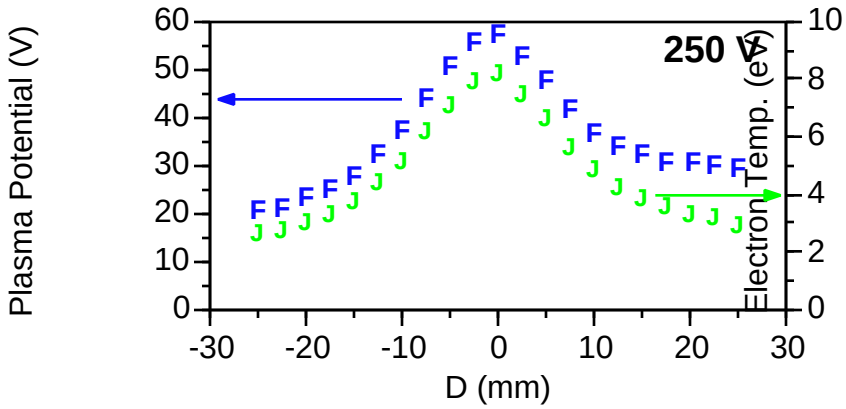

Figure 5.54. Radial profile of the plasma potential and electron temperature for a discharge voltage of 250 V at a Z = 13 mm.

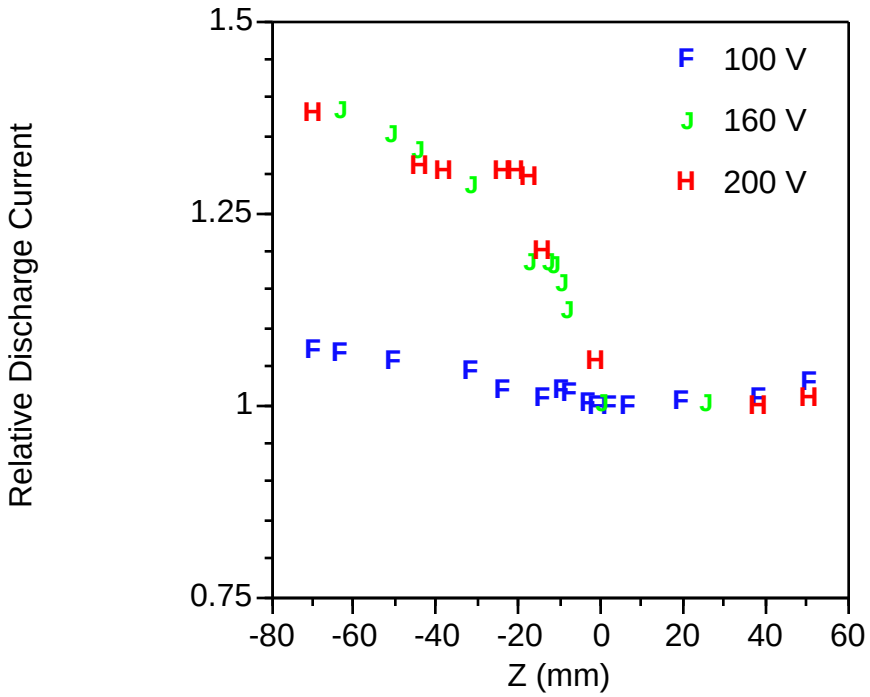

Figure 5.55. Perturbation of the discharge current due to potential probe position relative to thruster.

to determine the electron temperature does not warrant this effort except perhaps well within the Hall thruster where the ions are subsonic. The measurements of the electron temperature are repeatable to values significantly better than ±1 eV, but due to the use of the Bohm criterion to determine the ion flux to the probe surface, the only statement that can be maintained is that the values represent the lower bound of the actual electron temperatures.

Another issue that must be addressed is how much the plasma potential probe perturbs the plasma and affects Hall thruster operation. At 100 V, the lowest discharge voltage examined, the discharge current does not appreciably vary during insertion and removal of the probe. Universally, the thruster discharge current does not depend on whether the probe is heated, or remained cold. At higher discharge voltages, the discharge current is strongly affected by the position of the probe within the acceleration channel. Figure 5.55 shows the effect of probe position within the acceleration channel on the discharge current relative to the nominal discharge current. At the lowest discharge voltage case of 100 V, the probe does not significantly affect the thruster discharge current. With the probe fully inserted, the discharge current rises only 7% above the nominal value. The slight decrease

with the probe external to the thruster is attributed to the thruster approaching equilibrium conditions after start-up. The effect of the probe at higher discharge voltages is significantly different. In these cases, the probe has a strong impact on thruster operation. When the probe tip is traversing the initial 20 mm into the acceleration channel, the discharge current rises to nearly 130% of the nominal value. Inserting the probe significantly further into the thruster only raises the potential an additional 10%. Clearly, the probe is perturbing the discharge in the first 20 mm where it has been determined by LIF velocimetry where the acceleration of the ions begins. It is notable that the effect of the probe is so different between the discharge voltages of 100 V and 160 V, and yet so similar for the 160V and 200 V cases. This strongly reinforces the notion that the 100 V case differs significantly from all others.

5.4.3 Electric Fields from Plasma Potential Measurements

The plasma potential data in Figures 5.47 to 5.50 are differentiated to produce axial electric field data for the centerline of the acceleration channel shown in Figures 5.56 to 5.59. Also shown in these figures are axial electric field data calculated from ion LIF velocimetry measurements. This is possible since the acceleration mechanism within a Hall thruster is electrostatic. There are differences between the two measurement sets. LIF velocimetry is nonintrusive, or at least less intrusive with the addition of the slot in the insulator. The propellant ionization occurs in specific regions of high electric field which may mask the detection of local electric fields using velocimetry data, especially if the region of ion creation is sufficiently large such that ion creation and acceleration regions overlap. The uncertainties associated with the ionic velocity measurements are also magnified by the numerical derivation of potential and subsequent electric field data. With the plasma potential probe, the issue is the degree to which the probe disturbs the plasma. Figure 5.55 shows how much the thruster as a whole is disturbed by the presence of the probe, but does not indicate how much the plasma is modified locally.

The LIF and probe based measurements in Figures 5.56 through 5.59 show similar trends. Some of the features are different, particularly those more than 10 mm within the Hall thruster exit plane. Between Z = -10 mm and the anode, there exists only a small population of ions with low axial velocities. Velocimetry studies are inadequate to study the potential and electric field in this region, but potential probe measurements, assuming that

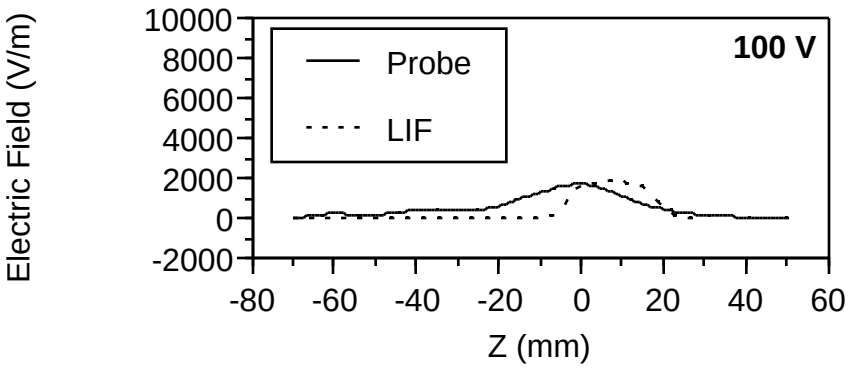

Figure 5.56. Probe derived axial electric field profiles for a discharge voltage of 100 V.

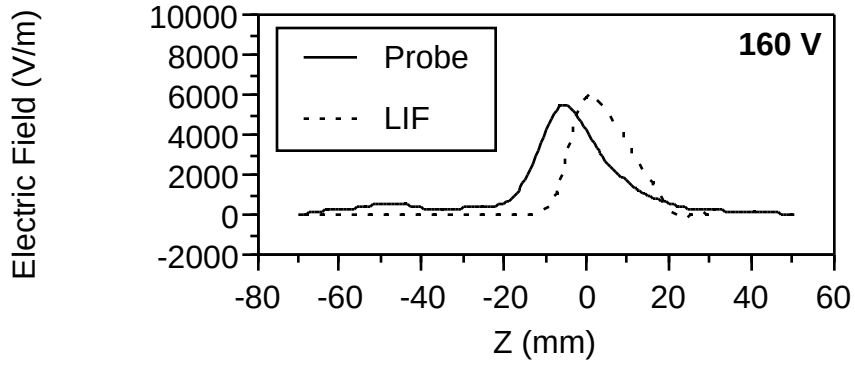

Figure 5.57. Probe derived axial electric field profiles for a discharge voltage of 160 V.

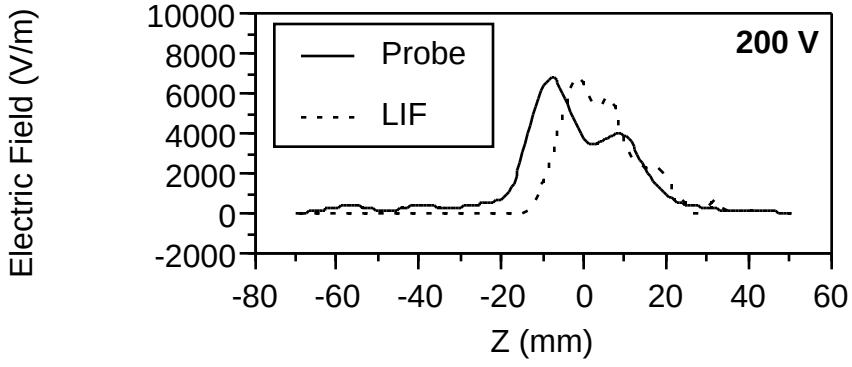

Figure 5.58. Probe derived axial electric field profiles for a discharge voltage of 200 V.

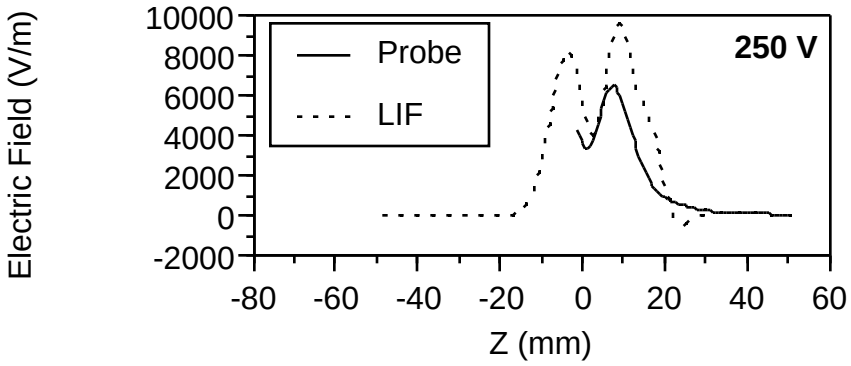

Figure 5.59. Probe derived axial electric field profiles for a discharge voltage of 250 V.

they do not significantly perturb thruster operation, provide better measurement of the plasma potential and subsequently a better indication of the electric field. It is believed that the probe, particularly the more robust version used for the majority of the plasma potential probes, under measures the higher gradients of the plasma potential due to the probe body perturbing the plasma flow field. This would explain the why the electric fields measured by the probe are generally less than those determined from velocimetry studies.

Figures 5.60 through 5.63 show the radial electric fields calculated from the plasma potential measurements presented in Figures 5.51 through 5.54. Each of these figures represents the radial component of the electric field across the acceleration channel at a location of Z = 13 mm. The magnitude of the electric field peaks at relatively large values in each case and shows the electrostatic forces focusing/defocusing the plume. The radial elec-

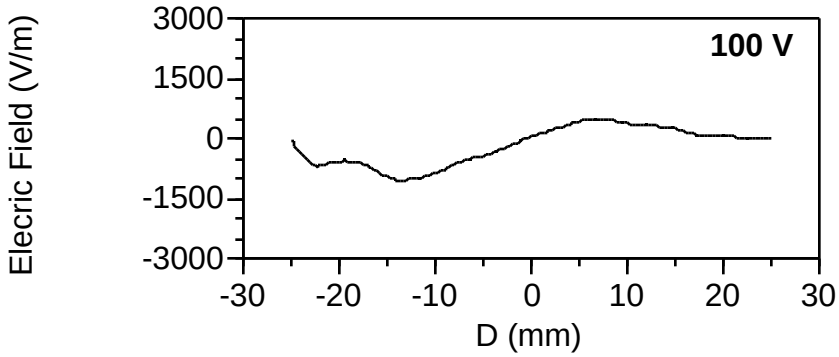

Figure 5.60. Radial electric field for a discharge voltage of 100 V at a axial location 13 mm downstream of the exit plane.

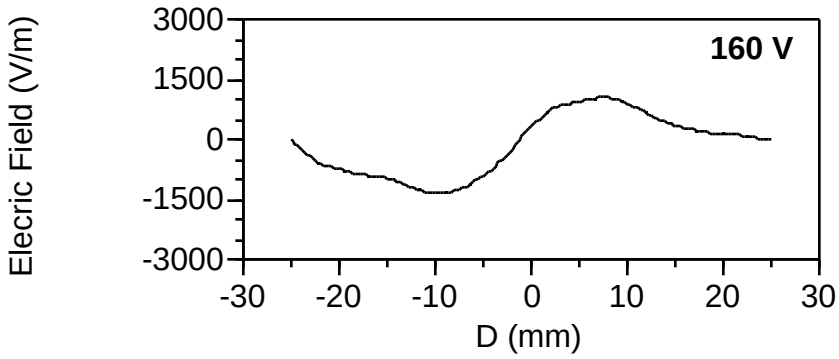

Figure 5.61. Radial electric field for a discharge voltage of 160 V at a axial location 13 mm downstream of the exit plane.

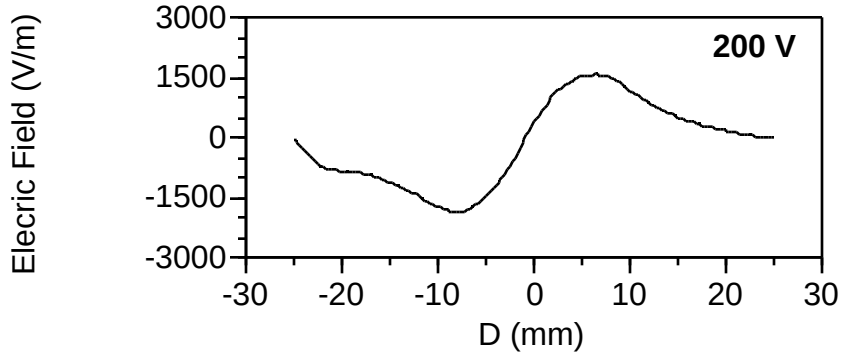

Figure 5.62. Radial electric field for a discharge voltage of 200 V at a axial location 13 mm downstream of the exit plane.

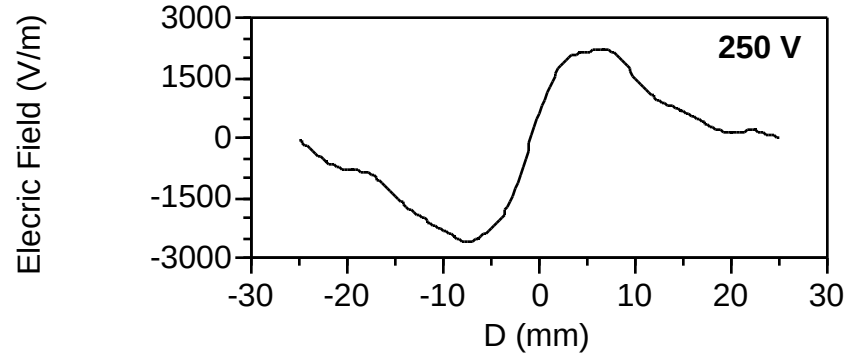

Figure 5.63. Radial electric field for a discharge voltage of 250 V at a axial location 13 mm downstream of the exit plane.

tric field peak increases with discharge voltage from a value near 1,000 V/m at 100 V to approximately 2,500 V/m at a discharge voltage of 250 V. The peak value of the radial component of the electric field at this location in the plume is approximately equal to the axial component at this location.

The variation of the radial electric field is similar to that seen in the axial component of the magnetic field. The impedance of the plasma, whether either classical or enhanced electron diffusion holds, is a function of the magnetic field strength as well as a vector quantity. Figures 5.64 and 5.65 show the radial and axial components of the magnetic field at an axial position 2 mm from the exit plane. Figure 5.64 is a vector plot of the field lines, while Figure 5.65 shows the magnitude of the radial and axial components of the magnetic field. The variation of the axial portion of the magnetic field is of most interest. At this position in the plume, the radial electric field is nearly proportional to the axial magnetic field. A density effect may be implied the discharge voltage. As the discharge voltage is increased, the velocity of the ion propellant stream rises and the plasma density falls. Along with the fall in plasma density, the conductivity falls and the radial electric field increases as evidenced by the data in Figures 5.60 through 5.63.

The magnetic field in Figures 5.64 and 5.65 may also explain another observed phenomena. The front surface of the thruster is coated with a layer of boron nitride. This coating has a nitrocellulose binder which carbonizes if exposed to excessive heating. After each thruster operation greater than several hours, the boron nitride coating over the central pole piece is discolored. The thin black layer could be brushed off to reveal the remainder of the coating to be intact. The magnetic field lines at the central core are normal to the surface. Low energy electrons in this region are constrained along these field lines normal to the surface of the central magnetic core and may eventually impact on the surface. The nature of the discoloration indicates that the heating is not from the thruster body, but from the plasma. Thermocouples attached to the thruster body measured maximum temperatures on the order of 500 K. Therefore, the carbonization of the boron nitride coating is believed to be due electron heating of the coating surface. Ion bombardment can probably be discounted in this process. The ionic Larmor radius is too large to effectively guide the ions to the central core and the potential field in the plume would draw the ions away from the electrically isolated thruster body. The strength and direction of the magnetic field lines shown in Figures

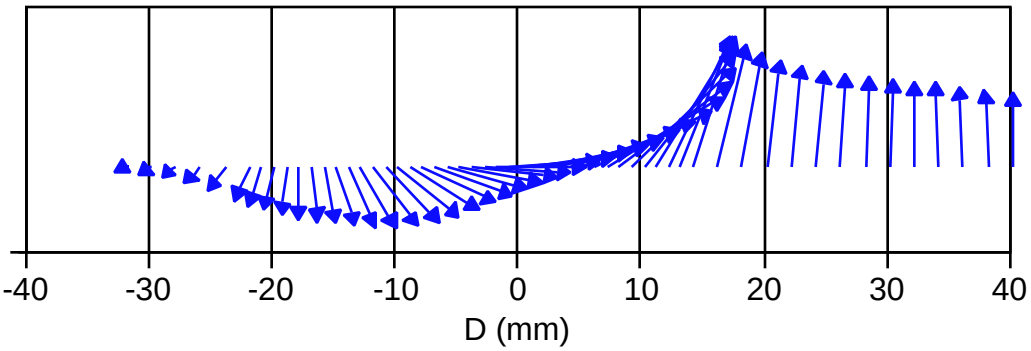

Figure 5.64. Magnetic field lines across the front of the thruster at an axial position of Z = 2 mm. Note that the center of the thruster body is at approximately D = 40 mm.

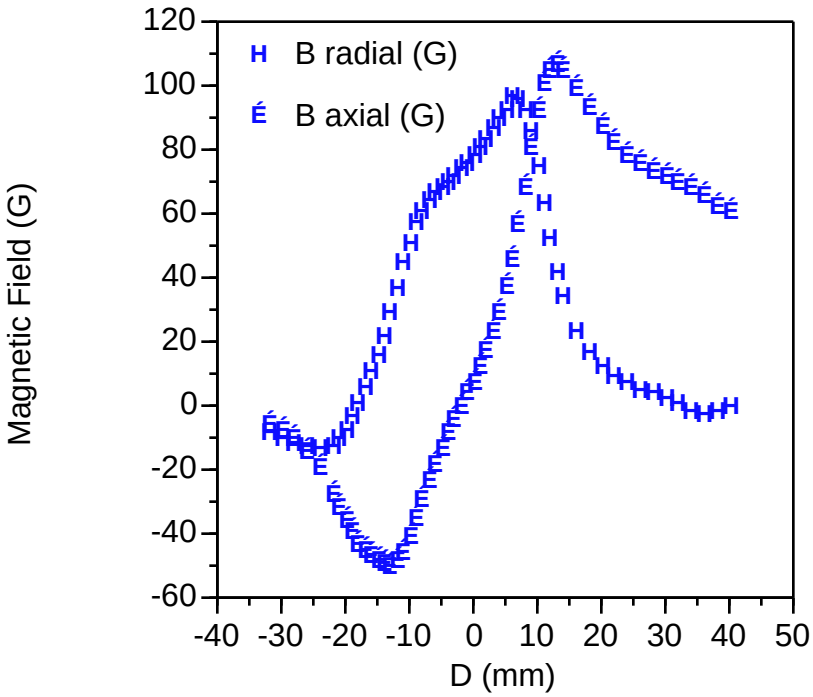

Figure 5.65. Magnetic field component strengths across the front of the thruster at an axial position of Z = 2 mm.

5.64 and 5.65 also account for the lack of significant discoloration on the front plate of the outer poles. The field lines are not as strong and are angled off normal to the front surface of the thruster.

Due to the low density of the plume, the question of electron conduction from the hollow cathode neutralizer toward the exit plane of the thruster is an important issue particularly in light of the radial components of the thruster magnetic field which extend into the plume. Electron conduction through this region is problematic. Classically, low energy electrons are constrained to travel along the magnetic field lines. As such, the electrons emitted from the hollow cathode neutralizer approach the thruster exit plane from the periphery near the outer poles, or through the central core. From these locations, the electrons would have to be transported across the magnetic field lines to the annular main plasma discharge. Several mechanisms may provide the enhanced electron transport necessary for this to occur. Plasma instabilities in the plume may lead to induced oscillatory electric and magnetic fields that enhance electron cross field diffusion. Alternatively, impacting primary electrons on the dielectric coating on the front surface of the thruster may be producing sufficient secondary electrons such that a number are effectively transported across field lines via a number of surface scattering events. Similar behavior has been proposed as an axial electron conduction mechanism within the acceleration channel (Fife and Martinez-Sanchez). Evidence that this behavior is occurring is shown in the plots of plasma potential and axial electric field for a discharge voltage of 250 V in Figures 5.50 and 5.59, respectively. At the exit plane, the plasma potential is nearly constant for several millimeters and the electric field is very low near the exit plane. Examination of the equations governing the cross field conductivity of a plasma given in Chapter 2 indicate that a sudden rise in the electron density would increase the local plasma conductivity causing the electric field to become small. The plasma potential measurements are confirmed by the ionic velocity measurements for this same conditions in Figure 5.15. The measured velocity is nearly constant for more than 5 mm centered on the exit plane.

5.5 Emission Spectroscopy Measurements

5.5.1 External Scan of Visible Spectrum

Figure 5.66 shows a typical scan of the visible spectrum of xenon taken with the collection optics of the LIF velocimetry apparatus with an Ebert-Fastie 0.5 m monochrometer with entry and exit slits set to 10 μm and a Hamamatsu R928 photomultiplier tube. The data has a relative intensity calibration based on a similar scan of a calibrated tungsten ribbon lamp, and a wavelength calibration based on a mercury vapor lamp. The scan shows the spectrum expected from a xenon plasma discharge. The strongest features are the neutral transitions at 823 and 828 nm. The strongest ionic transition is located at 835 nm. Otherwise, the stronger ionic transitions lie below 550 nm. Previous efforts (Manzella 1993) show that accurate determination of plasma parameters from emission spectroscopy is difficult due to the high degree of nonequilibrium. Therefore, the use of emission spectroscopy is qualitative rather than quantitative, yet may still provide valuable insights into the physics within the Hall thruster plasma discharge.

5.5.2 Neutral and Ionic Line Emission

Figure 5.67 shows the integrated line emission of the $6s[3/2]_2^0 - 6p[3/2]_2$ neutral xenon transition at 823.2 nm taken with the same apparatus used for the data in Figure 5.66, but with slits full open at 425 μm. The data shown was taken through the insulator slot with the collection optics focused to D = 0 mm. By only examining the signal from within the acceleration channel, the collection volume of the optics is clearly defined and does not traverse the entire plume. Although the collected emission is averaged across the acceleration channel, the sample volume is reasonably well defined.

The relative intensities shown in Figure 5.67 are representative of the $6p[3/2]_2$ level number density. From the data, there appear to be two high density regions. The first lies between the axial positions of Z = -20 and -5 mm and corresponds to the initial ion acceleration region. The peak signal in this region moves toward the anode with increasing discharge voltage. For all discharge voltages except 100 V, this peak decreases with increasing discharge voltage. The uniqueness of the 100 V case is not completely understood, but it

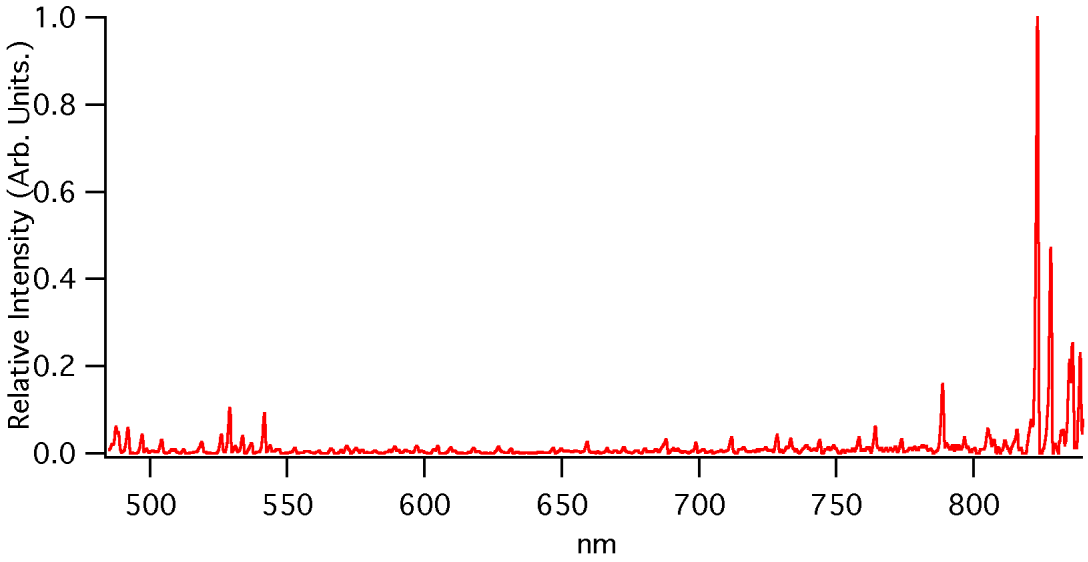

Figure 5.66. Emission scan of plume plasma centered 3 mm beyond the exit plane. A relative intensity calibration has been performed on this data.

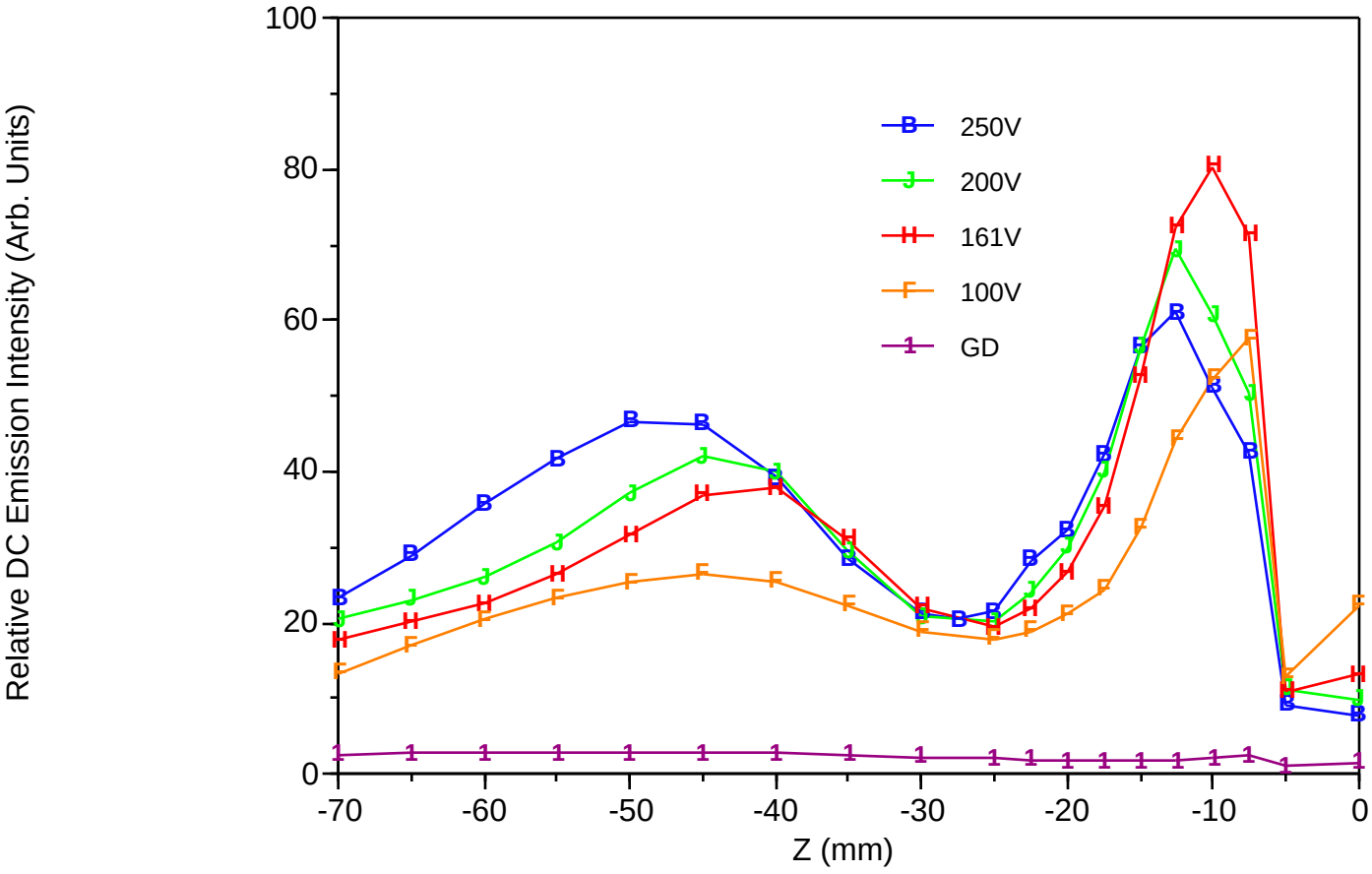

Figure 5.67. Relative intensity of the neutral line emission from the $6s[3/2]_2^0 - 6p[3/2]_2$ transition from within the Hall thruster.

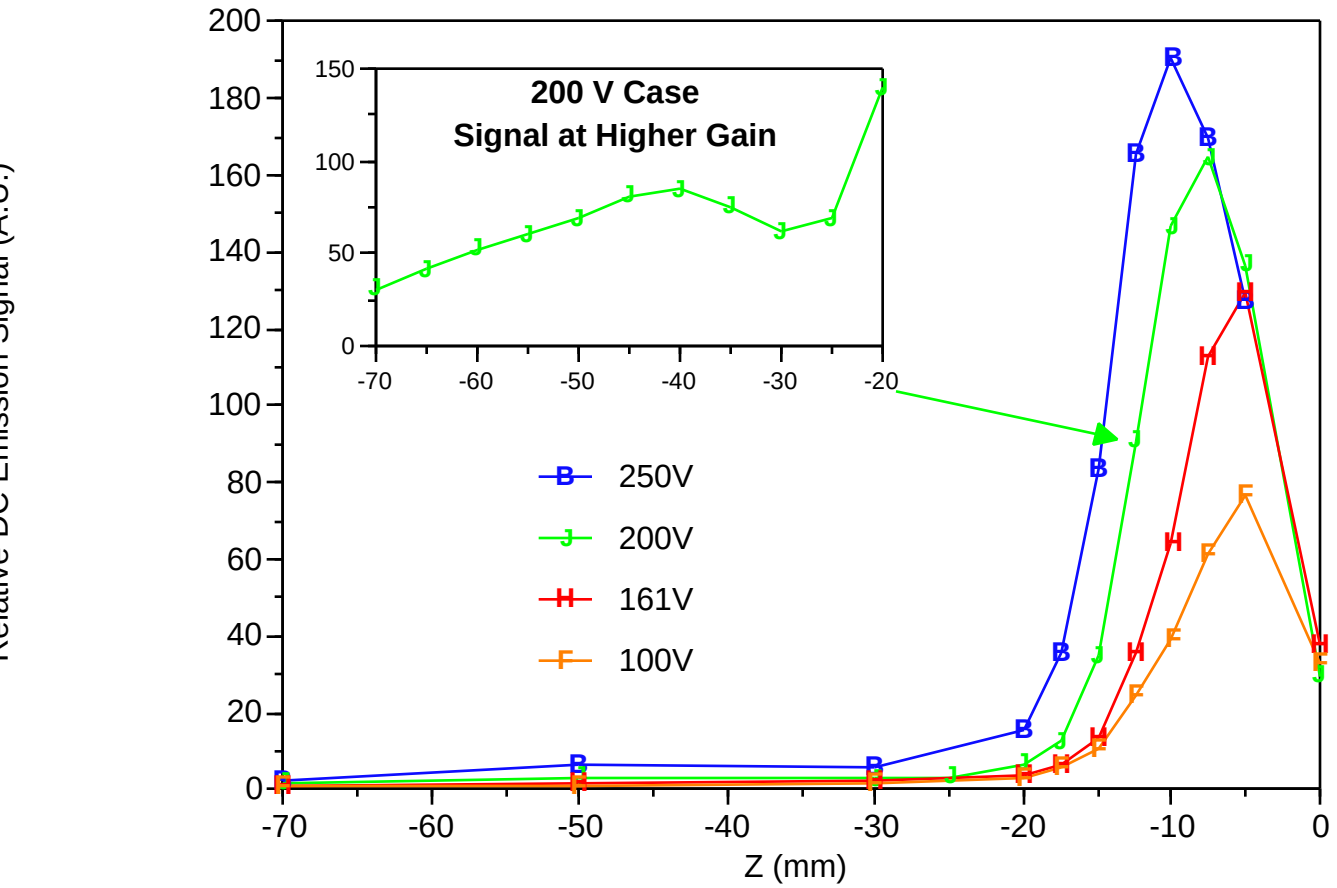

Figure 5.68. Relative intensity of the ionic line emission from the $6s[2]_{3/2} - 6p[3]_{5/2}$ transition from within the Hall thruster.

also differs in that the location and widths of the signal peak are not similar to the other three cases. These differences reinforce the notion that the 100 V case is substantially different than the other cases.

A second feature extends from the anode to Z = -30 mm. It is much less abrupt and much broader. Unlike the first, the peak and breadth appear to increase with increasing discharge voltage, and the peak also shifts toward the anode. The exception to this trend is the 100 V case in which the peak signal is almost aligned with the 200 V case. The 100 V case peak is does not follow the same trend. The peak does not rise in the same location and it is much broader than the peaks seen at higher discharge voltages.

Figure 5.68 shows a plot of the integrated line emission of the ionic xenon $6s[2]_{3/2} - 6p[3]_{5/2}$ transition at 541.9 nm. The shape of these curves is very different than the neutral emission shown in Figure 5.67. The most prominent feature lies between the exit

plane and Z = -20 mm. Here, a peak grows with increasing discharge voltage. The peak also shifts toward the anode and the width of the feature increases with increasing discharge voltage. Near the anode, there is evidence of a secondary feature. The insert in Figure 5.68 shows the intensity from Z = -70 to -20 mm at higher gain. There is a second peak two orders of magnitude lower in intensity than the primary peak at a position corresponding to the location of the second peak in the neutral emission curve shown in Figure 5.67 which also corresponds to a local maximum in ionic velocity seen in LIF velocimetry measurements. The primary ionic emission feature in Figure 5.68 indicates that the ionization of the propellant is occurring at locations where the signal is rising. Closer to the exit plane where the signal strength is decreasing, the ion density is lower due to the acceleration of the ionized propellant stream. The similar neutral emission feature in Figure 5.67 supports this statement. The electron collisional ionization process does not generally consist of a single collision event. Electron collisions with neutrals will usually first produce an excited state neutral and later collisions will result in an ion in an arbitrary excited state. The emission collected in shown in Figure 5.67 is at least partially produced by these intermediate excited neutral states.

The existence of the secondary ionic emission peak toward the anode is more difficult to explain. From Figure 5.67, a significant fraction of the neutrals are electronically excited in this region, but Figure 5.68 also indicates that there is not a significant ionic population. The relative populations of the excited neutral states are skewed by the excitation collisions that occur with higher frequency near the exit plane where electrons are constrained by the radial magnetic field. There are significantly more excited state neutrals nearer the exit plane, but ionizing collisions may occur before electronically excited states radiatively decay. Yet, both excited state neutrals and ions are being produced at the secondary peak near the anode. Another possible explanation is the existence of a weak shock at, or near, this location. The majority of the neutrals pass through this region without excitation, but a fraction are excited to higher energy levels, the radiative decay of which is detected as emission. A small fraction of the excited state neutrals are ionized. The shock would then represent the separation between the ions flowing toward the anode and those ions flowing out toward the exit plane. In order for charge neutrality to be held within the acceleration

channel, a number of ions must flow toward the anode with the electron current. LIF ionic velocimetry to some extent confirms negative ion velocities near the anode.

5.5.3 Comparison to a Glow Discharge

Some of the features seen in Figures 5.67 and 5.68 may be better understood by examining the behavior of the classic glow discharge. Figure 5.69 shows the portions of a low pressure glow discharge where the accepted nomenclature is used (Brown). The typical glow discharge is maintained by electrons produced by positive ion bombardment at the cathode. In the Aston dark space, there is an accumulation of electrons which gain energy by passage through the Crooks dark space. The cathode glow is the result of the relaxation of the positive ions undergoing neutralization. The electrons eventually gain sufficient energy in the Crookes dark space to produce exciting collisions which upon emissive relaxation produce the negative glow. The end of the negative glow corresponds to the extent of penetration of the electrons accelerated in the Crookes dark space. In the Faraday dark space, the electrons once more gain energy. The positive column is an ionized region extending from the Faraday dark space almost to the anode. In sufficiently large electrode separations, it serves as a conducting path to connect the Faraday dark space to the anode. This portion of the discharge is a true plasma where there is little or no charge separation. In the final several mean free paths prior to the anode, electrons may gain a sufficiently high energy to collisionally excite more neutrals thus producing the anode glow.

The Hall thruster is not a glow discharge, but shares some characteristics. Figure 5.70 shows neutral emission from the Hall thruster run at a glow discharge condition (1 A, 40 V, no applied magnetic field, residual magnetic field < 10 G). The neutral emission trace was taken at a significantly higher gain than those shown in Figure 5.67. The trace shows characteristics that are typical to the expected emission from a glow discharge in Figure 5.69. The general features of a positive column and negative glow appear distinctly where the exit plane may be treated as a virtual cathode. In the case of the Hall thruster discharge with an applied magnetic field, treating the exit plane as a virtual cathode is more valid. The radial magnetic field is an impedance to the electron current flow to the anode. In ideal operation, the Hall thruster operates at near constant current, near infinite impedance. Therefore,

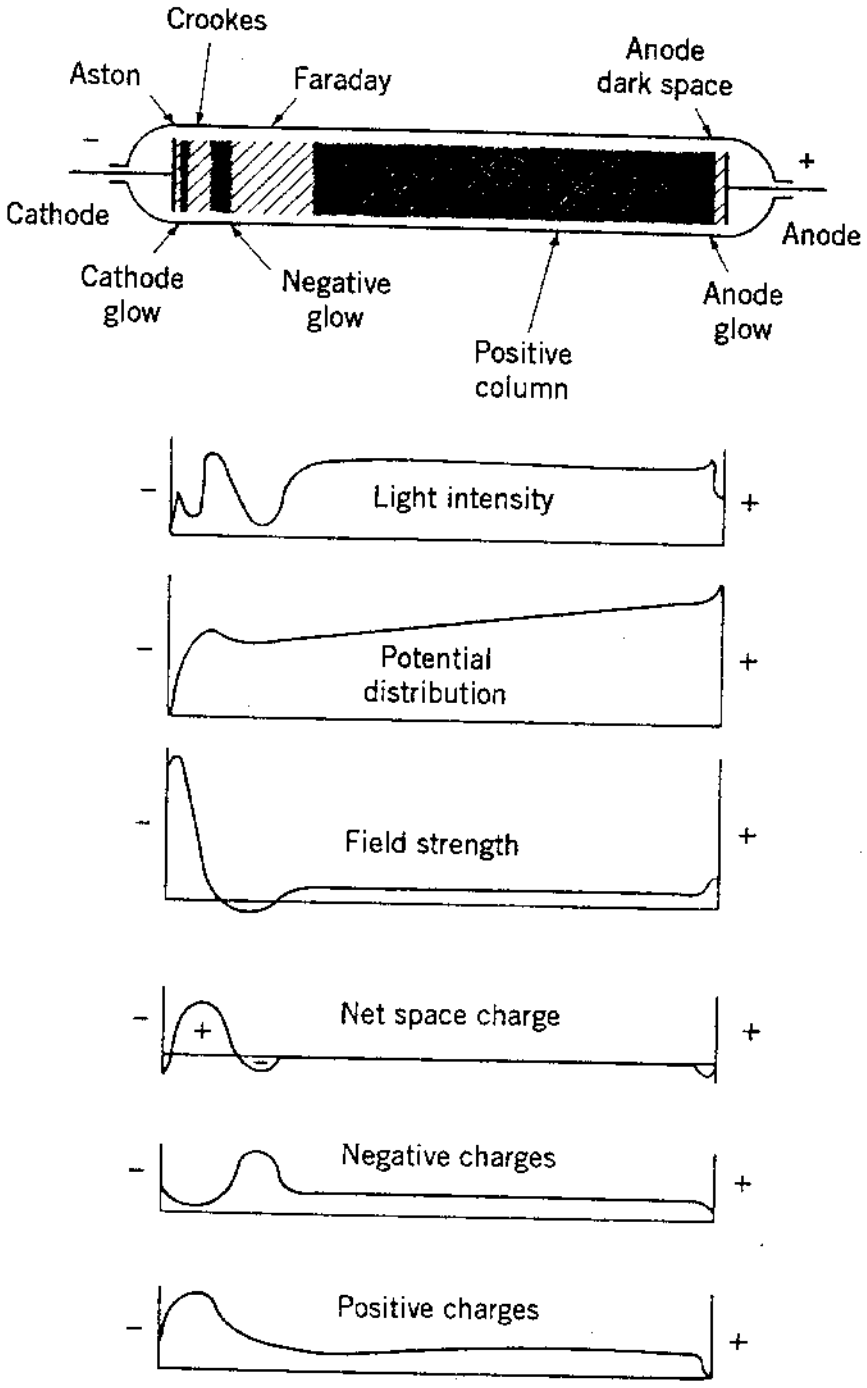

Figure 5.69. Classification of the regions of a glow discharge. Taken from S.C. Brown, 1994.

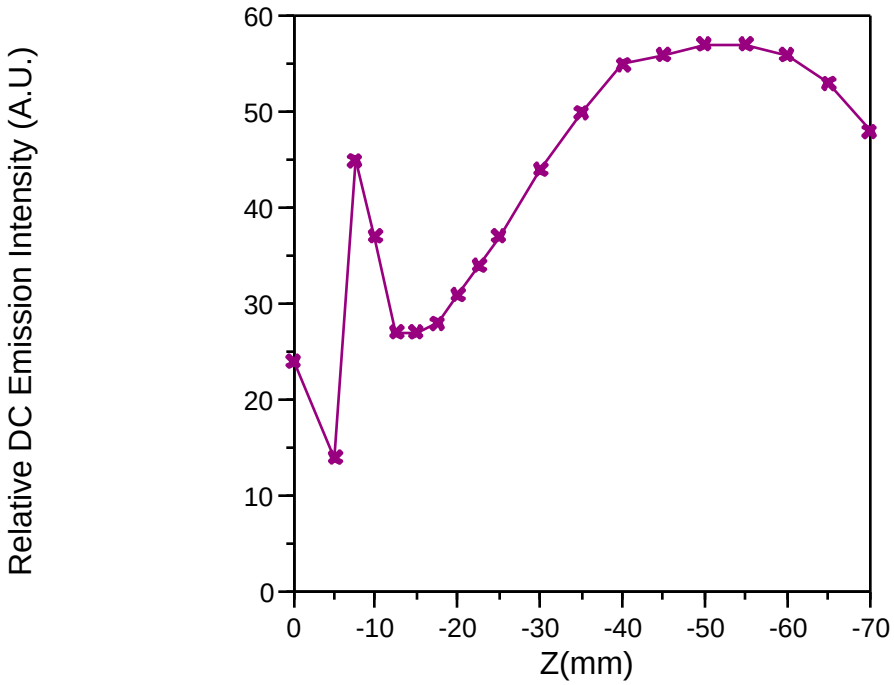

Figure 5.70. Glow discharge neutral emission at high gain.

treating the exit plane with its strong radial magnetic field as a virtual cathode in examining the plasma within a Hall type discharge is credible.

Examination of Figure 5.67 shows that neutral emission data for cases with applied magnetic field also have similarities to a glow discharge. The emission is similar in all cases. The ion emission curves exhibit a striking resemblance to the expected distribution of positive charge. Further comparisons can be made with the measured axial plasma potential profiles and the electric field profiles shown in Figures 5.47 through 5.49 and 5.56 through 5.59, respectively. In each of these cases, the measured plasma potential and electric field profiles in the interior of the thruster generally correspond to the behavior expected of a glow discharge.

5.5.4 Relative Electron Number Density and Corona Equilibrium

If the fractional population of the excited states is small, spectral line intensities are proportional to the electron density under corona equilibrium. This is especially true for transition energies less than the mean electron energy. Ideally, this would best hold with a state that was collisionally and radiatively connected to the ground state. Neither of the

lower states of the examined transitions is the ground state; however, the lower state of the $6s[3/2]_2^0 - 6p[3/2]_2$ neutral transition at 823.2 nm is metastable with a very long lifetime (42 s) and may serve as an virtual ground state. If so, Figure 5.67 shows the relative electron number density within the acceleration channel of the Hall thruster. With increasing discharge voltage, the location of peak electron density appears to move further into the acceleration channel. The electron density nearest the exit plane decreases with discharge voltage. This can be explained by the increased internal acceleration within the channel which in turn lowers the ion density. Due to charge neutrality, the electron density must in turn also be lower. Interestingly, the secondary feature nearer the anode is increasing in magnitude and breadth with increased discharge voltage. This appears to indicate that the electron density is increasing in this region. Figure 5.68 shows that the ionic density is increasing slightly in the rear of the thruster, but not to the levels seen closer to the exit plane. Also consistent with the comparison with the glow discharge, the peak in signal in Figure 5.67, corresponding to the electron density, lags the peak in Figure 5.68 which corresponds to the ion density. This behavior is also consistent with the behavior of a glow discharge.

Chapter 6. Summary and Recommendations for Future Work

6.1 Summary

The objective of this work was to measure plasma properties of a Hall thruster discharge in order to better understand the physics intrinsic to Hall thruster propellent acceleration. Due to the limited nature of existent modeling efforts, the understanding of the physical processes governing the operation of these plasma devices strongly relies on experimental diagnostics. For this reason, several laboratory Hall thrusters were constructed and tested. In order to construct these thrusters, the general physical concepts governing these devices had to be understood. These include, the crossed field production of an azimuthal Hall current which is responsible for a volume of magnetically retarded electrons. These electrons serve as a volumetric ionization zone for the neutral xenon propellant exiting from the anode. Once ionized, the propellant is accelerated through the electric fields generated by the same radial magnetic field that impedes the electrons. Once the ions have exited the thruster, an external electron source provides the electrons required to neutralize the ion beam. The Hall thruster is inherently an electrostatic thruster in that the propellant acceleration is solely due to electric body forces.

Although the Hall discharge appears to be quiescent, it is in fact the product of a number of unsteady processes. Among these is the electron transport through the radial magnetic field. A finite electron current must reach the anode to support the discharge. Due to the low densities and subsequent lack of collisions, classical electron cross-field transport is not sufficient. The discharge enhances electron transport by the production of plasma instabilities which create azimuthal electric fields which in turn produce axial Hall currents that drive electrons through the radial magnetic field. These instabilities occur at high frequencies and are often referred to as *plasma turbulence.*

Measurements of three broad plasma parameters were performed. These include thrust, neutral and ionic velocities, and plasma potential. Uniquely, the laser velocimetry measurements extend into the interior of the thruster through a 1 mm wide slot in the insula-

tor wall. Not only were measurements of the performance, propellant velocities, and plasma potential performed, but information on propellant energy deposition, electric field strength, electron temperature, and flow divergence were extracted from the data.

Thrust measurements showed that the two Hall thrusters were relatively efficient (~20%) and suitable for laboratory studies of Hall thruster physical phenomena. The prototype thruster was limited to low discharge voltages. The modified Hall thruster design corrected this short coming and operated at higher discharge voltages while maintaining similar performance characteristics. Facility effects impacted thruster performance and thrust measurements. The effects of relatively high background pressures could not be explored further due to limitations of the vacuum facility.

Typically, thrusters now rated for spacecraft, such as the Russian constructed SPT-100, claim efficiencies in the neighborhood of 50%. The differences between these mature, commercial designs and the thrusters constructed in this effort lie primarily in the magnetic field topology and materials used. Commercial Hall thrusters employ a number of schemes to tailor a more optimal magnetic field shape. Most of these thrusters employ shields of a magnetic material to minimize the axial component of the magnetic field. In some thrusters, magnetic trim coils are used to make fine adjustments in the field shape. Alternatively, the inner and outer coils of the magnetic circuit may be independently controlled to optimize the magnetic field. Although it is not responsible for the entire difference in performances, the effect of the relatively limited vacuum facility must also not be neglected. As the performance measurements implied, the limited pumping speed restricted testing to what may have been lower than optimal propellant flow rates. Therefore, it is likely that the low performance of the thrusters in this work could be substantially improved by testing in a more capable vacuum chamber.

In addition, it has been suggested in this work that the background pressure affects the operation of these devices. High background pressures caused difficulties at higher discharge voltages. For example, operation at 250 V was generally limited to less than 1 or 2 hours. A possible reason is a correlation between some modes of plasma oscillations and background pressures typical of the vacuum facility in this study (10^{-4} Torr). How these instabilities, whether or not due to the relatively high background pressure, affected thruster performance is unknown.

Laser induced fluorescence velocimetry measurements utilized the techniques developed by previous Stanford researchers. Ionic velocity measurements of axial velocity both inside and outside the thruster as well as radial velocity measurements in the plume were performed using LIF with nonresonant signal detection using the ionic xenon $5d[4]_{7/2} - 6p[3]_{5/2}$ excitation transition while monitoring signal from the $6s[2]_{3/2} - 6p[3]_{5/2}$ transition. Neutral velocity measurements were similarly performed in the interior of the Hall thruster using the $6s[3/2]_2^0 - 6p[3/2]_2$ transition with resonance fluorescence collection. While most of the velocity measurements used partially saturated fluorescence signals to improve the signal to noise ratio, one ionic transition radial trace was taken in the linear fluorescence region and yielded an ionic translational temperature between 450 and 750 K. However since the hyperfine structure constants are not known for the $5d[4]_{7/2}$ level, the constants for the $5d[3]_{7/2}$ were used instead. Therefore, this result should be viewed as an approximation. If the hyperfine structure is altogether ignored, the kinetic temperature may be as high as 1700 K. Ionic velocity data allowed for the measurement of the energy deposited into the propellant stream which was calculated as the kinetic energy of the ions. An effective electric field was calculated from the quasi-potential data which is representative of the propellant acceleration.

Plasma potential measurements were performed with two emissive probe designs. Initial measurements showed that a robust probe design was necessary to ensure repeatable measurements. Unfortunately, the larger, more survivable probe perturbed the anode discharge of the Hall thruster. Potential measurements showed that the far plume was approximately 15 V above ground, corresponding the potential of the electrons produced by the hollow cathode neutralizer. Axial electric fields derived from the plasma potential measurements show that the field peaks just inside the exit plane. Maximum field strengths were found to be approach 10,000 V/m. At the exit plane, the axial electric fields dip to near zero for nearly all cases. This axial electric field feature is due to an increase in the local plasma conductivity. The mechanism for this increased conductivity is due to an increase in the local electron number density, or an increased presence of plasma instabilities which promote electron cross-field diffusion. It also was possible to determine electron temperatures at the location of each plasma potential measurement by also measuring the probe floating potential.

The line emission from the neutral xenon $6s[3/2]_2^0 - 6p[3/2]_2$ transition was measured through the thruster insulator slot. Similar emission measurements were performed for the ionic xenon $6s[2]_{3/2} - 6p[3]_{5/2}$ transition. These measurements showed that ions are generated near the exit plane and the ionization plane moves further into the thruster with increasing discharge voltage. Neutral emission indicates that excited state neutrals are widely distributed along the length of the acceleration channel. Distinct features which are similar in shape in all cases suggest that there are excitation phenomena occurring near the anode. From LIF ionic velocity measurements, the feature may correspond to the location of ion flow reversal. The emission feature may be indicative of a shock associated with ion flow separation. Flow reversal is expected since in order for the plasma to retain its quasi-neutrality some ions must flow with the electron current to the anode. Due to the metastable nature of the neutral $6s[3/2]_2^0$ state, it is possible to view it as a pseudo-ground state. If it can be shown that an equilibrium condition similar to corona equilibrium holds within the thruster acceleration channel, the spectral line intensity is proportional to the electron density since electron-neutral collisions are the sole means for excitation to higher levels.

In this work, two laboratory Hall thrusters were constructed and tested. Thrust measurements indicate that these devices were relatively efficient (20%) at converting electrical power into thrust and served well as laboratory Hall thrusters for understanding the basic physics which govern the devices. Various diagnostics probed the Hall thruster plasma. These diagnostics allowed for the plasma propellant acceleration process to be examined in detail.

Overall, the thruster was adequate for improving the understanding of the propellant acceleration within a coaxial Hall thruster. While it was not optimized for high performance, it was outstanding as a robust and fully accessible research test article. If magnetic shielding or trim coils had been in place, the optical access that this thruster so readily provided would have been compromised by the additional hardware. Specifically in the case of the magnetic shields, it would have been necessary to cut through a portion of the shielding to obtain optical access to the insulator. The required slot through the magnetic shielding would have locally introduced axial magnetic field components thus modifying the mag-

netic field in the area of observation. The resulting change in the plasma conductivity would have changed the thruster behavior.

6.2 Recommendations for Future Work

6.2.1 Advanced Magnetic Circuits for Hall Thrusters

Most Hall thruster development work has been empirical. This is particularly true in the design of the Hall thruster magnetic field. There have been few studies on the effects of variations on the magnetic field. Therefore, a series of combined numerical studies of the magnetic field with extensive experimental confirmation would be valuable to the Hall thruster community.

State of the art Hall thruster technology currently is able to claim efficiencies between 50 and 60%. This high efficiency indicates that any further improvement will require serious study and an excellent understanding of the physics governing these devices. Current numerical models show promise of aiding in the design of new, more efficient Hall thrusters. However, little effort is being expended in improving thruster performance through the modification of the electric and magnetic fields.

As envisioned, this project would entail three parts. First, a three dimensional electromagnetic simulator would directly integrate Maxwell's equations to design specifically tailored magnetic fields and determine how such configurations may be achieved. Issues that could be explored include the creation of a sharper transition for the radial magnetic field profile, the reduction, or possible elimination, of axial components of the magnetic field, and the minimization of the magnetic field outside the acceleration channel. Many of these issues are much more easily treated in a thorough series of numerical simulations than by the construction and testing of a large number of expensive Hall thrusters.

The second portion of the study would determine the effect of more exotic magnetic circuit configurations on the performance of a Hall thruster using a numerical model. At first, a model of Hall thruster performance could be used to confirm the measurements performed by Morozov in 1972 which showed the effect of three broad types of magnetic field profiles on the efficiency of a Hall thruster. These were positive gradient, zero gradient (constant field), and negative gradient radial magnetic field profiles. Confirming the perfor-

mances measured by Morozov would show that the model can resolve gains from variations in the magnetic field configuration. Once the model is validated, the next step would be to model the configurations produced by the first effort. Ideally, the two numerical efforts would be performed in tandem. So that trends determined by the modeling of the thruster performance could be exploited.

The third portion of the study would be the construction and testing of a Hall thruster with an advanced magnetic circuit design. This would be the most challenging portion of the project as the magnetic field of the actual device would have to be meticulously compared to the desired magnetic field. Careful accounting of real effects would have to be made in order to reproduce the desired configuration. At this point, further modeling of the device's performance may be necessary to determine the expected deviation of the real device from the ideal case. Performance testing of one, or two, of the configurations numerically chosen to be superior would finally serve to validate the advanced magnetic circuit concept.

6.2.2 Development of a Linear Hall Thruster

Parallel to the ongoing advancements in the use and understanding of Hall thruster technology, microsatellite technology has become an increasingly important area of study. Small satellites offer the advantages of lower launch and operational costs along with shorter development times, allowing spacecraft of all types and missions to be developed and deployed quickly and inexpensively. For these small, lightweight satellites, electric propulsion with high specific impulses and high efficiencies is ideal if suitable thrusters can be developed.

Available coaxial Hall thrusters have been scaled to low powers, but have proven to be less efficient than larger devices. It is unknown whether a coaxial geometry is absolutely necessary in the design of an efficient miniaturized Hall thruster. There are several advantages of a linear geometry for a Hall thruster. It is easier to scale a linear device. In the simplest case, a linear Hall discharge can be initially tested for optimum magnetic field and propellant flows. Once, these conditions are established, the thruster could simply be lengthened to produce larger thrust levels. It would then no longer be necessary to have on hand a number of coaxial thrusters of varying diameters. Should a satellite need high thrusts at the

beginning of life for such things as orbit raising or repositioning, an array of linear thrusters could be used. When small corrections, such as station keeping, are required only propellant flow to one, or several, of the linear channels in the array would be required. In this way, an array of linear Hall thrusters could provide optimal specific impulse and thrust efficiency at a number of thrust levels with the use of a single thruster.

A number of preliminary tests have been performed on several designs for a linear Hall thruster. Many issues remain unresolved. The effect of a open circuit Hall current on the discharge is uncertain and appears to be the most important constraint on the operation of a linear Hall thruster geometry. Yet, linear devices have functioned at conditions that mirror the behavior of a coaxial Hall thruster. The effect of the Hall current in Hall type thrusters needs to be better understood. A tantalum wire placed around the acceleration channel of a linear thruster in an attempt to short the Hall current has proven to be insufficient. A better solution would be to place a thoriated filament at each end of the linear acceleration channel. These two filaments will be placed on a single isolated power circuit such that they can be heated and float at the local plasma potential. This dual filament device should then electrically connect the two ends of the acceleration channel, shorting the Hall current. This next stage of testing will determine the importance of the Hall current in this device.

The cathode configuration will also have to be modified. The hollow cathode neutralizer used in initial tests consumed nearly as much propellant as the anode. Future tests should use a thoriated filament which should provide sufficient electron current to neutralize the ion beam. This will eliminate a significant fraction of the propellant flow and increase efficiency. Another important design issue that requires further exploration is an improved circuit to mitigate the affect of plasma oscillations on the various power supplies supporting the plasma discharge. Thus far, this approach has yielded the most dramatic improvements in thruster stability. It therefore should be explored in a more systematic way.

Although the initial set of tests of a linear Hall thruster geometry have not been fully successful, they have shown a great deal of promise. The effects of the Hall current on thruster operation are still not absolutely clear. It should be possible to examine this issue by using heated filaments to electrically short the ends of the acceleration channel. Even if this modification is the only method by which the thruster can be stably operated, this device

will provide important information on the oscillatory nature common to all Hall thrusters and will allow researchers to better understand Hall thrusters.

References

R. C. Alig and S. Bloom, “Secondary Electron Escape Probabilities,” *Journal of Applied Physics*, Vol. 49, No. 6, June 1978.

J. Ashkenazy, Y. Raistes, and G. Appelbaum, “Investigations of a Laboratory Model Hall Thruster,” AIAA-95-2673, 31st Joint Propulsion Conference, July 10-12, 1995, San Diego, CA.

V. I. Baranov, Y. S. Nazarenko, V. A. Petrosov, A. I. Vasin, and Y. M. Yashnov, “Theory of Oscillations and Conductivity for Hall Thrusters,” AIAA-96-3192, 32nd Joint Propulsion Conference, July 1-3, 1996, Lake Buena Vista, FL.

D. A. Barnhart, J. M. McCombe, and D. L. Tilley, “Electric Propulsion Integration Activities on the MSTI Spacecraft,” IEPC-93-011, 23rd International Electric Propulsion Conference, Sept. 23-27, 1993, Seattle, WA.

C. R. Bingham, M. L. Gaillard, D. J. Pegg, H. K. Carter, R. L. Mlekodaj, J. D. Cole, and P. M. Griffin, “Colinear Fast-Beam laser Spectroscopy Experiment: Measurement of Hyperfine Structure and Isotope Shifts in Xe II,” *Nuclear Instruments and Methods*, Vol. 202, 1982.

N. Bober, N. Maslennikov, M. Day, G. Popov, and Yu. Rylov, “Development and Application of Electric Propulsion Thrusters in Russia,” IEPC-93-001, 23rd International Electric Propulsion Conference, Sept. 23-27, 1993, Seattle, WA.

G. Borghs, P. De Bisschop, R. E. Silerans, M. Van Hove, and J. M. Van den Cruyce, “Hyperfine Structures and Isotope Shifts of the $5d^4D_{7/2} \rightarrow 6p^4P^0_{5/2}$ Transition in Xenon Ions,” *Atoms and Nuclei*, Vol. 299, 1981.

J. Brophy, “Advanced Ion Propulsion Technology for Solar System Exploration,” AIAA-97-2782, 33rd Joint Propulsion Conference, July 6-9, 1997, Seattle, WA.

L. Bronstrom, A. Kastberg, J. Lidberg, S. Mannervik, “Hyperfine-structure Measurements in Xe II,” *Physical Review A*, Vol. 35, No. 1, Jan. 1996.

C. O. Brown and E. A. Pinsley, “Further Experimental Investigations of a Cesium Hall-Current Accelerator,” *AIAA Journal*, Vol. 3, No. 5.

S. C. Brown, *Basic data of Plasma Physics: The Fundamental Data on Electrical Discharges in Gases*, American Institute of Physics, 1994.

A.I. Bugrova, A.S. Lipatov, V.K. Kharchevnikov, D.V. Churbanov, A.I. Morozov, “SPT-ATON Tests at Kurchatov Institute Stands,” IEPC-95-067, 24th International Electric Propulsion Conference, Sept. 19-23, 1995, Moscow, Russia.

R. J. Cedolin, *Laser-Induced Fluorescence Diagnostics of Xenon Plasmas*, Ph.D. Dissertation, Mechanical Engineering, Stanford University, June 1997.

R. J. Cedolin, Personal Communication, 23 Jan. 1999.

F. F. Chen, *Introduction to Plasma Physics and Controlled Fusion: Volume 1*, Plenum Press, New York, 1990.

E.Y. Choueiri, “Characterization of Oscillations in Closed Drift Thrusters,” AIAA-94-3013, 30th Joint Propulsion Conference, June 27-29, 1994, Indianapolis, IN.

R. D. Cowan, *The Theory of Atomic Structure and Spectra*, University of California Press, Berkley, California, 1981.

M. W. Crofton, *Evaluation of Electric Thrusters,* Aerospace Report No. ATR-97(8201)-1, The Aerospace Corp., El Segundo, California, 1997.

P. H. Dawson, "Secondary Electron Emission Yields of Some Ceramics," *Journal of Applied Physics,* Vol. 37, June 1978.

W. Demtroder, *Laser Spectroscopy: Basic Concepts and Instrumentation,* Springer-Verlag, Berlin, 1996.

A. C. Eckbreth, *Laser Diagnostics for Combustion Temperature and Species,* Overseas Publishers Association, Amsterdam, 1996.

Y. B. Esipchuk, A. I. Morozov, G. N. Tilinin, and A. V. Trofimov, "Plasma Oscillations in Closed-Drift Accelerators with an Extended Acceleration Zone," *Soviet Physics - Technical Physics,* Vol. 18, 1974.

Y. B. Esipchuk and G. N. Tilinin, "Drift Instability in a Hall Current Plasma Accelerator," *Soviet Physics - Technical Physics,* Vol. 21, 1976.

J. M. Fife, Personal Communication, 23 Jun. 1999

J. M. Fife, M. Martinez-Sanchez, and J. Szabo, "A numerical Study of Discharge Oscillations in Hall Thrusters," AIAA-97-3081, 33rd Joint Propulsion Conference, Seattle, WA, July 6-9, 1997.

W. Fischer, H. Huhnermann, G. Kromer, and H.J. Schafer, "Isotope Shifts in the Atomic Spectrum of Xenon and Nuclear Deformation Effects," *Z. Physik,* Vol. 270, No. 113, 1974.

V. Gakusha, S. Semenkin, and S. Tverdokhlebov, "Thermal Analysis of the Anode Layer Thruster Operation," IEPC-97-150, 25th International Electric Propulsion Conference, Aug. 24-28, 1997, Cleveland, OH.

S. Garpman and N. Spector, "Transition Probabilities for the $5p^4 6p - 5p^4 6s$ Array of Xe II," *Journal of the Optical Society of America,* Vol. 66, No. 9, Sept. 1976.

V. M. Gavryshin, V. Kim, V. I. Kozlov, and N. A. Maslennikov, "Physical and Technical Basis of the Modern SPT Development," IEPC-95-038, 24th International Electric Propulsion Conference, Sept. 19-23, 1995, Moscow, Russia.

H. Geisen, T. Krumpelmann, D. Neuschafer, and Ch. Ottinger, "Hyperfine Splitting Measurements on the 6265 Å and 6507 Å Lines of Seven Xe Isotopes by LIF on a Beam of Metastable Xe($^3P_{0,3}$) Atoms," *Physics Letters A,* Vol. 130, No. 4.5, 11 July 1988.

R. H. Goddard, *The Papers of Robert H. Goddard,* Eds. E. C. Goddard and G. E. Penray, McGraw-Hill Book Co., New York, 1970.

H. R. Griem, *Plasma Spectroscopy*, McGraw-Hill Book Company, New York, 1964.

H. R. Griem, *Spectral Line Broadening by Plasmas*, Academic Press, New York, 1964.

H. R. Griem, *Principles of Plasma Spectroscopy,* Cambridge University Press, Cambridge, 1997.

T. W. Haig and F. W. Curran, "Arcjet Starting Reliability: A Multistart Test on Hydrogen / Nitrogen Mixtures," AIAA-87-1061, 19th International Electric Propulsion Conference, May 11-13, 1987, Colorado Springs, CO.

J. E. Hansen and W. Persson, "Revised Analysis of Singly Ionized Xenon, Xe II," *Physica Scripta*, Vol. 36, 1987.

N. Hershkowitz, "Theory of Electrostatic Probes," *Plasma Diagnostics: Volume 1*, Eds. O. Auciello and D. L. Flam, Academic Press, Inc., 1989.

G. Herzberg, *Atomic Spectra and Atomic Structure*, Dover Publications, New York, 1944.

P. G. Hill and C.R. Peterson, *Mechanics and Thermodynamics of Propulsion*, Addison-Wesly Publishing Co., Reading, MA, 1965.

C. J. Humpreys, "Second Spectrum of Xenon," *Journal of the National Bureau of Standards*, Vol. 22, Jan. 1939.

D. A. Jackson and M. C. Coulombe, "Isotope Shifts in the Arc Spectrum of Xenon," *Proceedings of the Royal Society London, A.*, Vol. 338, 1974.

R. G. Jahn, *Physics of Electric Propulsion*, McGraw-Hill Book Co., New York, 1968.

S. W. Janson, "The On-Orbit Role of Electric Propulsion," AIAA-93-2220, 29th Joint Propulsion Conference, 28-30 June 1993, Monterey, CA.

V. Khayms and M. Martinez-Sanchez, "Design of a Miniaturized Hall Thruster for Mircosatellites," AIAA-96-3291, 32nd Joint Propulsion Conference, July 1-3, 1996, Lake Buena Vista, FL.

L. B. King, *Transport-Property and Mass Spectral Measurements in the Plasma Exhaust Plume of a Hall-Effect Space Propulsion System*, Ph.D. Dissertation, Aerospace Engineering, University of Michigan, June 1998.

Larson and J. R. Wertz, *Space Mission Analysis and Design*, Microcosm, Inc., Torrance, CA, 1992.

E. C. Lary, R. G. Meynard, Jr., and F. Salz, "Ion Acceleration in a Gyro-Dominated Neutral Plasma - Theory and Experiment," *Bulletin of the American Physical Society*, Vol. 7, p 441, 1962.

D. R. Lidde, Ed., *Handbook of Chemistry and Physics*, CRC Press, Inc., Boca Raton, Florida, 74th Edition, 1993.

M. A. Lierberman and A. J. Lichtenberg, *Principles of Plasma Discharges and Materials Processing*, John Wiley and Sons, Inc., New York, 1994.

R. P. Lucht, "Applications of Laser-Induced Fluorescence Spectroscopy," *Laser Spectroscopy and its Applications*, Eds. L. J. Radziemski, R. W. Solarz, and J. A. Paisner, Marcel Dekker, New York, 1987.

D. H. Manzella, "Stationary Plasma Thruster Plume Emissions," IEPC-93-097, 23rd International Electric Propulsion Conference Sept., 1993, Seattle, WA.

D. H. Manzella, "Stationary Plasma Thruster Ion Velocity Distribution," AIAA-94-3141, 30th Joint Propulsion Conference, June 27-29, 1994, Indianapolis, IN.

M. Mitchner and C. H. Kruger, Jr., *Partially Ionized Gases*, John Wiley and Sons, Inc., 1992.

A.I. Morizov, Y.V. Esipchuk, A.M. Kapulkin, V.A. Nevroskii, and V.A. Smirnov, "Effect of the Magnetic Field on a Closed-Electronic-Drift Accelerator," *Soviet Physics - Technical Physics*, Vol. 17, No. 3, Sept. 1972.

A. I. Morizov, Y. V. Esipchuk, G. N. Tilinin., A. V. Trofimov, Yu. A. Sharov, and G. Ya. Shshepkin, "Plasma Accelerator with Closed Electron Drift and Extended Acceleration Zone," *Soviet Physics - Technical Physics*, Vol. 17, No. 1, July 1972.

C. E. Moore, *Atomic Energy Levels: Volume III*, National Bureau of Standards, Washington, 1958.

Y. Raistes, J. Ashkenazy, and G. Appelbaum, “Experimental Investigation of the Effect of Channel Material on Hall Thruster Characteristics,” IEPC-97-056, 25th International Electric Propulsion Conference, Aug. 24-28, 1997, Cleveland, OH.

Y. Raistes, J. Ashkenazy, and G. Appelbaum, “Probe Measurements of Plasma Properties Inside and Experimental Hall Thruster,” AIAA-98-3640, 34th Joint Propulsion Conference, July 13-15, 1998, Cleveland, OH.

T. Randolph, V. Kim, H. Kaufman, K. Korzubusky, V. Zhurin, and M. Day, “Facility Effects on Stationary Plasma Thruster Testing,” IEPC-93-93, 23rd International Electric Propulsion Conference Sept. 23-27, 1993, Seattle, WA.

P. A. Redhead, J. P. Hobson, and E. V. Kornelsen, *The Physical Basis of Ultrahigh Vacuum,* American Institute of Physics, New York, 1993.

A.V. Rusakov, A.V. Kochegin, A.V. Semenkin, and S.O. Tverdokhlebov, “Multiple Thruster Propulsion Systems Integration Study,” IEPC-97-130, 25th International Electric Propulsion Conference, Aug. 24-28, 1997, Cleveland, OH.

R. Salasovich, D. Bromaghim, and A. Sutton, “Diagnostic and Flight Planning for the U.S. Air Force Electronic Propulsion Experiment (ESEX),” AIAA-97-2777, 33rd Joint Propulsion Conference, July 6-9, 1997, Seattle, WA.

J. M. Sankovic, J. A. Hamley, and T. W. Haag, “Performance Evaluation of the Russian SPT-100 Thruster and NASA LeRC,” IEPC-93-094, 23rd International Electric Propulsion Conference Sept. 23-27, 1993, Seattle, WA.

M. J. Seaton, “The Theory of Excitation and Ionization by Electron Impact,” *Atomic and Molecular Processes*, Ed. D.R. Bates, Academic Press, New York, 1962.

G. R. Seikel, and E. Reshotko, “Hall Current Accelerator,” *Bulletin of the American Physical Society*, Vol. 7, p 414, 1962.

I. I. Sobelman, *Atomic Spectra and Radiative Transitions*, Springer-Verlag, New York, 1992.

G. G. Spanjers, J. B. Malak, R. J. Leiweke, and R. A. Spores, “The Effect of Propellant Temperature of Efficiency in a Pulsed Plasma Thruster,” AIAA-97-2920, 33rd Joint Propulsion Conference, July 6-9, 1997, Seattle, WA.

R. A. Spores, M. Birkan, and R. B. Cohen, “The Air Force Electric Propulsion Program,” AIAA-95-2373, 31st Joint Propulsion Conference, July 10-12, 1995, San Diego, CA.

R. A. Spores, R. B. Cohen, M. Birkan, “The USAF Electric Propulsion Program,” IEPC-97-001, 25th International Electric Propulsion Conference, Aug. 24-28, 1997, Cleveland, OH.

J. J. Szabo and J. E. Pollard, “A Laboratory-Scale Hall Thruster,” AIAA-95-2926, 31st Joint Propulsion Conference, July 10-12, 1995, San Diego, CA.

K. Toki and A. Sassoh, “An Overview of Electric Propulsion Activities in Japan,” IEPC-97-005, 25th International Electric Propulsion Conference, Aug. 24-28, 1997, Cleveland, OH.

W. G. Vincenti and C. H. Kruger, Jr., *Introduction to Physical Gas Dynamics*, Robert E. Krieger Publishing Company, Malabar, FL, 1982.

M. Walhout, A. Witte, and S. L. Rolston, “Precision Measurement of the Metastable $6s[3/2]_2$ Lifetime in Xenon,” *Physical Review Letters*, Vol. 72, No. 18, 2 May, 1994.

R. C. Weast, Ed., *Handbook of Chemistry and Physics*, CRC Press, Inc., Boca Raton, Florida, 69th Edition, 1998.

H. E. White, *Introduction to Atomic Spectra*, McGraw-Hill Book Co., New York, 1934.

A. Y. Wong, *Introduction to Experimental Plasma Physics*, UCLA Press, 1977.

S. Yoshikawa and D. J. Rose, "Anomalous Diffusion of a Plasma Across a Magnetic Field," *Physics of Fluids*, Vol. 5, No. 3, March 1963.